HARDWARE AND SOFTWARE DEVELOPMENT FOR IMPLEMENTATION OF FAST AND SAFE CHARGING OF COMMERICAL LIHTIUM-ION BATTERIES

by

Noah Robert Hedding

A thesis submitted in partial fulfillment
of the requirements for the degree

of

Master of Science

in

Electrical Engineering

MONTANA STATE UNIVERSITY
Bozeman, Montana

May 2023

ACKNOWLEDGEMENTS

I would like to acknowledge my fiancé, Samantha. She is always willing to listen to my niche and obscure problems; I could not have completed this work without her support.

I would like to acknowledge Dr. Hongwei Gao for giving me a chance to participate in exciting research as an undergraduate student. This work created the interests and passions that will define the rest of my career.

Research was sponsored by the DEVCOM Army Research Laboratory (ARL) and was funded under Cooperative Agreement (CA) Number W911NF-20-2-0284. The views and conclusions contained in this document are those of the authors and should not be interpreted as representing the official policies, either expressed or implied, of the DEVCOM Army Research Laboratory or the U.S. Government. The U.S. Government is authorized to reproduce and distribute reprints for Government purposes notwithstanding any copyright notation hereon.

TABLE OF CONTENTS

TABLE OF CONTENTS CONTINUED

ABLE OF CONTENTS CONTINUED

LIST OF TABLES

Table Page

LIST OF FIGURES

Figure Page

LIST OF FIGURES CONTINUED

Figure Page

LIST OF FIGURES CONTINUED

Figure Page

LIST OF FIGURES CONTINUED

Figure Page

LIST OF FIGURES CONTINUED

Figure Page

ABSTRACT

From single cells in handheld electronics to enormous packs in battery electric vehicles (BEV), batteries govern modern life. Lithium ion batteries (LIB) present the best available commercially available products for these applications; they have the highest energy densities and can output currents many times their capacity. But safely charging LIBs requires a slow and detailed process which is typically unacceptable for use in BEV and other rugged handheld devices; therefore, decreasing the required charging time would be greatly beneficial. Fast charging methods do present dangers and concerns. Unmonitored fast charging of LIBs allows for the potential of lithium plating where the lithium ions within the cell are converted to metallic lithium at the battery anode. Lithium plating can remove these ions from the charging and discharging process causing reductions in battery capacity. The metallic lithium structures formed also present the dangers of short circuit and thermal runaway. In this thesis, a charging protocol is developed using equivalent circuit models and experimentation with the goal of the elimination of lithium plating. First, equivalent models of a test cell were determined and validated. Then, this test cell was used to find the fast charging protocol both experimentally and through the use the equivalent circuit elements. Custom power electronics and software were then developed to implement the proposed charging protocol on commercial LIBs for 350 cycles. The results of this experiment show that the charging protocol did not create noticeable lithium plating while decreasing the charging time required by a typical constant current – constant voltage (CC/CV) from 50 minutes to 29 minutes. The proposed charging protocol decreased the charging time without stressing the LIB beyond its set limitation.

INTRODUCTION

Lithium ion batteries are widely used in portable electronics, communication devices, power tools, electric vehicles. Lithium ion battery (LIB) cells are the overwhelming choice for use in modern devices; they offer the highest volumetric and gravimetric energy density of any practical energy choice [1]. As LIBs can take several forms, including cylindrical, pouch, and coin, they are excellent for inclusion where size and mass must be minimized. The capacities of these devices enable portable electronics to complete previously impossible tasks and achieve long discharge lives.

Charging LIBs is extremely important; the quality of the charging will contribute to several key aspects of battery health. Currently, the standard charging protocol for LIBs requires nearly 2.5 hours. This is considered unacceptable for applications requiring quick charging turn-around times such as electric vehicles (EV) or rugged portable devices such as communications equipment. To allow for shorter charging times for LIBs, fast charging can be used, often charging beyond the manufacturer's recommendations. Fast charging will result in shorter charging times but will also cause the LIB more stress and induce more degradation. One of the main degradation factors in LIBs is lithium plating. Lithium plating will occur when the lithium ions, present within the LIB, are converted to metallic lithium. The metallic lithium will form into dendrites which are long, thin crystalline structures. The formation of metallic lithium dendrites can remove cyclable lithium from the LIB and pose the threat of internal short circuit. These short circuits can lead to thermal runaway and dangerous fires. Therefore, in designing a fast charging protocol, the mitigation of lithium plating should be a driving factor.

In this thesis, a fast charging protocol is proposed, simulated, and experimentally evaluated. This charging protocol focuses on the elimination of lithium plating during the charging process. First, the terminology surrounding batteries, charging, and discharging will be introduced; this discussion gives useful context. Then, to properly understand battery chemistry and the charge-discharge process, LIB structure and the various chemistries will be examined and discussed; this includes a discussion of the charging and discharging processes. Battery pack monitoring methods will then be discussed; the monitored attributes will relay important information about battery pack state of health (SOH) and state of charge (SOC). Existing fast charging protocols will be examined; these methods give insight into the tradeoffs that designers make. The charging protocol and its motivations will then be introduced. The proposed charging protocol is first verified through simulation focusing on the equivalent model of a LIB cell. To realize the charging protocol, a synchronous buck converter was designed, simulated, and fabricated to act as the charging circuit. To properly control the charger, software was designed and implemented; the software is responsible for implementing the charging protocol and maintaining safety through the process. Finally, the results of the experimental evaluation will be examined. This includes a review of the generated data and a destructive inspection of the experimental battery cell.

BACKGROUND AND MOTIVATION

Battery and Charging Terminology

To aid in the discussion of batteries and the charge-discharge process, several terms will be introduced in this section. The terms to be introduced are open circuit voltage, nominal and cutoff voltage, power capacity and energy density, state of charge, depth of discharge, capacity rate, safe operating area, and cycle life.

Open circuit voltage (OCV) refers to the voltage potential across a battery cell or pack when no external load is connected. As battery cells are not ideal power sources, they feature some source impedance; therefore, when the battery cell is loaded, the cell voltage will drop. A battery cell may take tens of minutes to reach its steady state OCV after having been discharged [2], [3]. Time, temperature, and discharge current have great effects on the cell voltage and relaxation times required to reach steady state OCV [2], [3]. When considering the OCV of a battery cell these factors must be accurately accounted for.

The nominal voltage represents the voltage that the battery will function at during most of its discharge. The nominal voltage can easily be seen during a discharge, when the voltage of the cell is visualized as a function of time. The relationship can be seen in Figure 1, where the nominal voltage of the cell under test is 3.7 V.

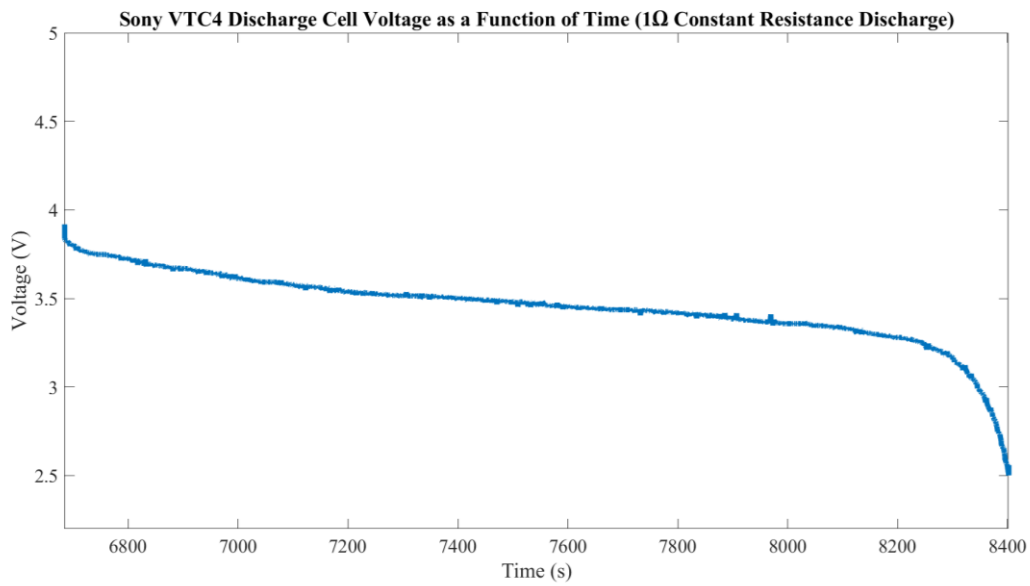

Figure 1: Sony VTC4 discharge cell voltage as a function of time (1Ω constant resistance discharge).

Power capacity illustrates the power stored within a battery cell whereas energy density calculates the power capacity per mass or volume of a battery cell. Power capacity is calculated as in (1):

$$P_{cap} = V_{nom} C_{rated} \tag{1}$$

where V_{nom} is the nominal voltage and C_{rated} is the rated capacity. Energy density can then be found by dividing the power capacity by either the mass to find specific energy density, measured in Watt-hour per kilogram, or by the volume to determine volumetric energy density, measured in Watt-hour per liter.

State of charge (SOC) and depth of discharge (DOD) provide similar information about capacity within a battery cell. SOC represents “how full” a battery cell is whereas DOD illustrates how much of the cell’s capacity has been discharged. A battery charged to its full

capacity has 100% SOC and 0% DOD while a battery that is fully discharged will have 0% SOC and 100% DOD. SOC is often determined through an integrative method as seen in (2).

$$SOC(t) = SOC_{init} + \frac{1}{C_{nom}} \int_{t_0}^{t_0+\tau} I_{battery}(t)\, dt \tag{2}$$

SOC_{init} is the known initial SOC, C_{nom} is the nominal capacity, and $I_{battery}$ is the current into or out of the battery cell. A loss current can also be subtracted from the battery current, as not all current into the cell will be converted to chemical energy and some current is lost within the resistive elements of the cell during discharge. DOD is also calculated using (2), but we will only make use of DOD during a discharging action, so the battery current, $I_{battery,}$ is assumed to be negative. SOC provides a large amount of information, often acting as an independent variable for several other aspects of a lithium ion cell. This enables researchers to understand how batteries change during charging and discharging.

Capacity rate, often shown as a number followed by a capital "C", denotes an input or output current that is then proportional to the capacity of the battery cell or pack in question. For example, if a 2000 mAh cell is to be charged with a maximum of 1C, then the maximum charging current should not exceed 2 A. This helps manufactures normalize and generalize their charging and discharging recommendations.

The safe operating area (SOA) of a battery cell defines the range that a battery should be operated in. In general, the SOA is defined by temperature, cell voltage, charging rate and discharging rate. If a cell reaches too great a temperature, expanding gasses can cause the cell to rupture, exposing flammable electrolyte to air. If cells operate at two low a temperature, material is removed from the normally reversible charge-discharge process, limiting the cell's lifetime.

Operating the cell at a voltage greater than the cut-off voltage can cause thermal runaway and fires, while operating at too low a voltage can damage a cell such that it cannot be recharged. These damages include chemical instabilities and structural damage of the active materials. Finally, the charging and discharging rate maximums must be observed. High currents can lead to increasing temperatures and thermal runaway as the charge transport and diffusion within the cell becomes unbalanced. This leads to lithium dendrite formation, removing cyclable lithium ions from the process and creating the possibility of a short circuit. Keeping a cell within its SOA is very important in ensuring longevity and cell durability.

The cycle life of a cell is defined by the number of charges and discharges, known as cycles, that a battery can accomplish before the working capacity drops below 80% of the original or manufacture stated capacity. This is referred to as state of health (SOH), which denotes how much a battery has degraded over time by dividing the original capacity by the working capacity. SOH and cycle life are an important benchmarks in battery testing as a battery with less than 80% SOH is considered “dead”. This allows researchers and designers to evaluate their charging protocols or discharge loads over many cycles to help understand how they affect the long term health of the battery.

With the basic terms of LIBs described, the structure will now be surveyed. The structure of LIBs defines their functions and limitations. There are also many different materials that are chosen in constructing LIBs; the impact of choosing these materials will be examined as well as their advantages and disadvantages.

Lithium Ion Battery Structure Discussion

Lithium ion cells are made up of three main components: anode, cathode, and electrolyte [4], [5]. The cathode is the positive electrode, and the anode is the negative electrode. These two are separated by an electrolyte, which is typically a liquid [4]. Within the electrolyte, there is a separator. The separator is intended to isolate the two electrodes and prevent a short circuit, as within the LIB structure, the anode and cathode are typically only separated by a few millimeters. The electrolyte and separator are permeable to lithium ions, allowing them to move between the anode and cathode during charge and discharge [1], [5]. When a cell is in a fully discharged state, the lithium ions are held within the cathode as illustrated in Figure 2(a).

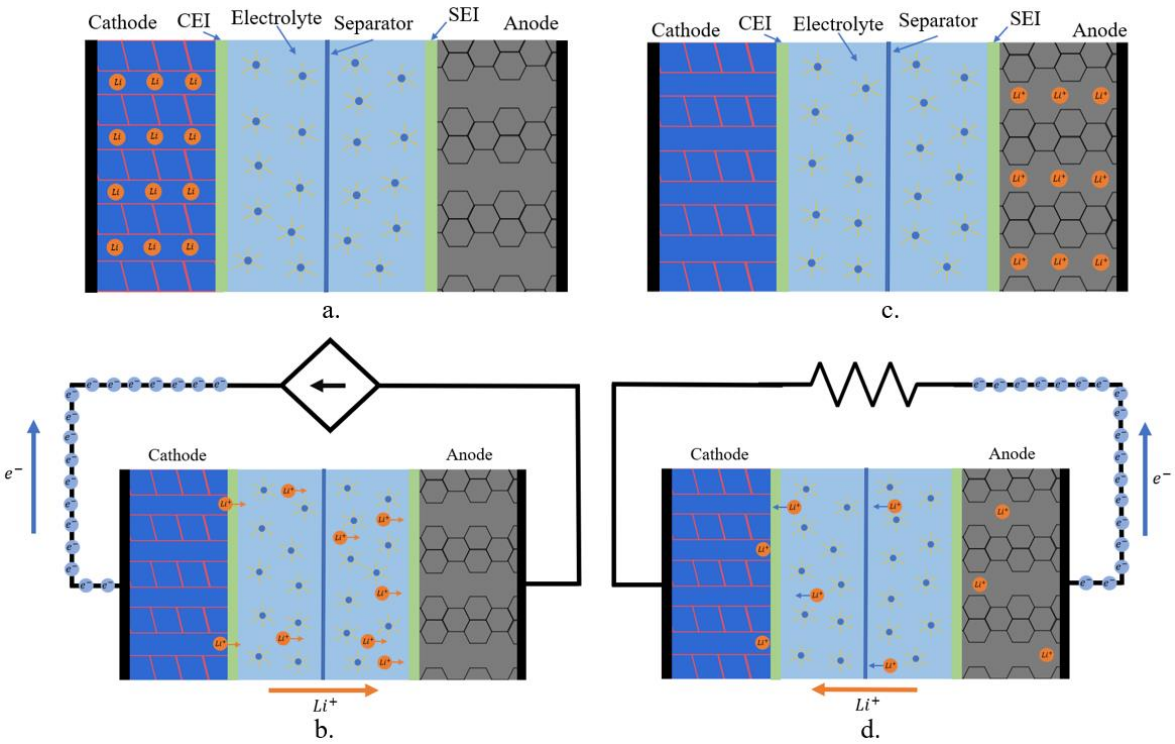

Figure 2: Lithium ion cell structures while (a) fully discharged, (b) charging, (c) fully charged, and (d) discharging

When charging, the ions move from the cathode to the anode by way of the electrolyte, this is shown in Figure 2(b). As the cell reaches a fully charged state, the lithium ions have intercalated into the anode structure, shown in Figure 2(c) as a graphitic structure. Finally, during discharging, the lithium ions move back to the cathode as shown in Figure 2(d).

These individual components will now be examined in more detail. This includes a survey of anode materials, a discussion of cathode materials and properties, and a description of the electrolyte. The solid state electrolyte will also be inspected as this is an emerging technology. The charge and discharge process for lithium ion cells will be described throughout.

Anode

In a lithium ion cell, the anode is responsible for storing lithium ions during and after charging [6], [7]. A typical anode is made up of a carbon structure, usually graphitic carbon pasted on copper foil [5]–[8]. The copper foil acts as a current collector [5]. The layered structure of graphitic carbon allows for lithium ions to intercalate into the anode and be stored. This intercalation forms a lithium carbon intercalation compound [7], which is a reversible process described by (3).

$$xLi^{+} + xe^{-} + C_n \leftrightarrow Li_xC_n \tag{3}$$

During the first charge of a lithium cell with a carbon-based anode, a solid electrolyte interface (SEI) layer is formed on the anode [6]. The SEI isolates the anode and electrolyte and contributes to cell impedance parameters [6]. The SEI layer is permeable to the lithium ions but can offer increasing impedance during charge and discharge if the cell is overcharged or exposed to extreme low temperature. It represents the main aging mechanism of the anode [6]. If a cell is overcharged or charged at low temperatures, lithium ions can be reduced to metallic lithium and

deposited at the anode interface [9], as the ions cannot instantly be inserted into the carbon structure [10]. This can create metallic lithium dendrites on the anode surface, destroying the SEI layer, removing cyclable lithium ions from the cell, and possibly causing a short circuit between the anode and cathode [9], [11], [12]. These phenomena are all to be avoided as they will decrease the lifespan of the cell and cause serious safety issues.

During discharge, lithium ions move from the anode, through the SEI layer and electrolyte, back to the cathode [6]. During this process, the impedance of the SEI layer, as well as charge transfer resistance and resistances related to charge diffusion, will contribute to heating of the cell and inefficiencies. The lithium ions then intercalate into the cathode structure [9]. The intercalation into the cathode structure depends on the materials used to form the cathode.

Cathode

Within a lithium ion cell, the cathode serves as a lithium ion donator. Lithium ions can intercalate and de-intercalate from the anode structure, allowing for reversable processes. [4]–[6]. This allows LIBs to be rechargeable. The electrode material chosen determines the nominal voltage potential of the cell [6]. Cathode materials vary in terms of conductivity, temperature stability, cost, specific and volumetric capacity, and many other qualities. Similar to the anode, the cathode materials are pasted on aluminum foil, which is utilized as a current collector [5]. Similar to SEI on the anode, a cathode electrolyte interphase (CEI) layer is also formed. The discussed technologies will be Lithium Cobalt Oxide (LCO), Lithium Iron Phosphate (LFP), Lithium Manganese Oxide (LMO), Lithium Nickel Manganese Cobalt Oxide (NMC), and Lithium Nickel Cobalt Aluminum Oxide (NCA). These materials are separated into three distinct classes illustrating their structure. The first is layered, which supports fast two-dimensional

lithium ion diffusion and high lithium conductivity [13]. Second are spinal structures; these structures enable three dimensional lithium ion diffusion, and lithium ion conduction with the lowest energy barrier and high stability [13]. The final class is polyanion oxides. This oxide class presents a higher operating voltage, nearly 5V, which is greater than simple oxides [13]. The previously listed cathode materials will now be examined and discussed.

Lithium Cobalt Oxide. Lithium Cobalt Oxide (LiCoO2), or LCO, is a cathode material that initially enabled mass production of lithium ion cells [5]. It is included in the class of layered oxide cathodes [13]. It also offers structural stability and high conductivity [6], [13], this enables fast charging and discharging with good cyclability results [13]. This cathode is paired with a graphite anode [13], [14] and the practical specific capacity is limited to 140 mAh/g [6], [13]. LCO shows a practical volumetric capacity of 550 mAh/cm3 [15]. While LCO allowed the initial breakout of lithium ion cells, it struggles to keep up with cyclability of new technologies, with a cycle life ranging from 500-1000 cycles [14]. LCO also exhibits a low thermal stability and poor load capabilities [14].

Lithium Iron Phosphate. Lithium Iron Phosphate ($LiFePO_4$), or LFP, is a cathode material chosen for its stability, high cycle life, resilience against high temperatures, and ability to handle overcharge [6], [14], [16]. It takes the structure of a polyanion oxide [13] and is paired with a graphite anode [14]. While this material is more rugged when compared to LCO, it suffers from a higher self-discharge, and lower electrical conductivity [7], [14], [17]. The specific capacity ranges from 120 – 165 mAh/g [18] and volumetric capacity is found to be 589 mAh/cm^3 [15]. The safety and ruggedness of this material allows it to compete with seemingly superior

technologies and modified versions of LFP have led to success for a technology start-up [6], [16]. This cathode enables cells to achieve a cycle life of about 2000 [14].

Lithium Manganese Oxide. Lithium Manganese Oxide (typically $LiMn_2O_4$), or LMO, is a cathode technology selected for its low internal resistance, fast charge characteristics [12], [13], and price [13]. It is classified as a spinal oxide [13]. LMO is paired with a graphite anode [14] and considered a greener alternative to LCO [1]. When compared with LCO, LMO shows better fast charge and load characteristics [13], [14]. LMO suffers from poor cyclability, ranging from 300-700 cycles [14] and lesser practical specific capacity of 120-130 mAh/g in commercialized cells [13], [15]. LMO offers a volumetric capacity of 596 mAh/cm^3 [15]. While LMO is not typically used in the present, it led to an important derivative, NMC [14].

Lithium Nickel Manganese Cobalt Oxide. Lithium Nickel Manganese Cobalt Oxide ($LiNiMnCoO_2$), or NMC, is considered a premiere cathode technology. It is included in the layered oxide class [13]. It is utilized for high energy processes including EV drive trains and power applications [14]. It is favored for its capacity, energy density, and cyclability [14]–[16]. With a specific capacity of 170 mAh/g and a volumetric capacity of 600 mAh/cm^3 [15], NMC surpasses previously discussed technologies. NMC can also attain 1000-2000 cycles [14]. While the cyclability can be matched by LFP, NMC sports much higher specific and volumetric capacities. NMC is created by blending LMO technology with cobalt and nickel [13], [14]. Nickel features a high specific energy but has poor stability [13], [14]. This poor stability is solved using manganese, as it creates a more stable structure and assists the incorporation of nickel into NMC [13], [14]. NMC also shows a greater thermal stability than NCA [16]. NMC was the overwhelming choice of EV manufacturers in 2017 [5].

Lithium Nickel Cobalt Aluminum Oxide. Lithium Nickel Cobalt Aluminum Oxide ($LiNiCoAlO_2$), or NCA, is similar, in terms of performance, to NMC. It boasts strong specific and volumetric capacities [14], [15], but a lower cycle life and worse thermal stability [14]. This material has a layered structure [19]. Although NCA has the greatest specific and volumetric capacities, of the discussed cathode materials, with 200 mAh/g and 700 mAh/cm^3 [15], its poor cycle life of around 500 [14] may dissuade use in EVs. Tesla is the only mainstream EV manufacturer relying on this technology which shows only average specific range when compared to several commercial EVs [5]. NCA is susceptible to thermal runaway due to overcharging [14]; this poor thermal stability is due to structural degradation via phase transformations [19].

Cathode Materials Summary. NCA and NMC show superior volumetric and specific capacities but exhibit some limitations in their requirements of rare earth metals. LFP is an interesting technology offering ruggedness to overcharge, thermal stability, and cheaper raw materials. While LMO and LCO fall short of other cathode technologies, they provided important steps to more advanced materials.

Electrolyte

The electrolyte is typically made up of lithium salts in an organic solvent [1], [6], [8]. Typical lithium salts such as $LiPF_6$, $LibF_4$, $LiAsF_6$, $LiClO_4$, $LiCF_3SO_3$ are used as electrolytes in lithium cells [6]. The inclusion of the lithium cation increases the lithium mobility of the electrolyte [5]. These materials are flammable and toxic, requiring attentive use of lithium ion cells [5], [6], [8]. $LiPF_6$ stands out as safe and ionically conductive but can react with water to form hydrogen fluoride [6]. This process takes place as the $LiPF_6$ breaks down into LiF (s) and

PF_5 (g) due to heating. PF_5 can then react with water, an unintended impurity, to form hydrogen fluoride as per (4) [20].

$$PF_5 + H_2O \rightarrow 2HF + PF_3O \tag{4}$$

This process can be mitigated by thermally monitoring charging and discharging cells. Alternatively, faults can be caused by mechanical failures of the SEI layer, exposing the electrolyte to the cathode; this can happen at temperatures of 70°C to 100°C [8]. Other issues caused by external factors, such as mechanical penetration or overcharge, can result in rapid heating of the cell and thermal runaway, where the cathode decays releasing oxygen that recasts with the electrolyte. This process can easily cause dangerous fires [5], [6]. To avoid these failures, it is important to choose electrolytes that can withstand the different environments present at the electrodes, are stable within the operating temperature range, and can tolerate the voltages of the cell [6]. It also important to consider the formation of the SEI layer between the electrolyte and the anode; stabilizers can be added to improve the quality of the SEI layer [6]. One such stabilizer used is 2, 2-Dimethlethenylboronic acid (DEBA), which was found to be able to handle the volume expansion of a graphite lattice during charge, as well as improve columbic efficiency, rate capability and cycling stability [21].

Solid State Electrolytes. As an alternative to typical liquid electrolytes, solid state electrolytes (SSE) have been proposed. The aim of these materials is to address several shortcomings of liquid electrolytes. These include possible exposure to toxic chemicals, mitigation of thermal runaway, and the minimization of side reactions [22]. SSEs also present the ability to greatly increase the energy density [22]. The conductivities of some solid materials are comparable with traditional electrolytes and are able to provide a greater working temperature

range [22]. Realizing SSE technology would allow for further minimization of portable technology, but several challenges are currently preventing full commercialization. SSEs suffer from poor interface contact with the electrodes. The interface becomes solid to solid, rather than solid to liquid, so the SSE cannot wet the electrodes and therefore provides a greater impedance [22]. This can also provide worse rate capability, coulombic efficiency, and cycle stability [22]. $Li_7La_3Zr_2O_{12}$ (LLZO) based electrolytes have shown promise due to high lithium-ion conductivity and stability in relation to lithium metal [23]. Sadly, the LLZO based electrolyte is unstable in moist air and can react to generate a surface layer featuring an ultralow lithium-ion conductivity, but this can be mitigated in several ways as presented in Reference [23]. While SSE present a clear path to an exciting future technology, several factors are preventing this technology from reaching full scale adoption.

Electrolyte Survey Summary. The electrolyte layer present in lithium ion batteries currently present several issues. They pose fire risks if exposed to air and can violently react with released oxygen from the electrodes during high temperature faults. Some of these issues can be mitigated using a SSE, but this technology has not yet reached market maturity; therefore, liquid electrolytes still present the best case for practical use and experimentation. To manage the liquid electrolyte properly, several factors must be monitored. These include voltage potential, temperature, and state of charge. Monitoring these quantities will also serve to keep a healthy separator layer. Ensuring that these variables remain in their proper regions will grant safe operation of lithium ion cells.

Separator

Located within the electrolyte is the solid separator, which prevents the electrodes from touching one another and is permeable to the lithium ions [6]. Like the electrolyte, the separator must be mechanically and chemically stable in the operating range of the cell [6]. When a liquid electrolyte is chosen, typical separator materials are microporous polyolefin and polyethylene (PE) [5], [6]. While this layer is permeable to lithium ions, during excessive heating, it can fail such that it loses its permeability, resulting in the opening of a possible short circuit acting as a safety element [5]. While the separator is not an electrochemically active portion of the lithium ion cell, it can still contribute to degradation in the cell. Low ionic conductivity can contribute to overpotential of the cell leading to lithium dendrite formation [24]. As with all impedances within the cell, decreasing their magnitude can improve cell performance [24]. This can be done by ensuring separator homogeneity, ensuring proper temperature range, and limiting lithium dendrite formation [24]. The lithium dendrites can block separator pores or enter the porous separator network [24]. Just as all elements of the lithium ion cell, the separator will impact performance. Ensuring that the cell stays within its proper operating range will solve the larger problems associated with separator impedance and wear.

Cell Structure Summary

Cell components and structure not only dictate the operation and parameters of LIBs but are huge focuses for researchers. Each aspect can aid LIBs in becoming smaller and more efficient. Anode technologies are currently centered on graphitic materials, but some emerging technologies are focusing on silicon based materials with carbon additives. Cathode technologies are one of the main focuses in LIB research, they have a large impact on the energy density,

cycle life, and safe operating area. Currently NMC and NCA are the focus of EV manufactures as they offer the highest energy densities of the surveyed materials and the relatively high cycle lives. The electrolyte used in LIBs aims to have high lithium ion conductivity while remaining safe. The electrolyte poses a large safety risk when cells are punctured or mistreated as the electrolyte can react violently with moisture to cause fires. SSEs is currently being studied as an alternative to the typical liquid electrolyte but has not yet reached market maturity. The SSE can offer safer operation and the elimination of the SEI layer but suffers from solid-solid contact with the electrodes, offering a greater impedance than the typical liquid-solid interface. Contained within cells utilizing liquid electrolytes, the separator provides physical isolation between the anode and cathode. Just as the other components of the LIB, ensuring that the separator is not damaged will assist in keeping the impedance of the LIB low; this is accomplished by keeping the LIB within its SOA. The separator can also function as a safety measure when the cell begins to malfunction as it can fail such that it loses its ionic permeability, blocking lithium ions from moving between the electrodes.

With the structure and theoretical cycling process of a LIB described in detail, the practical aspects of cell monitoring can be examined. As mentioned previously, to avoid cell aging and degradation, LIBs must be kept within their SOA. This requires careful consideration of cell SOC as this gives clear indications for the current parameters governing the LIB. As there are many methods of determine cell SOC, it is important to understand the advantages offered by each method.

SOC Determination Methods

To properly fast charge LIB cells, several cell parameters must be monitored or calculated. These parameters include, but are not limited to, cell voltage, temperature, current, and SOC. Cell voltage and current will allow for SOC calculations to take place while temperature will ensure that the cell is within the SOA. The most important of these parameters is SOC, which can be determined through an integration of the current into the cell as a function of time plus an initial condition. The integration method is the basis for nearly all SOC determination techniques but offers some issues. Therefore, several other SOC calculation techniques have been developed and tested. These methods showcase a range of complexity and are not mutually exclusive. Several methods will now be described and examined. These methods are the open circuit voltage method, machine learning algorithms, the Kalman filter, Coulomb counting, and enhanced Coulomb counting.

Open Circuit Voltage / Cell Voltage

Cell voltage can be utilized to determine SOC as there exists a clear relationship between cell voltage and SOC [1]–[3]. Using experimental data and known battery parameters, a look-up table (LUT) can be developed relating cell voltage and SOC.

The relationship between cell voltage and SOC is greatly affected by many aspects including, discharge load [3], cell temperature, and rest time [2]. Due to the source impedance of LIBs, different load currents will create different cell voltages [3]. This means that a successful LUT must incorporate a dependence on the discharge current to compensate for the loaded cell voltage at high (>5C) discharge currents [3]. Temperature also plays a role in both the cell voltage and the apparent discharge capacity [2], [3]. The US18650VTC4, a typical rechargeable

lithium ion cell and the one studied in this thesis, has a discharge capacity that shows a clear dependence on ambient temperature affecting a potential reliance on the cell voltage [3]. Finally, the cell voltage can be affected by the length of rest since either charging or discharging. Reference [2] shows that a cell may take 30 minutes to relax to a steady voltage after a discharge step and up to 600 minutes to relax to a point where the OCV to SOC relationship becomes precise again. Due to cell voltage dependencies on many factors, it is not a reliable indicator for online SOC estimation.

Machine Learning Algorithms

When models of complex systems are required, machine learning techniques can be excellent at deciphering difficult transfer functions characteristics. As the SOC of a battery cell is not directly measurable, machine learning algorithms are well tooled for estimation. Using large sets of training and model reinforcement data, the algorithms can be trained to accurately estimate SOC.

Several methods are proposed in Reference [25]. These algorithms include Artificial Neural Networks, Support Vector Machines, Gaussian Process Regression, Linear Regression, Ensemble Bagging, and Ensemble Boosting. While these methods are shown to be effective, several drawbacks must be noted. The first is required training data. To train the algorithms, large datasets are required [25]; these datasets must feature the same parameters as the system to be estimated. Collecting data converting all zones of operation, specifically for an EV, is considered nearly impossible [26]. An important aspect of SOC estimation techniques is the ability to estimate the SOC during operation. As machine learning algorithms require large amounts of computation [25], they may be disqualified from online operation [27].

Unscented Kalman Filter for SOC Estimation

Utilizing battery model parameters and closed loop estimation, the unscented Kalman filter (UKF) can be applied to estimate battery SOC. First, battery parameters can be determined experimentally. These parameters include internal battery impedance at different operating points as well as the OCV and SOC relationship [26]. These data will provide the basis for the estimation. Linear averaging can then be used to calculate several correction factors. These correction factors are used to control for cell resistance while current is entering or leaving the battery cells [26]. Using the derived parameters and correction factors, the UKF can then be formed and offers a closed loop method to estimate SOC [26].

While the UKF does offers a compelling method for estimating SOC, several factors may limit its performance in relation to other SOC methods. First, battery parameters must be known. This requires offline measurements which are not always available. Second, complex computing is required. While Reference [26] presents an online test, a personal computer (PC) is required and the sampling period is one second; these speeds are not acceptable for online monitoring. Kalman filtering has been shown to have $O(n^3)$ time complexity [27], requiring immense computing power and time. Without a powerful computing unit, online use of the UKF may not be possible.

Coulomb Counting

Coulomb counting is a method where the current into or out of the battery cell is measured and then integrated over time [27], [28]. The formula for calculating the SOC is illustrated in (5).

$$SOC(t) = SOC_{init} + \frac{1}{C_{nom}} \int_{t_0}^{t_0+\tau} I_{battery}(t)\, dt \tag{5}$$

Where SOC_{init} is the known initial SOC, C_{nom} is the nominal capacity, and $I_{battery}$ is the current into or out of the battery cell. A loss current can also be subtracted from the battery current, as not all current into the battery cell is converted to charge capacity [27]. Coulomb Counting offers a computationally light and relatively easy method of calculating SOC by measuring capacity in and out of the battery cell [27]–[30].

Several complications accompany Coulomb counting. While it is computationally light, error easily clouds the SOC calculation. Over long periods of operation, error will begin to accumulate [27]. This is due to the implementation of Hall Effect sensors or current sense resistors; the precision of this method is limited by the physical error shown in these components [31]. The sample-and-hold phenomenon is also introduced. Within the system that tracks the battery SOC, continuous time signals are converted to discrete time signals with a sampling period. The current is sampled, and the computations then take place; these computations are not immediate. Therefore, one sample is assumed to represent a period when the current may vary introducing error into the system. This problem worsens with the increase of the sampling period. Coulomb counting on its own is not acceptable for online operation due to the accumulated error.

Enhanced Coulomb Counting

To supplement the integration-only method of coulomb counting, the enhanced coulomb counting (ECC) method is utilized. This method adds one or more calibration points to the coulomb counting technique [27], [30]. These calibration points stem from the OCV of the cell

which can provide accurate calibration points if other variables are held somewhat constant (temperature and current out of the cell). These calibrations usually take place when the cell is fully charged or fully discharged as these are often known points taken from the battery datasheet.

In this thesis, the ECC method is used. This is motivated by several choices. First, the computing unit chosen is a microcontroller. While more complex algorithms could be implemented, the ECC method is fast, accurate, and produces consistent cycle-to-cycle results with lowered computation needs. The microcontroller will also be tasked with computing the required charging current in addition to monitoring cell voltage, current, and temperature so lowering cycles devoted to SOC calculations will benefit the other required aspects. Secondly, as the cell under test is charged and discharged with the same method each cycle, ECC presents the best estimation method. As there is no meaningful difference in the charging and discharging curves, there is no need to compute correction factors or to measure the cell equivalents to understand how the load current will affect the cell voltage.

Existing Fast Charging Methods

Many fast charging methods exist currently. These methods work to improve on the typical constant current / constant voltage (CC/CV) method where a cell is charged at a predefined current level until the cell voltage reaches a cut-off. The cell is then charged at a constant voltage until the charging current drops below a set value. This is a slow process as the constant current section of the charge is often limited to 1C and the lower limit set for the charging current in the constant voltage section is typically set at C/10 to C/25. A typical 1C CC/CV charge requires 50 minutes to reach 80% SOC and 2 to 4 hours to reach 100% SOC. This

is often unacceptable for several reasons. CC/CV charging is slow, often requiring hours to complete a 1C charge. Fast charging protocols will often work to balance short charging times with cell heating and lithium plating, as these are the two main degradation factors in lithium ion cells. The methods surveyed will be pulse charging, boost charging, varying current charging, and multi-stage constant current charging.

Pulse Charging

Pulse charging is a fast charging technique that attempts to limit lithium concentration at the SEI layer [10]. During a typical CC/CV charging process, the lithium concentration will become saturated once the cut-off voltage of the cell is reached [10]. To avoid lithium saturation at the anode and to shorten charging, a pulse charging technique was developed. Pulse charging is realized by charging cells at moderately high constant current rates for a set period, followed by a relaxation period. The current pulses and rest periods serve to balance the formation rate of the lithium at the anode surface and the diffusion of the lithium into the graphite anode [10]. The lithium ions can intercalate into the graphite structure, avoiding the possible formation of lithium dendrites. In addition to the rest times, some pulse charging approaches incorporate discharging pulses, which work to actively decrease the lithium concentration at the anode surface during the charging process [10]. An example of the pulse charging method, with integrated discharge pulses, is illustrated in Figure 3.

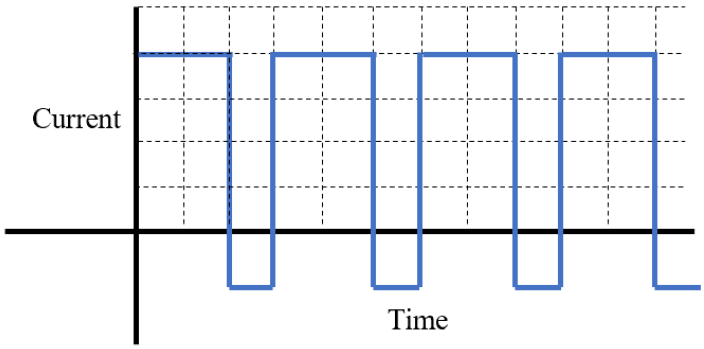

Figure 3: Example of charging current created during the pulse charging protocol

While pulse charging may offer an approach to avoid lithium plating, optimization toward the charging process is neglected. Incorporating rest periods in charging slows the charging process where a more sophisticated algorithm could avoid reaching the saturation level during the charging process. Continually charging at high currents, even with an incorporated rest, can cause the cell to reach high temperatures as thermal equilibrium may not be reached during the rest period, especially if the rest periods are relatively short. The incorporation of a discharge pulse may not only worsen the thermal performance but is energy inefficient and impractical to implement in a commercial battery charger.

Boost Charging

Boost charging utilizes conventions similar to the typical CC/CV charging process but using two constant current portions and a final constant voltage portion [32]. In this fast charging technique, cells are charged at 4C until the cut-off voltage is reached. This portion of the charge contributes approximately 90% of SOC. Then the charging current is reduced to 1C, decreasing the cell voltage to a level below the cut-off voltage. The cell is charged at 1C until the cut-off voltage is reached again. The charging is then finished with a constant voltage portion for five

minutes [32]. The time required for the cell to reach 100% under these charging conditions is measured to be approximately 20 minutes [32]. The cathode material used in this study is LFP. Paired with a 4C constant current discharge, Reference [32] finds that the discharge capacity decreases by only 14% after 4500 cycles. Boost charging, as presented in Reference [32], shows impressive results for fast charging. An example boost charging current is illustrated in Figure 4.

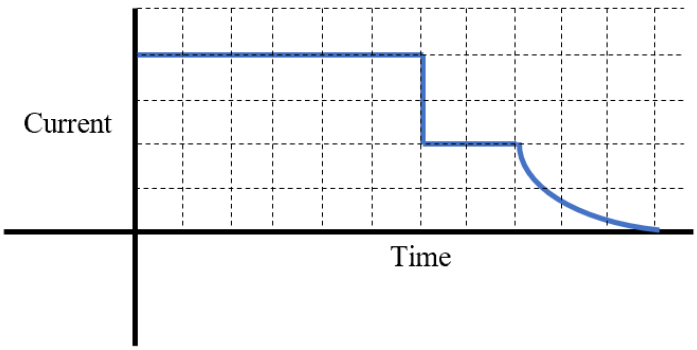

Figure 4: Example of charging current created by the boost charging protocol

Boost charging dictates that a cell with a low SOC be charged with a 4C charging current. Reference [32] presents internal resistance data as a function of SOC. These data illustrate a low internal resistance from 0% to 10% SOC, in the range of 5mΩ to 15mΩ, followed by a constant resistance from 10% to 55%, approximately 15mΩ, and then an exponentially increasing resistance from 50% to 100% SOC with a final value of nearly 27mΩ. These data were calculated during the charging of the cell using the potential across the cell and the applied charging current. The cell is not characterized using electrochemical impedance spectroscopy (EIS). Reports [11] and [29] show that the internal resistance of various lithium-ion cells is greater at lower SOC, below approximately 15%. Measuring the cell resistance in this way results in unrealistic values as the calculated resistances values will be influenced by the OCV

potential and fail to capture events at the electrode interface such as lithium ion diffusion. This is a slow electrochemical process which constitutes a significant portion of the cell impedance. Cell impendence measurements should not take place while charging and should be conducted using EIS. Due to high cell impedance at low SOC, charging with initial currents of 4C for a relatively long period would cause vast temperature increases in a commercial charger. This is due to a potential lack of ambient temperature control as described in Reference [32]. This can be damaging to the cell in realistic use cases.

Varying Current Profile

The varying current (VC) profile focuses on the cell impedance as a function of time and attempts to minimize the charging time and generated heat [12]. As shown in references [11] and [29], cell impedance is greatest at low SOC, and shows a fairly constant profile above 15% SOC. To avoid generating large amounts of heat during low SOC periods, the VC profile features a low but increasing initial current. Once the cell has been charged past the high-impedance, low SOC section, the charging current reaches a peak and then begins decaying exponentially. The constants that determine the shape of the initial rise and subsequent exponential decay are calculated through an equivalent circuit and optimization choices. The derived charging current is capable of charging 2.2 Ah cells to 100% SOC in one hour [12]. An example charging current is illustrated in Figure 5.

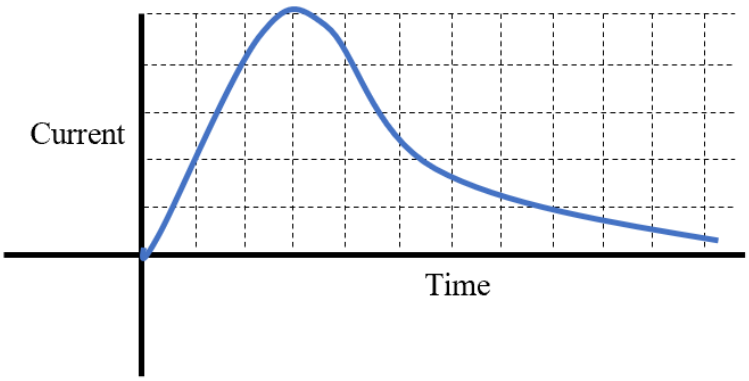

Figure 5: Example of charging current created by the boost charging protocol

While the VC method does work to avoid charge high impedance cells with high currents, the time taken to do so is too great for fast charging. The cell is also held close to the cut-off voltage for approximately 1/3 of the charging time which encourages cell aging and consumption of active materials [11]. The implementation of this charge protocol would also require measurement of cell parameters while the cell is in use to adjust the charging method to suit the cell health [12].

Multi-Stage Constant Current Charging

Multi-stage constant current (MCC) charging is a method that features several descending levels of constant current charging. To calculate the discrete charging current, circuit modeling, experimentation, and optimization techniques were used [33]. This method presents higher energy efficiency, shorter charging times, and less temperature variation when compared to the traditional CC/CV charging [33]. An example is shown in Figure 6.

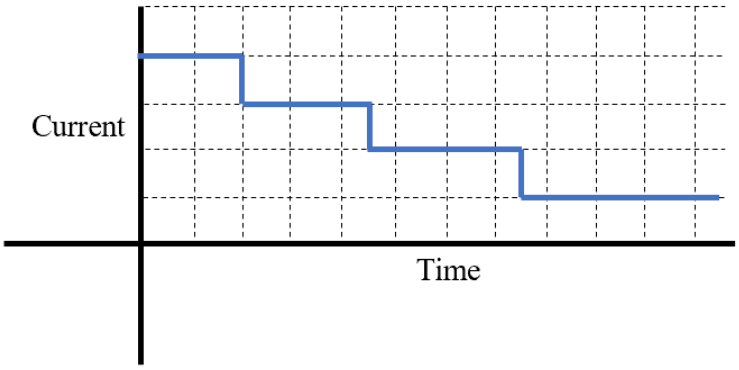

Figure 6: Example of charging current created by the multi-stage constant current protocol

While the MCC method may present an interesting technique for optimizing the charging processing, several important factors are neglected. Cells are almost immediately pushed close to the cut-off voltage and then continually charged with high currents. This is known to encourage the evaporation of the electrolyte and unwanted side reactions within the cell [11], [34] .To implement this charging technique, complex algorithms are required, and lithium plating is only briefly considered in not having a high charging current at a low SOC [33] .

Fast Charging Methods Summary

Several fast charging algorithms are surveyed in this section, they include the pulse, Boost, VC, and MCC charging techniques. Pulse charging works to limit the lithium ion concentration at the anode surface by supplementing high current charging pulses with rest periods allowing for intercalation into the anode structure. While this method offers strong electrochemical results, it is impractical to implement as it is energy inefficient. Boost charging considers electrochemical events, and the protocol is practical to implement, but several considerations were not made in testing the method. This includes ideal lab settings and the separation of the battery under test and the charging electronics [32]. A practical fast charging

method must consider how implementation will take place outside of research settings. The VC charging protocol is considerate of cell impedance and SOC but fails to charge cells as fast as other presented methods. It also forces cells close to their cut-off voltages for a large portion of the charging time, which is detrimental to cell health. The MCC method implements discrete, monotonically decreasing constant current charging currents with the goal of fast charging and optimization. This method can produce short charging times but does not consider high cell impedance at low SOC and continues to charge cells with high currents close to their cut-off voltages.

There exist several options for fast charging protocols, each with their own disadvantages. The ideal fast charging protocol will charge cells in the shortest possible time while avoiding active material loss and remaining safe. This protocol must also be tested in realistic use cases, where the cell under test is subject to a realistic charging case including ambient temperatures and proximity to charging circuitry. The charging protocol studied in this thesis will now be introduced. The goal of this charging method is to avoid lithium plating while charging LIBs as quickly and safely as possible. This charging protocol will be motivated electrochemically, simulated, and then implemented using custom power electronics. This derivation and implementation offers a protocol with strong scientific evidence and a realistic implementation.

PROPOSED CHARGING PROTOCOL

To avoid cell aging during fast charging, several considerations must be made: the main being lithium plating. Lithium plating can be avoided by keeping a small positive voltage between the anode and the lithium and lithium ions (Li/Li+) within the cell. A specific charging profile can be created and simulated such that this difference is always positive. This simulation utilizes the equivalent circuit model of a lithium ion cell, whose values can be measured through EIS. This charging current can then be measured experimentally. The difference between the anode and Li/Li+ is held at a small, positive voltage and the resulting charging current is recorded. This is done using a custom three terminal device. Once the measured current has been confirmed, it can be applied to commercial cells utilizing a scale factor that is determined through the ratio of the capacities of the custom cell and the commercial cell. To ensure that massive amounts of current are not forced into the battery at low SOC, the charging current is limited to 3C. This results in a charging protocol featuring a constant charging current until a fitted function calculates a charging current with a value of less than 3C.

This fast charging protocol presents a simple and effective method of fast charging. As the charging current is a function of SOC and cell parameters, it can easily be loaded onto a microcontroller which controls the current into the cell during charging. There is no cycle-to-cycle variation in this method so there is no need to update the charging protocol. Utilizing a simple corrected integrated algorithm for calculating SOC, minimal calculations take place to find the SOC and then the resulting charging current. This error in SOC is corrected by utilizing the cell voltage to determine when the cell has reached 0% SOC.

This process is optimized toward the elimination of lithium plating, which neglects several other issues associated with fast charging. First, the thermal effects of this fast charging protocols are not controlled. Reports [11] and [29] show that cell impedance is greatest at low SOC, so applying an initial charging current of 3C will result in Joule heating of the cell. The cell can reach high temperatures during this high constant current section. But, as this portion of the fast charge is approximately 250 seconds long, the cell does not have the opportunity to reach unsafe temperatures. Secondly, while this algorithm can be used to charge cells to 100% SOC, 80% is chosen as the stop condition for charging. As the last 20% of SOC contributes a large amount of the charging time with only a small increase in charge capacity; this portion is not considered using this algorithm. These are the tradeoffs required for fast charging; cells cannot be charged quickly without some damage taking place. The tradeoffs between cell damage and fast charging must be considered.

Derivation of Proposed Charging Protocol

It is known that lithium plating can only occur when the potential of the graphite anode is negative with respect to the Li/Li+ present within the battery cell. This potential is not directly measurable, so battery cells must be modified or constructed to include a third electrode, often referred to as the reference electrode, enabling the potential of Li/Li+ to be measurable. Commercial cells, which would benefit from fast charging, can be deconstructed, allowing researchers to build small coin-sized cells with three terminals. Using the custom three-electrode device, the constructed battery cell can be charged such that the potential between the third terminal and the anode is held above 0V. This charging current can be recorded and then scaled, proportional to the ratio of the capacities of each cell, from the small coin-sized cell to the

commercial cell. Reference [35] follows this protocol to impressive results, testing in several different temperature ranges and on large LIB packs. While the results are impressive, several features of the described algorithm limit its potential as an online and commercial charging method. First, a look up table (LUT) is used to calculate the charging current meaning that the algorithm may not generalize to cells with different anode chemistries [35]. Secondly, while this method aims to prevent lithium plating through the fact that the potential of the anode versus Li/Li+ in the cell must be kept positive and small in magnitude, no motivation for the shape of the charging current or its origins are offered. The curve is recorded from a coin cell experiment and then scaled to larger packs. Therefore, there is no way to apply this algorithm in a generalized way as the dependence of the charging current on cell impedance or electrochemical events is not captured.

To improve upon this process, the three-electrode device can first be modeled as an electrical equivalent circuit using parameters found through electrochemical impedance spectroscopy (EIS) measurements. These parameter measurements are conducted at several different SOCs, as they are dependent on SOC. This simulated current gives many insights into the charging process and assists in confirming the charging protocol. As opposed to a look-up-table, as presented in Reference [35], the simulated charging current provides a functional relationship between the SOC and the required charging current. This simulated model can also be simplified to resistive elements leading to a simple and easily implementable algorithm. It can be shown that there are only very marginal differences in the simulated current when the system is considered purely resistive.

Generating Lithium/Lithium Ion to Anode Equivalent Circuit Model

To generate the equivalent circuit model, large amounts of experience in electrochemistry are required. Therefore, a post-doctoral researcher, within the Gao Lab Group, completed the following commercial cell deconstruction, test cell assembly, experimental data generation, subsequent destructive examination, and contributed technical advice and expertise. The experimental data includes the chosen equivalent circuit model as well as interpretation of electrochemical impedance spectroscopy results. The data generated and experimental results are the basis for the proposed fast charging protocol. Reference [36] documents portions of this work and is currently submitted to the Journal of Energy Storage pending review. Proof of this submission is included in Appendix E.

First, using materials from a commercial LIB, specifically the Sony US18650VTC4 (VTC4) shown in Figure 7(a), were harvested, and used to construct the three-electrode cell. This includes the anode, consisting of graphite on copper foil and cathode, consisting of NMC on aluminum foil [36]. The commercial cell is first discharged to the discharge cut-off voltage of 2.5V. The cell was then disassembled inside of a glovebox as shown in Figure 7(b); this allows for moisture and atmosphere to be controlled. The upper bounds for moisture and O_2 were 0.5 ppm and 0.1 ppm respectively. Within the glovebox, the anode and cathode were removed from the battery structure and immediately submerged in dimethyl carbonate (DMC) to wash them of electrolyte. They were then dried for 24 h inside of the glovebox. After being dried, the active material from the electrodes was removed using cotton swabs and N-Methyl-2-Pyrrolidone (NMP) and allowed to dry again for 12 h. Next, to create the coin cell sized electrodes, 12 mm discs were punched out inside the glove box. As opposed to fabricating the lithium reference that

would be placed inside of the three-electrode cell, 99.9% pure lithium rings from Sigma-Aldrich were used. A three-electrode split test kit from MTI was then used to house the cell. To form the electrolyte, 1 M lithium hexafluorophosphate ($LiPF_6$) was dissolved in a mixture of ethylene carbonate (EC) and dimethyl carbonate (DMC) (v/v = 1:1) (Sigma-Aldrich, battery grade, ≥ 99.99% trace metals basis). Once completed, the test cells were rested for 24 h before any tests were performed [36]. The final assembled test cell is illustrated in Figure 7(c).

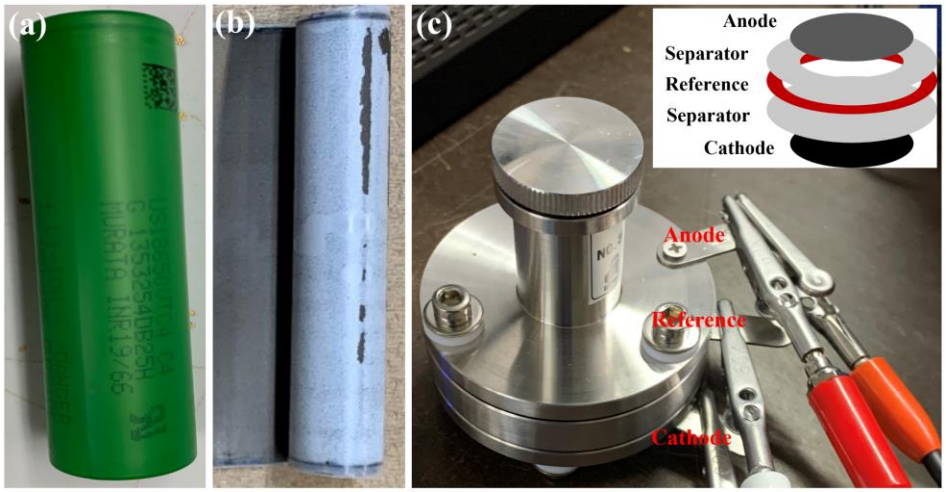

Figure 7: (a) As-received commercial Sony 18650VTC4 lithium-ion battery. (b) Exposed after cell disassembly inside the glove box. (c) MTI three-electrode split cell kit and schematic of the cell component arrangement inside a three-electrode lithium-ion test cell [36]

Electrochemical Impedance Spectroscopy

Before discussing the developed circuit model of the test cell, the technique used to find the equivalent circuit parameters should be discussed; this technique is electrochemical impedance spectroscopy. Electrochemical impedance spectroscopy (EIS) is a measurement technique used to characterize the impedance of a system at different excitation frequencies. In this experiment, EIS is used to measure the elements that will be used to build the eventual circuit model. To gather this data, small amplitude current signals are sent into the system and

the induced voltage is recorded. With these recorded signals, the impedance as a function of frequency can be calculated. This process takes place over many frequencies, typically from several millihertz to hundreds of kilohertz resulting in the data needed to generate both Nyquist and Bode plots. More often, in electrochemistry, the Nyquist plot is used to visualize the generated data as researchers are often familiar with the generated shapes and their corresponding circuit element models.

Developing a Model of the Lithium Ion Battery Cell

Before any experiments were conducted on the three-electrode test cell, five initialization cycles took place. These cycles consisted of a CC/CV charge in the range of 2.5 V to 4.2 V, with a CC rate of C/5 and a cut-off of C/20 during the CV phase. The cells were also allowed a five minute rest period between charge and discharge. The goal of the initialization tests was to measure capacity, determine a known SOC, and to ensure stable operation. These initial cycles were performed using the LBT21084HC Arbin cycler [36].

To then begin the EIS set-up, the Gamry Reference 3000 potentiostat/galvanostat was used. Two measurement modes were chosen; EIS data was recorded using two-electrode configuration and three-electrode configuration. The two-electrode configuration allows for EIS data representing the entire test cell to be captured, as the two electrodes measured are the anode and cathode, while the three-electrode configuration allows the EIS of the anode and cathode to be measured using the reference lithium electrode [36]. EIS tests were conducted with current amplitudes set to 5% of the cell capacity (0.05C) to attain a strong signal to noise ratio (SNR) and to minimize non-linearities that arise from the electrochemical events. The frequency range

was set to 100 kHz to 50 mHz and the EIS tests were conducted from high to low frequencies [36].

As the impedances of the cell vary depending on SOC, EIS and OCV measurements must be performed at different SOC to accurately model the cell. The test cell was first full discharged to 0% SOC. The cell was then charged at CC at a C/5 rate, increasing the SOC to the predetermined points, and allowing for measurements. After a cell was charged to the predetermined SOC, a 3-hour rest took place. This 3-hour rest allows for the cell to reach steady state so that the OCV measurements are accurate [37].

These EIS test data yield very important results, allowing for an equivalent circuit model (ECM) to be fit to the test cell. The EIS tests were conducted at 5%, 10%, 15%, 20%, 40%, 60%, 80%, and 100% SOC. These predetermined SOC values reflect the fact that the characteristics of the LIB change drastically during low SOC and become steadier as the cell grows closer to 100% SOC. The Nyquist plot showing the impedance of the cell as measured from lithium reference to the graphite anode is illustrated in Figure 8(a). The shapes presented in the impedance spectrum allow for a specific circuit model to be fit to the test cell. This ECM is illustrated in Figure 8(b). Most elements used are typical circuit elements, but one unique element is used in this ECM. This element is the constant phase element (CPE) and is analogous to a capacitor but with some notable differences. While the impedance of a capacitor forces a phase shift of π / 2, a CPE creates a phase shift of n * π / 2, where is n found to be between 0.8 and 1 [38]. The impedance of a CPE is given in (6).

$$Z_{CPE} = \frac{1}{Y_0(j\omega)^n} \tag{6}$$

Here, ω is angular frequency, Y_0 and n are the parameters of the CPE. The n parameter gives insight into if the CPE behaves more like a resistor or capacitor. The CPE also gives flexibility in representing electrochemical phenomenon that are not directly translatable to electric circuit elements [38]. The CPE can be translated to a capacitor for simulations and easier understanding, this is done through (7).

$$C = \frac{(RQ)^{\frac{1}{n}}}{R} \tag{7}$$

Where R and Q are the resistance and CPE corresponding to the R-CPE network as shown in Figure 8b [38]. The CPE can then be interpreted as a parallel resistor-capacitor (RC) network.

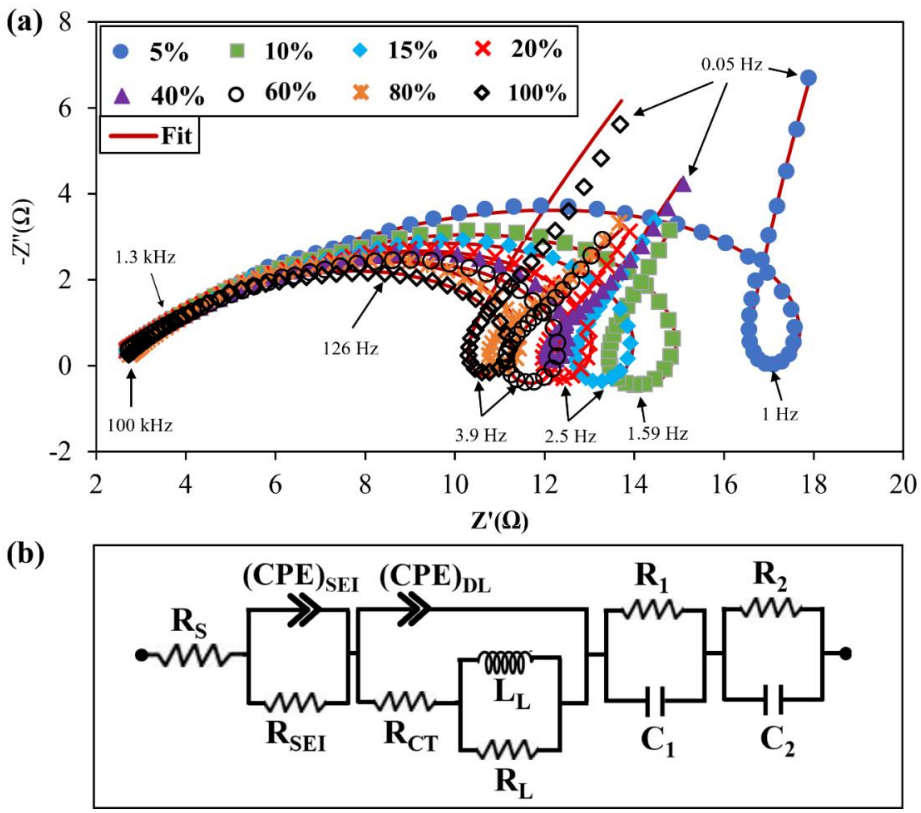

Figure 8: (a) Impedance spectra of the graphite anode measured at different SOCs during the charge. (b) The equivalent circuit model (ECM) used to fit the anode impedance spectra shown in Fig. 8(a) [36]

The physical components and processes that are modeled using circuit components will now be discussed. First, the series resistance component (R_s) models the series resistance of the battery cell; this is mainly the Ohmic resistance of the anode. Then, an RC parallel network is used to model the SEI layer; the included capacitor represents the diffusion process of the graphite anode. Another parallel branch is used to model the charge-transfer resistance (R_{CT}) and capacitances (referred to as the double layer (DL) capacitance). Series with R_{CT}, a parallel inductor-resistor network is used to model the inductive behavior present in the impedance spectrum [36]. The origin of this inductance is thought to originate mostly in the electrolyte of the cell, but many more cell elements may contribute to this inductive behavior [37]. Finally, two parallel R-CPE (R_1C_1 and R_2C_2) networks are used to model the Warburg impedance which is related to the lithium diffusion process [37]. Many of these branches can be combined in series to better approximate the LIB but it is advantageous to choose fewer to ease the required calculations. Using the developed circuit and EIS results, SOC-dependent circuit element parameters can be assigned to the ECM. During this process of the OCP of the cell was also measured. These results are given below in Table 1.

Table 1: Element values according to SOCs obtained after fitting the anode EIS spectra of a small three-electrode test cell using the ECM shown in Fig. 8(b) [37]

SOC (%)	OCP (mV)	R_S (Ω)	R_{SEI} (Ω)	C_{SEI} (μF)	R_{CT} (Ω)	C_{DL} (μF)	L_L (mH)	R_L (Ω)	R_1 (Ω)	C_1 (F)	R_2 (Ω)	C_2 (F)
5	310	2.411	3.167	58.56	12.29	529	508	4.520	23.80	1.108	0.623	0.304
10	209	2.392	3.102	55.45	10.12	869	258	5.340	0.815	0.041	10.35	1.143
15	160	2.396	3.139	50.47	9.088	629	141	4.021	10.71	1.100	0.341	0.597
20	130	2.395	3.014	56.71	8.336	755	135	4.702	7.448	1.053	0.688	0.163
40	105	2.42	3.007	51.44	7.604	577	73	3.526	0.731	0.238	7.610	1.117
60	70	2.448	2.949	56.28	7.370	660	62	3.751	0.792	0.681	7.625	1.070
80	56	2.439	2.809	58.78	6.656	605	118	4.606	8.834	1.407	0.847	0.891
100	37	2.513	2.706	59.79	6.552	816	119	3.181	9.075	1.028	1.587	0.109

These values were then used to build a simulation of the test cell. This simulation gives insight into the actions of different component models and how they can be simplified.

Small Cell Equivalent Circuit Simulations

As in Reference [35], the fast charging experiment was conducted to allow for comparison to simulation results. Using the test cell and the Gamry Reference 3000 potentiostat/galvanostat, a charging current was created with the goal of maintaining 10 mV

between the third electrode and the anode. This dataset will be compared to simulation results. These data are also used to model the OCV as a function of SOC, providing extremely important information. A function can be fit to this relationship, this fit is illustrated in Figure 9 and in (8). This function is directly used in simulation.

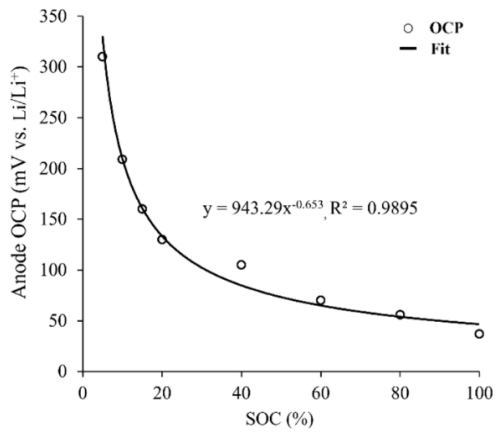

Figure 9: The anode open circuit potential measured at various SOCs [36]

$$OCP(SOC) = 943.29 * SOC^{-0.653} \tag{8}$$

The simulated system models the ECM between the third electrode, the Li/Li+ reference, and the anode. This model incorporates both the ECM as illustrated in Figure 10, and a dependent voltage source to model the OCV as a function of SOC.

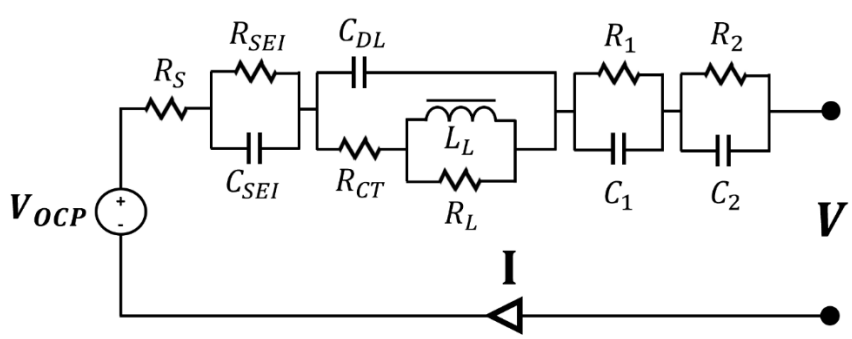

Figure 10: Electrical circuit model for predicting a fast-charging current for a LIB test cell

The system was simulated in MATLAB and Simulink using the Specialized Power Systems tool set. This tool set gives access to passive and active electrical components as well as controllable power sources. Resistor (R), capacitor (C), and inductor (L) circuit elements are represented by the Series RLC Branch which allows for any series combination of RLC circuits to be modeled. Controllable voltage and current sources are used to model the charging current and OCP. Proportional control is used to maintain the required voltage across the Li/Li+ terminal. This Simulink model is illustrated in Figure 11. All component values were set according to Table 1 and the recorded data was transferred to the MATLAB workspace for better visualization.

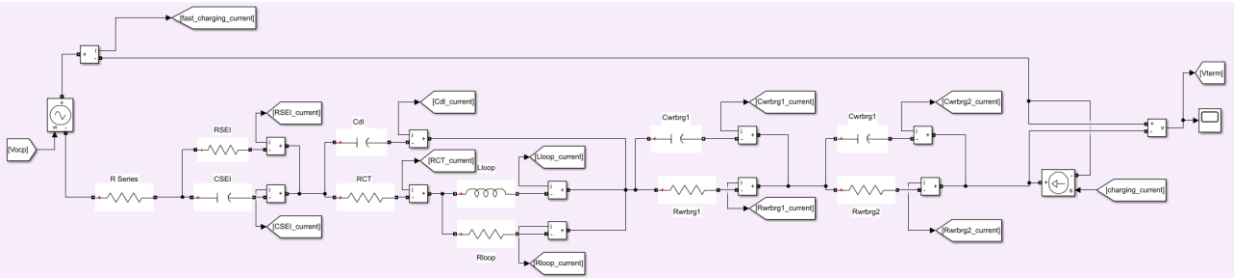

Figure 11: Simulink model of ECM between Li/Li+ and anode

These simulated charging data were then compared to the data found experimentally with the physical test cell. There are several key variables that must be examined including SOC, charging current and charging times. These comparisons are illustrated in Figure 12 and include charging current as a function of SOC, charging current as a function of time, and SOC as a function of time. The simulation data is shown as the blue scatter points where the experimental data is shown as the orange line, allowing for the data to be overlain without losing any information. It is also important to recall that in the introduction to this chapter, it is noted that

the proposed charging protocol will only charge cells to 80% SOC as opposed to 100% and that the maximum charging current will be limited to 3C.

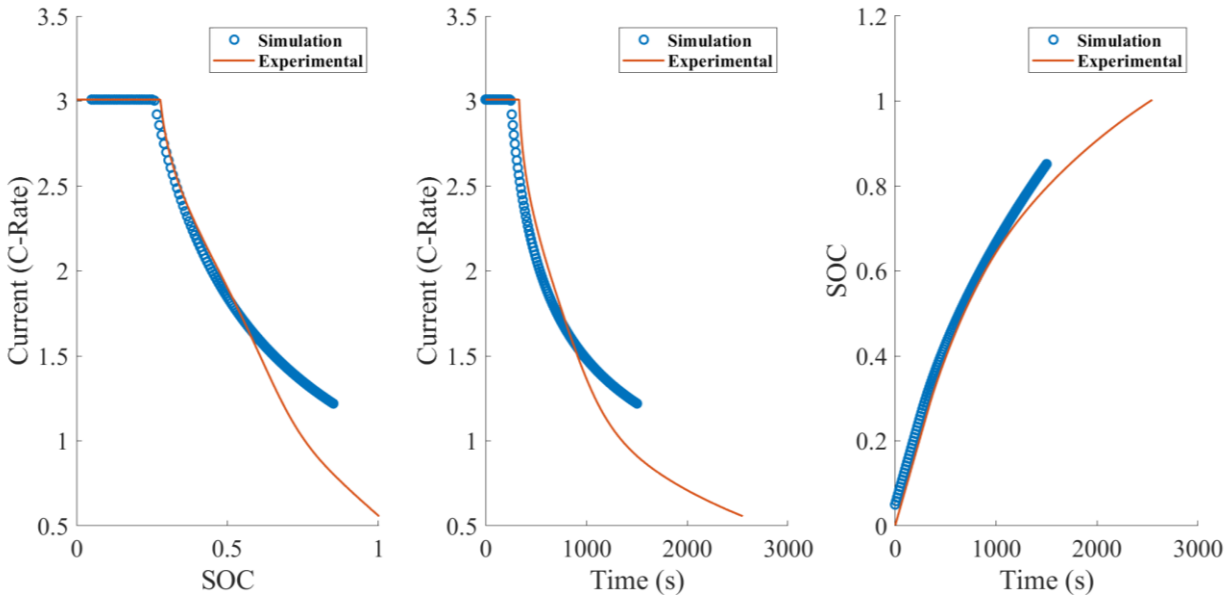

Figure 12: (a) Simulated and experimental charging current as a function of SOC, (b) simulated and experimental charging current as a function of time, and (c) simulated and experimental SOC as a function of time

The comparison of the experimental results illustrates that the simulation can accurately model the LIB and provide insight to the electrochemical processes that take place during charging.

Elimination of Inductive and Capacitive Elements

While the ECM simulation shows impressive results, it includes capacitive and inductive elements increasing the complexity of computations required to calculate the required charging current. It is advantageous to attempt to remove these items to decrease the computational power required without compromising the accuracy of the model. This conjecture is based on the time constants of the different capacitive and inductive elements within the model; they are much

shorter than the total charging time and the charging current charges very slowly with respect to those same time constants. To measure the contribution of the LC components within the model, the current through the specific elements was recorded and compared to the parallel R elements. As an example, the comparison of the current through C_{SEI} and R_{SEI} is illustrated in Figure 13.

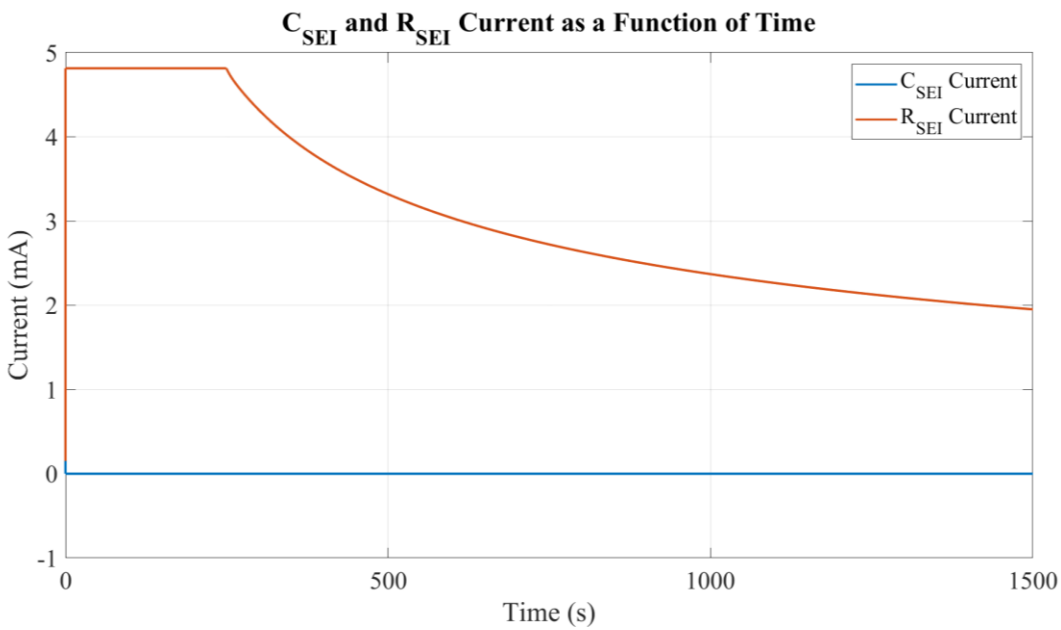

Figure 13: Comparison of C_{SEI} and R_{SEI} currents as a function of time during the charging process

The current through C_{SEI} is marginal compared to the current through R_{SEI} proving that C_{SEI} contributes little to the impedance during a DC charging process. This conclusion can be reached for all the other capacitive elements found in the system as the comparisons are extremely similar if not the same. Similar findings are reached for L_L and $R_{L,}$ but the inductor becomes a short-circuit removing R_L from the system. The remainder of the comparisons are included in Appendix A.

With these findings, the ECM can be condensed to include only the resistive elements, excluding R_L. This reduction decreases the computations required to find the charging current and greatly simplifies the systems. The impedance of the ECM is now considered purely resistive as illustrated in Figure 14. The values for the various resistances, as a function of SOC, were given previously in Table 1.

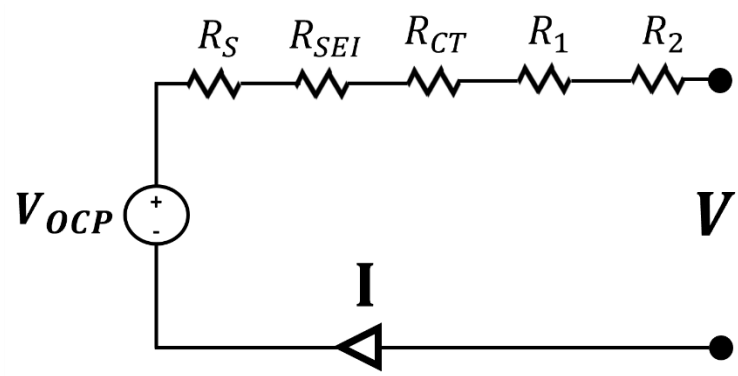

Figure 14: Purely resistive equivalent circuit model of Li/Li+ to anode

This simplified ECM was then compared to both the previous simulation, featuring the LC components, and the experimental data; this comparison is illustrated in Figure 15.

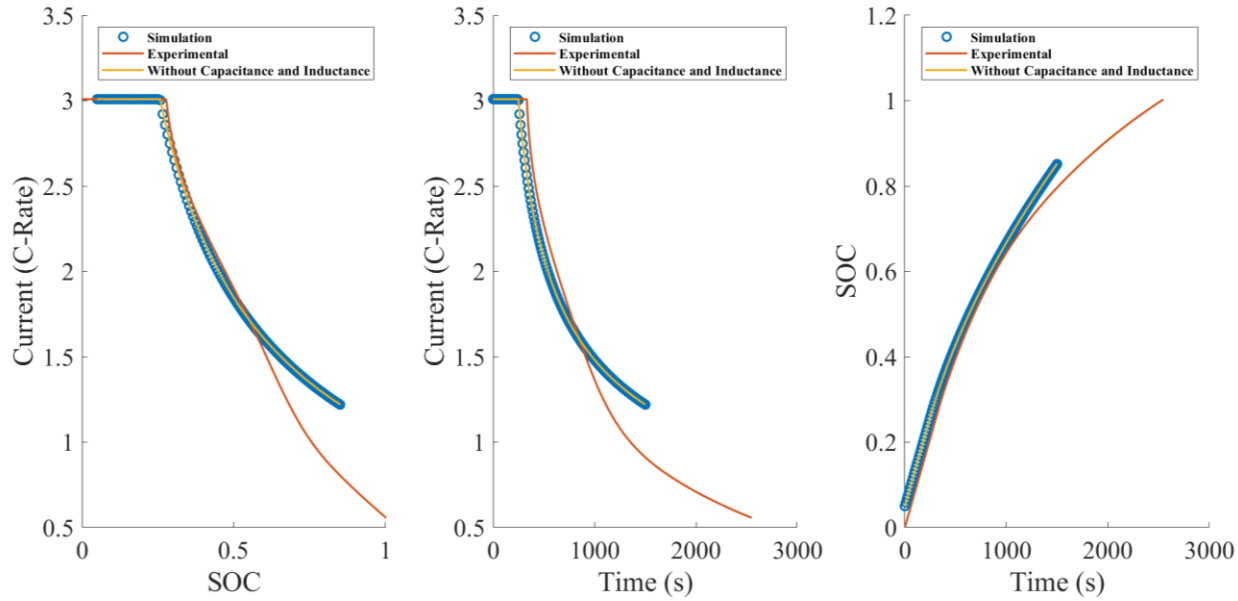

Figure 15: (a) Complete ECM, simplified ECM, and experimental charging current as a function of SOC, (b) complete ECM, simplified ECM, and experimental charging current as a function of time, and (c) complete ECM, simplified ECM, and experimental SOC as a function of time

This simplification of the system impedance during relatively constant charging currents clearly shows only marginal deviations from the more complex circuit model. It also illustrates a fast charging time requiring only 22.6 minutes to reach 80% SOC. The condensed model will now be solely used to determine the charging current for the protocol. The model based equation is given in (9).

$$I_{charging} = \frac{OCP(SOC) - 10mV}{\sum R(SOC)} \tag{9}$$

Combining (8) and (9), (10) can be formed.

$$I_{charging} = \frac{(943.29 * SOC^{-0.653}) - 10mV}{\sum R\,(SOC)} \tag{10}$$

While this equations allows for current to be calculated, the sum of the resistances is still a function of SOC. As the goal of this fast charging protocol is to eliminate lithium plating and remain easily implementable, it is advantageous to simplify the denominator of (10). To do so, the resistance values of the test cell were scaled, using the ratio of capacities, to the commercial 18650 LIB. As previously noted, the sum of these resistances at their respective SOCs will determine the charging current. The resistance sums are listed in Table 2 and graphed as a function of SOC in Figure 16.

Table 2: Summed cell resistances as a function of SOCs calculated for the anode of commercial 18650 LIB

SOC (%)	5	10	15	20	40	60	80	100
Sum of Resistances (mΩ)	42.321	26.778	25.674	21.881	21.372	20.470	22.299	22.433

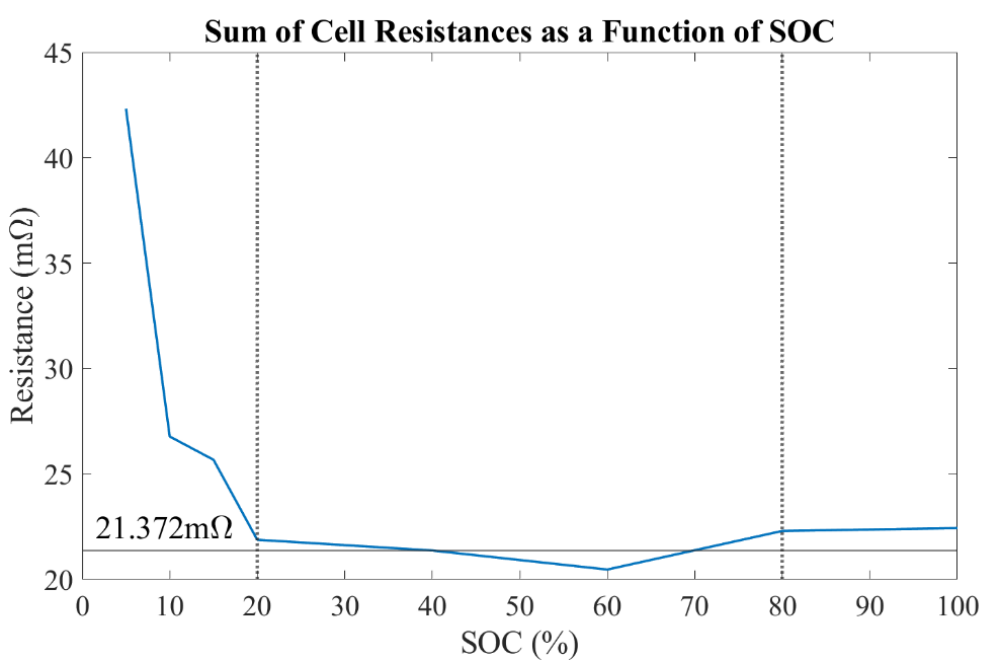

Figure 16: Sum of cell resistances as a function of SOC

As the goal was to remove the dependence on SOC from the denominator in (10), a singular resistance value is chosen. Here, the value representing 40% SOC is chosen to represent the SOC spectrum and will be utilized to realize the charging current for the commercial LIB. The choice of cell resistance seen at 40% is an accurate representation of the cell resistances seen from 20% to 80% SOC. Also, as the portion of the charging curve at low SOC is limited to 3C, this will have little effect. This results in (10) becoming (11).

$$I_{charging,simplified} = \frac{(943.29 * SOC^{-0.653}) - 10\ mV}{21.372\ m\Omega} \tag{11}$$

With this equation finalized for the commercial LIB, hardware and software design and testing could begin. The required charging current, based on SOC, is known, so hardware and software were developed to realize this charging protocol.

First, the power electronics for the charging systems were developed. The topology chosen was a synchronous Buck converter utilizing average current control. The calculations required for the elements will be described, this involves ensuring the proper output of the charging system as well as proper component ratings. Then, control theory used for the synchronous Buck converter will be explained and described. Using both the calculated component values and derived control system, the power electronics are then simulated to ensure proper operation. Finally, the implementation of the charger will be discussed, this involves a survey of the different integrated circuits (IC) and printed circuit board (PCB) design choices made. The software development is then described; this description includes a survey of the general process flowchart governing the charging and discharging process and complications navigated during implementation of the charging system.

DEVELOPMENT AND TESTING OF CUSTOM BATTERY CYCLING HARDWARE

The goals of developing a fast charging system are to independently cycle the battery under test and emulate realistic charging cases.

The created charging system will be able to implement the proposed charging protocol, discharge the cell under test, record the required data, and ensure safety throughout the process. This charger would have robust current control enabling the equation governing the charging current equation to be directly implemented. The charger also will have the ability to discharge the cell, utilizing constant resistance discharge, and continually record data to ensure cell health. The temperature of the cell will be monitored to ensure that temperatures allowing for thermal runaway are not reached. Temperature limits can be set such that the charger will be shut down if they are reached.

The realistic charging case typically requires that the battery be somehow mechanically connected and physically close to the charging electronics. This enables heat transfer between the charging electronics and battery under charge, an interaction not described or accounted for in any of the surveyed fast charging methods [10], [12], [32], [33]. Heating of the battery cell can encourage consumption of active materials and the possibility of thermal runaway, allowing the charger itself to contribute to the aging of the battery under test. This relationship should be studied as part of the research surrounding a fast charging protocol.

The battery utilized in this thesis will now be introduced. This cell was chosen as it features NMC cathode technology, the common choice of EV manufactures, and offers robustness to high charging currents. Then, the calculations required for the circuit elements used within the charging power electronics will be discussed. These elements are then simulated in

MATLAB and Simulink to verify proper operation. Integrated circuit (IC) elements were then chosen; those choices will be explained and examined. All required elements were then placed on a PCB and the required connections were created; the design choices related to the PCB will be examined. While a single charger design was utilized to conduct experiments, another was developed to illustrate improvements that could be made. Both chargers will be discussed and compared.

Introduction of VTC4

The cell utilized in this thesis is the US18650VTC4 (VTC4), a cylindrical 18650 cell featuring NMC cathode technology and graphitic anode technology [3]. The label 18650 indicates that the nominal diameter is 18.00 mm, and the nominal height is 65.00 mm. This LIB features a nominal voltage of 3.7 V and nominal capacity of 2100 mAh resulting in a power capacity of 7.77 Wh [3]. With a volume of 16.54 cm^3 and nominal mass of 45 g [3], the VTC4 attains a volumetric energy density of 469.7 Wh/L and a gravimetric energy density of 172.84 Wh/kg. The standard constant current charging rate for this cell is set at 2A, just under 1C, and a standard charge is listed at 2.5 h in length [3].

Synchronous Buck Converter Introduction and Examination

The Buck converter is a power electronics circuit utilized as a DC-DC converter and will be used to implement the proposed charging protocol. There are two main topologies, the first, the asynchronous Buck converter shown in Figure 17, utilizes a transistor (Q) and diode (D) to create an alternating voltage across an inductor (L) stemming from an input DC voltage. Due to the relationship between the voltage across an inductor and its resulting current, a sawtooth

current is generated by the inductor. As the goal of a Buck converter is to output a DC voltage, the sawtooth current created by the inductor is then smoothed by an output capacitor (C). This enables the DC portion of the created induced in the inductor to be send to the load, while the AC portion is filtered through the output capacitor. This output voltage is a stepped down version of the input voltage.

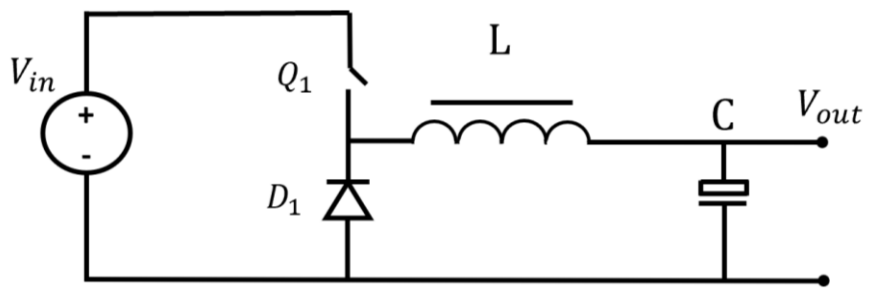

Figure 17: Asynchronous Buck converter topology

The synchronous Buck converter accomplishes the same goal as the asynchronous converter but utilizes two transistors to create the alternating voltage across the inductor as opposed to a transistor and diode. This similar topology is illustrated in Figure 18. The choice to utilize two transistors results in more efficient operation as transistors feature only an on-resistances and switching loss where diodes require a forward voltage of about 2 V.

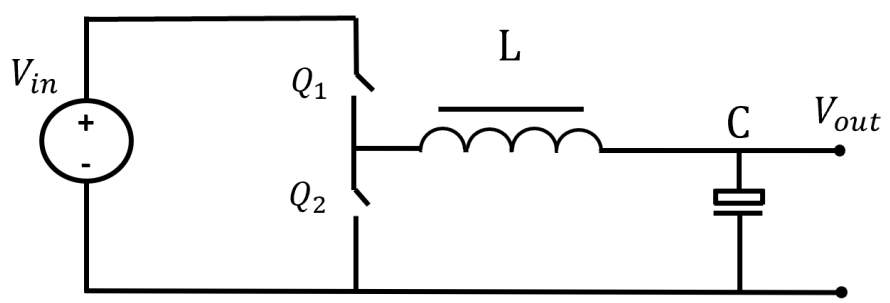

Figure 18: Synchronous Buck converter topology

While the Buck converter is more often utilized with voltage control, it can also be designed such that the output current is controlled. Ideally, as power is conserved during the DC-DC conversion process, the Buck converter can then act as a current step-up device. This topology and control choice is advantageous as the charging protocol requires that current be output as a function of SOC.

To construct the required electronics, the current and voltage levels utilized in the charging electronics were defined. This allowed for the component current and voltage capacities to be calculated such that they can withstand the power levels present. First, several important equations governing the required values will be derived through circuit analysis. Then, definitions and resulting component calculations will be outlined; this includes the voltage and current ratings for all components and component specific parameters such as capacitance and inductance.

Specifications and Calculated Elements

The specifications given for this power electronics circuit are given in Table 3.

Table 3: Converter specifications for Silicon based charging system

Specification	Value
$I_{out,max}$	10 A
ΔI_L	20% of $I_{out,max}$
V_{in}	12 V
V_{out}	2.5 V – 4.2 V
f_s	100 kHz

The goal of this design was to charge the VTC4 from 0% SOC to 80% SOC; therefore, the output voltages and currents of this system were determined by the parameters of the VTC4. The VTC4 operates over the ranges of 2.5 V to 4.2 V, specifying the output voltage range for the converter. It was also required that the charger be able to charge the VTC4 at currents of up to 5 C. Through experimentation, the practical capacity of the VTC4 was determined to be approximately 1.9 Ah. The maximum output current ($I_{out,max}$) was then chosen to be 10 A. The input voltage (V_{in}) was fixed at 12V, and the switching frequency (f_s) was set at 100 kHz. These are reasonable values for the required output voltage and power level. Finally, the inductor ripple current (ΔI_L) was chosen to 20% of the maximum output current. Again, this is a reasonable choice for a converter of this power level. The inductor ripple current rating will determine the inductance of the inductor and therefore the physical size. Choosing 20% of the output current as the ripple is often a good choice in having a small output ripple current while keeping the size of the inductor small.

With the specifications known, component values were then calculated. First, the Buck converter will be inspected, this will consist of a multiphase circuit analysis. Then, the required equations will be derived through circuit analysis; these equations will be used to find the required component values.

The Buck converter operates in two phases, these are dictated by the two transistors and their complementary switching. These switches apply an alternating positive and negative voltage across the inductor. Knowing that voltage and current in an inductor are related by (12), this alternating voltage induces a sawtooth current in the inductor.

$$V_L = L\frac{di}{dt} \tag{12}$$

Here, L is the inductance in Henries. This complimentary switching can be divided into two main states, with a focus on the on- and off-times of the upper transistor. The on-time of the upper transistor is defined as the duty ratio (D) times the switching period (Ts). The focus in this analysis will be on continuous conduction mode (CCM), meaning it is assumed that the inductor current is always greater than zero and there is some positive voltage at the output. When the upper switch is on, or closed, current flows from the source, through the inductor and to the output capacitor and load as illustrated in Figure 19.

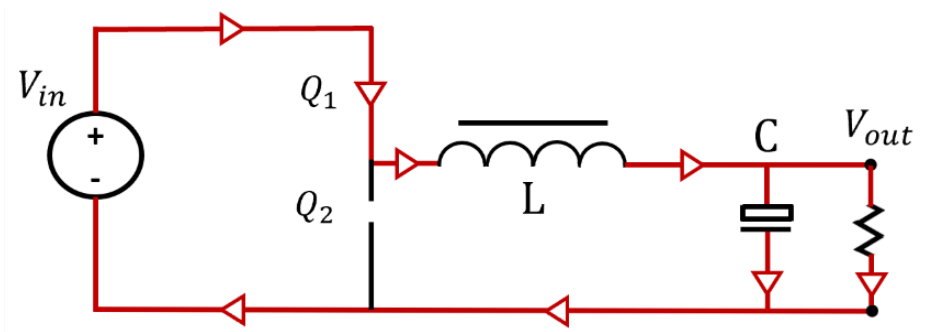

Figure 19: Analysis of T_{ON} for upper transistor in synchronous Buck converter

This forces the voltage across the inductor to be the difference between the input and output; as the input voltage is greater than the output voltage, the induced inductor current will have a positive slope. This is reflected in the current through the upper transistor. The positive slope portion of the current is then delivered to the output capacitor and load, where the AC portion of the current is filtered through the capacitor and the DC portion is delivered through the load. The circuit element specific curves are illustrated in the first column of Figure 21. This allows for energy to be stored in the inductor in preparation for the next state.

After the time requested for the on state has elapsed, the upper transistor will be turned off, and the lower transistor will be turned on; this time is referred to as the off-time. As the

current through an inductance cannot change instantly, the current will continue to flow to the load. Figure 20 illustrates the flow of current through the system during this stage.

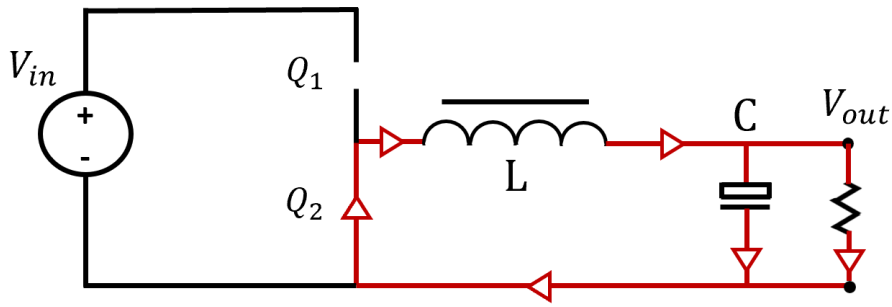

Figure 20: Analysis of T_{OFF} for upper transistor in synchronous Buck converter

The voltage across the inductor is now the negative of the output voltage, as one terminal has been shorted to the reference point in the circuit by the lower transistor. This negative voltage across the inductor will generate a current with a negative slope, as per (12). Again, this downslope of the sawtooth current will be delivered to the output capacitor and load. The AC potion will be filtered through the capacitor while the DC portion is delivered to the load.

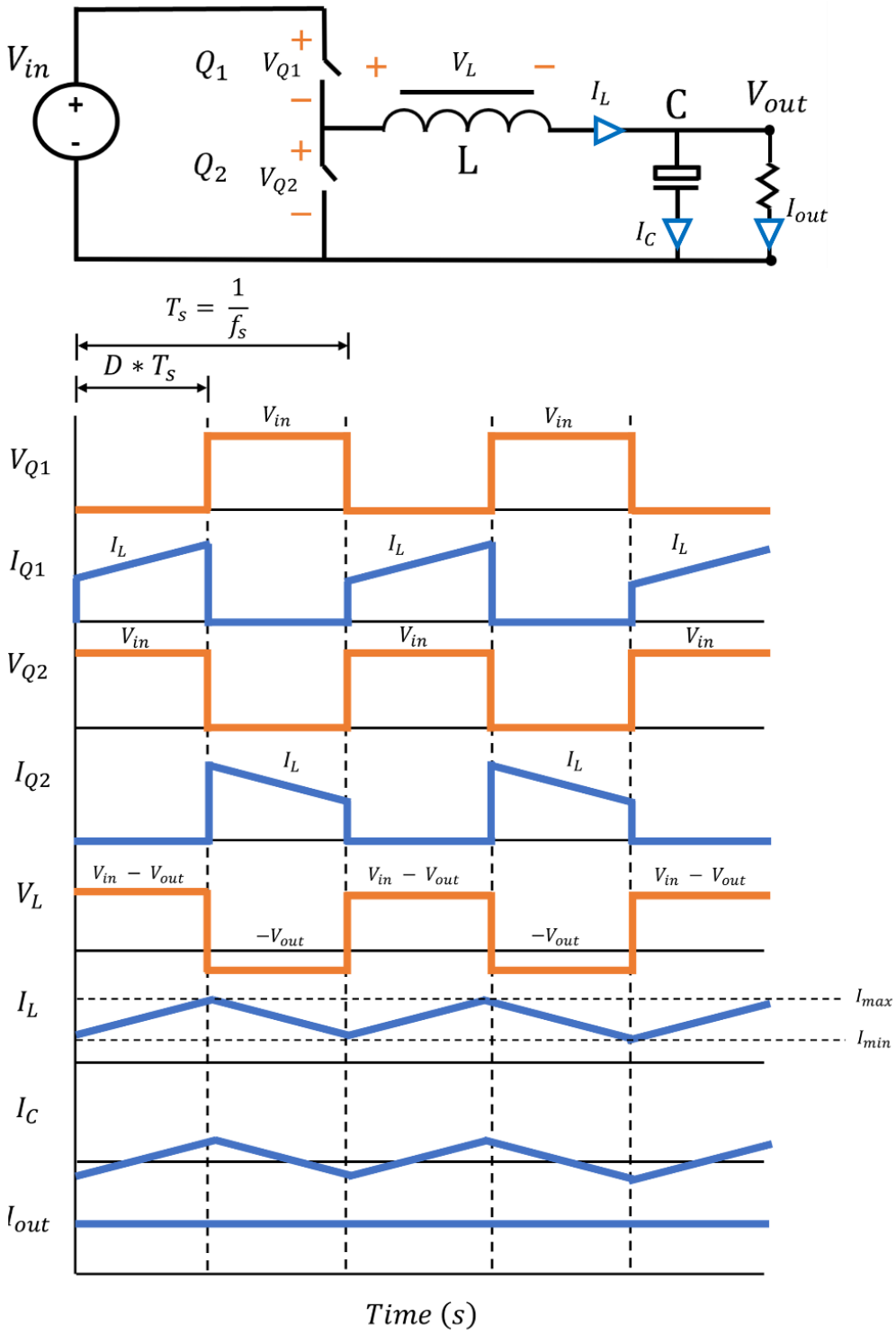

Figure 21: Analysis of current and voltages for specific circuit elements in the synchronous Buck converter

The circuit will continue to switch between these two states, allowing for a constant output current. Inspecting the inductor current, using its different stages and slopes, the output voltage can be found as (13).

$$V_{out} = DV_{in} \tag{13}$$

While output voltage control will not be needed to implement the proposed charging protocol, the calculation of the duty ratio will assist in finding several component values. To determine the parameters required for the circuit elements, circuit analysis can be performed. The required parameters for the inductor, transistors, and output capacitor can be found.

The sawtooth shape of the inductor current is segmented into two regions, stemming from the on- and off-states discussed above. These two sections can give insights into the required inductance and current ratings. Inspecting the positive and negative portions of the inductor current slope, we can determine the required inductance.

$$L = \frac{V_{in}(1 - D)D}{(\Delta I_L)(fs)} \tag{14}$$

The maximum current rating for the inductor can then be found.

$$I_{max} > I_{out,max} + \frac{\Delta I_L}{2} \tag{15}$$

The average current required of the inductor is given as $I_{out,max}$. The voltage rating of the inductor is not of concern in this low voltage system.

Next, the parameters for the two transistors can be determined, these include root-mean-square (RMS) current, peak current, and peak voltage. As the transistors will both conduct parts of the inductor current, the maximum required current for both is known and listed in (15). Then,

to determine the RMS current for both the transistors, the current waves presented in Figure 21 can be utilized. The required RMS current capacity for the upper switch can be found as (16).

$$I_{RMS,Q1} > \sqrt{D\frac{I_{max}^2 + (I_{max}I_{min}) + I_{min}^2}{3}} \tag{16}$$

Similarly, the RMS current requirement can be found for the lower transistor.

$$I_{RMS,Q2} > \sqrt{(1-D)\frac{I_{max}^2 + (I_{max}I_{min}) + I_{min}^2}{3}} \tag{17}$$

I_{max} and I_{min} have previously been defined by the inductor and given specifications. The peak current required by the switches is governed by I_{max} as given in determining the inductance. The voltage capacities required for both transistors can be determined by circuit analysis, giving a required peak voltage that is equal to the input voltage.

Finally, the required ratings for the output capacitor can be found. As the capacitor will filter the AC portion of the inductor current at the output, it must be able to withstand the RMS value of that current as well as the output voltage. The RMS current can be determined by knowing ΔI_L.

$$i_{C,RMS} = \frac{\Delta I_L}{2\sqrt{3}} \tag{18}$$

As all system specifications are known, all required circuit element parameters can now be calculated. As the output voltage of the system is determined by the VTC4, it will be chosen as 3.7 V, representing the voltage that the converter will output most often. This results in a duty ratio of 31%. Using (14)-(18), all required parameters can be found and are listed in Table 4.

Table 4: Calculated component values for synchronous Buck converter

Component	Calculated Requirements
Inductor (Inductance, Current Capacity)	12.8 µH, 10 A_{RMS}
Upper MOSFET (Current Capacity, Voltage Capacity)	5.48 A_{RMS}, 12 V
Lower MOSFET (Current Capacity, Voltage Capacity)	8.38 A_{RMS}, 12 V
Output Capacitor (Ripple Current Capacity, Voltage Capacity)	577 mA, 4.2 V

With the known parameters, circuit elements were selected to construct the required charging system.

With the discrete circuit elements required for the Buck converter selected, the required control was developed. As the proposed charging protocol requires that current be output as a function of SOC, average current control was chosen as the control mode. The control choices made will now be described.

Control Theory for Synchronous Buck Converter

To control the Buck converter in average current mode, closed loop control is implemented using the inductor current. The inductor current will be sensed and compared to a given reference; this error can vary widely, especially during startup of the converter. To handle this large error a compensator is employed, enabling the system to respond in a reasonable way. This compensated error is then compared to a sawtooth signal to generate gating signals for the

transistors. When the compensated error is greater than the sawtooth signal, the upper transistor is gated on, and lower transistor is gated off. When the sawtooth signal is greater than the compensated error, the upper transistor will be turned off and the lower transistor will be turned on. A diagram illustrating this control topology is illustrated in Figure 22.

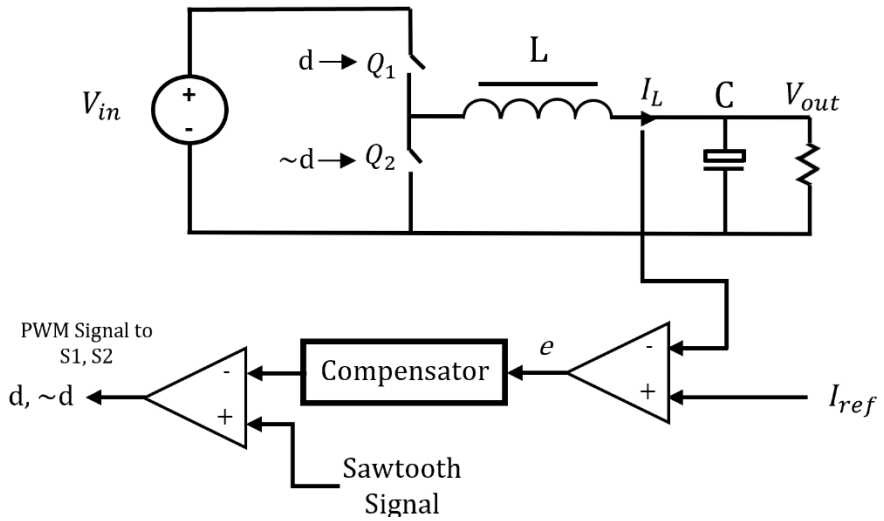

Figure 22: Average current control scheme for synchronous Buck converter

The compensator chosen for this system is the Type II compensator as illustrated in Figure 23. The Type II compensator gives one zeros and two poles, with one pole at DC.

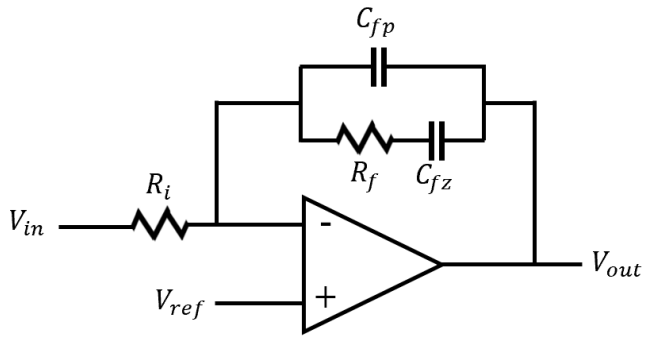

Figure 23: General Type II error amplifier

The transfer function of the Type II compensator is given in (19).

$$H(s) = \frac{-1}{R_i} \frac{sC_{fz}R_f + 1}{s^2 C_{fp} C_{fz} R_s + s(C_{fz} + C_{fp})} \tag{19}$$

As C_{fp} is known to be much smaller than C_{fz}, (19) can be rewritten as (20).

$$H(s) = \frac{-1}{R_i} \frac{sC_{fz}R_f + 1}{s^2 C_{fp} C_{fz} R_s + sC_{fz}} \tag{20}$$

With this simplified transfer function known, the pole and zero locations can be viewed using (21) and (22).

$$f_{z1} = \frac{1}{2\pi C_{fz} R_f} \tag{21}$$

$$f_{p2} = \frac{1}{2\pi C_{fp} R_f} \tag{22}$$

As per Reference [39], f_{z1} was placed at 10 kHz, 1/10th switching frequency. The purpose of this zero is to increase the phase margin of the system. Then, f_{p2} was placed at the switching frequency of 100 kHz; the purpose of this pole is to attenuate noise at frequencies greater than the switching frequency [39]. R_f and R_i were chosen to be 1 kΩ, these choices allowed for C_{fp} and C_{fz} to be calculated. All values are illustrated in Table 5.

Table 5: Calculated error amplifier component values for closed-loop average current control

Component	Value
R_f	1 kΩ
R_i	1 kΩ
C_{fp}	159 pF
C_{fz}	1.59 nF

The current sensing, comparator circuitry, and gating signal generation will be handled by specifically chosen ICs, so no calculations required for those elements.

With the elements required for the power electronics and feedback control circuitry calculated, the system can now be simulated. To do so, MATLAB and Simulink were utilized, which offers access to the circuit elements and the control modeling blocks required. The required outputs will be verified, as given in Table 3, using the calculated circuit element values.

Simulation of Power Electronics and Feedback Control

The goal of simulating the charging power electronics was to ensure stability during the charging process and to validate the calculated component values. The charging system was built using Simulink's Specialized Power Systems toolset and libraries, while the analog control circuitry was modeled using control blocks from several different Simulink base libraries. The focus of this simulation was the stability and operation of the system at 10 A (5C) output currents and a current reference modeling a descending current reference from 6 A to 2 A (3C to 1C). The 3C limit was selected as the maximum current that would be used to charge the commercial LIB.

The simulation was built using the calculated values from the previous sections. The system is illustrated below in Figure 24.

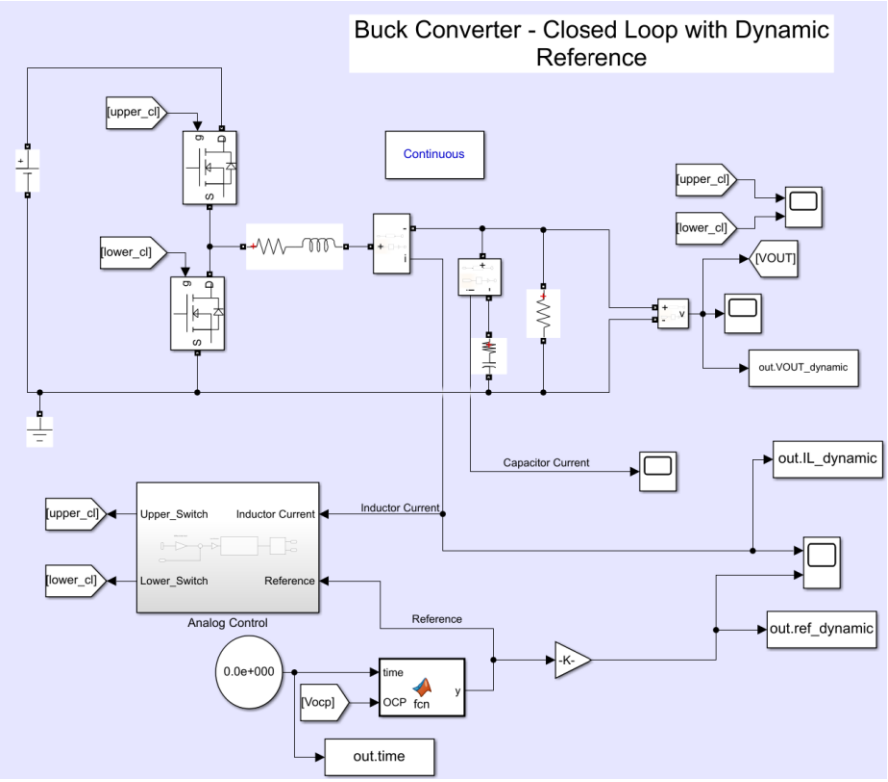

Figure 24: Simulink simulation of charging system control and power electronics

Realistic series resistances were included for the inductor and capacitor. Current sense and gain blocks were used to model a current sensing resistor and differential amplifier, which will act as the output sensing when the circuit is realized. Several control blocks were utilized to model the analog feedback networks and required comparators. A MATLAB function was used to model the microcontroller that would provide a variable reference. The system output at 10 A (5C) will now be inspected to verify proper operation. A 10 A reference was provided to the system. The inductor, output, and reference currents are illustrated below in Figure 25.

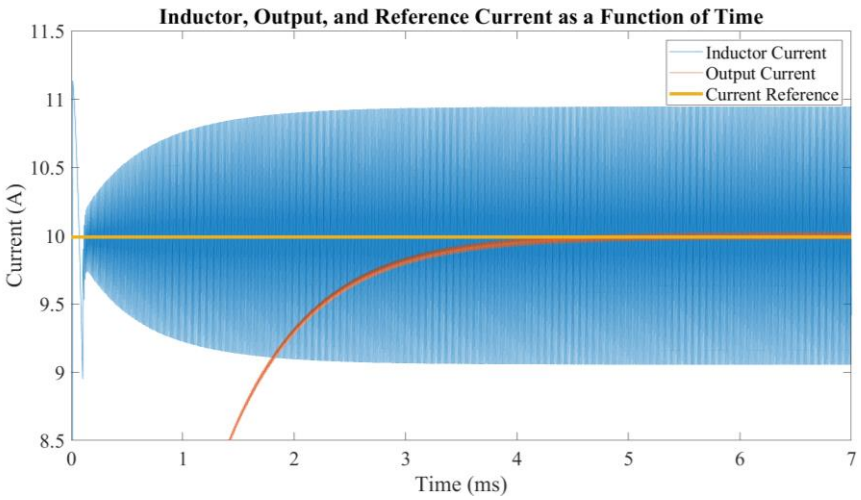

Figure 25: Inductor, output, and reference current as a function of time for simulated charging system

The inductor and output current respond to the current reference quickly and accurately, reaching steady state in approximately 5 milliseconds as illustrated in Figure 26. This verifies the stable operation of the charging system at 10 A.

Inspecting the inductor current at steady state shows that the ripple specification of 20% of the output current is met; this is specified in Table 3.

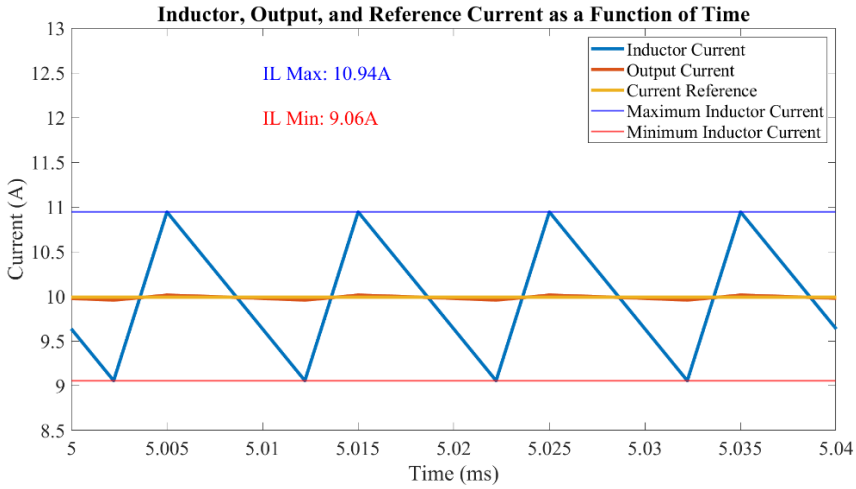

Figure 26: Inspection of inductor current as a function of time to ensure that ripple specification is met

Inspecting the maximum and minimum of the inductor current ripple at steady state shows that the system meets the required specifications. The maximum is found to be 10.94 A, which is less than the 11 A maximum allowed. The minimum is found to be 9.06 A, greater than the 9 A minimum allowed. These measurements validate the calculated inductance value. The control calculations are implicitly confirmed as the system is stable at the required output current. There is no need to quantify the results of testing the control calculations as the system can be stable at many combinations of the control parameters.

Next, the system was verified at the current levels that would be required for battery charging. This was done using scaled version of the charging currents generated by the earlier small cell simulations. The inductor current as a function of SOC is visualized in Figure 27.

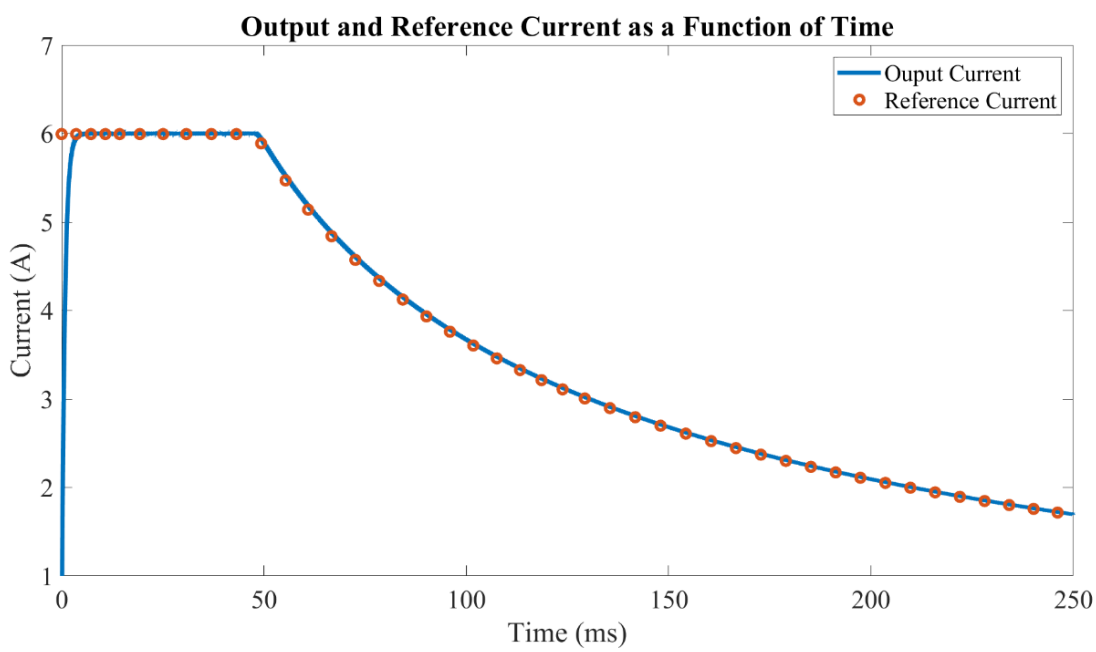

Figure 27: Output and reference current representing the proposed charging protocol as a function of time

This simulation validates the stability of the charging system at the current levels that are required by the proposed charging protocol. The charger can accept the function required by the charging protocol.

As the component values and stability of the charger have been verified, the charging system was then realized. This included choosing the required ICs required for the implementation of the charging power electronics and control as well as the calculation of SOC and data logging. These ICs were then placed on a PCB for organization and reliability. The PCB design choices will be explained. While one charger was utilized as the main system for experiments, an improved system was designed and tested. These two different versions will be compared.

Realizing Power Electronics for Battery Charging: Silicon Based Version

As all component values were determined during design and confirmed during simulation, the charging electronics could now be chosen. Transistors, capacitors, and the inductor were chosen based on the specification and calculated values. The list of these components is given in Appendix C.

Integrated circuits were then selected that would construct the system. This included the pulse width modulation (PWM) controller, transistor gate driver, differential current sense amplifier, microcontroller unit (MCU) for implementing the charging current equation, and Hall effect sensor for data logging. These choices will now be briefly described.

PWM controllers include the compensation network required for closed loop feedback to be implemented, the switching frequency determination circuit, and other system protections. The PWM controller chosen for this system was the UC3823 from Unitrode / Texas Instruments.

This controller offers switching up to 1 MHz, a 50 ns propagation delay, and a wide bandwidth error amplifier [40].

The UC3823 outputs a single gating signal, able to drive a single low-side transistor. To drive both transistors required for the synchronous Buck converter, a gate driver that accepts a single input and creates dual outputs was chosen. This gate driver is the IR2184 from Infineon Technologies. This driver can complimentarily drive the two transistors required for the synchronous Buck converter using a bootstrap circuit [41]. This driver also features a shutdown pin which will be utilized when battery cells are discharging.

To sense the induced voltage across the sensing resistor and relay it to the UC3823, a differential amplifier is utilized. This amplifier is the TLC081IP from Texas Instruments which offers a slew rate of 19 V/μs and a bandwidth of 10 MHz [42]. Using resistors, the gain of the TLC081IP was set to 15 times, and a sensing resistor of 20 mΩ was selected.

To generate the reference current based on the proposed charging current, log data, and manage the charging system, the MSP403FR2355 MCU was selected. This MCU features 16-bit architecture and a system clock capable of 24 MHz operation. This MCU also incorporates multiple I^2C modules, digital to analog converters (DAC), analog to digital converters (ADC), timer modules, and 32 KB of FRAM [43]. These modules allow for the MCU to read from other sensors in the system using both digital and analog means and output the charging current reference via the DAC.

To measure the charging current as output by the system, a Hall effect sensor was utilized. The Hall effect sensor selected was the ACS717KMATR-10B-T from Allegro Microsystems. This Hall effect sensor allowed for bidirectional current sensing, which is

required for the cycling system, with a sensitivity of 132 mV/A. The output of the Hall effect sensor is tied to the MCU allowing for the voltage output to read directly by the on-chip ADC.

Several other ICs were chosen to assist in system operation, including the LM92 digital temperature sensor to read case battery temperature [44], the TLV2217-33KCSE3 3.3 V regulator to create the voltage supply for the 3.3 V rail [45], and the MIC5014YN high side gate driver to allow for the battery to discharge [46]. Many passive elements were selected to aid these ICs in their operation. All ICs were given bypass and decoupling capacitors to assist in noise rejection and power supply dips.

As mentioned previously, a discharging circuit was also designed. This circuit allows for the battery to be fully cycled without removal from the charging system, enabling autonomous cycling by the system. This system was comprised of a constant load resistance and high-side transistor.

These elements were then placed on a PCB using the EagleCAD PCB design software from Autodesk. Symbols and footprints were created from the component datasheets, and the system was assembled first as a schematic and then laid out and routed on a PCB. The finalized board is illustrated below in Figure 28.

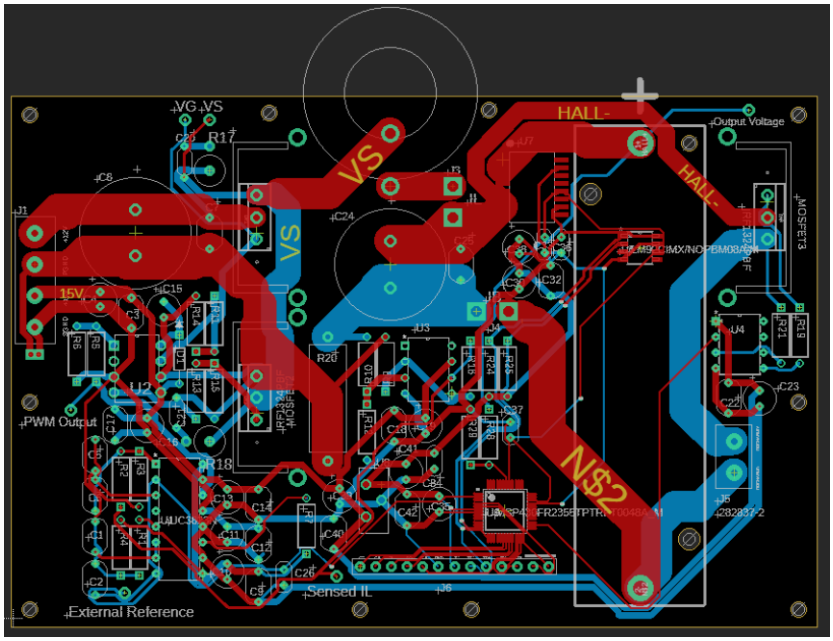

Figure 28: Finalized PCB layout in EagleCAD for Silicon based charging system

The unpopulated PCBs were ordered form OSHPARK, a US based board house known for their high quality products, and components were ordered from Digikey. Once both had been received, the system was assembled as illustrated in Figure 29 with several key parts identified.

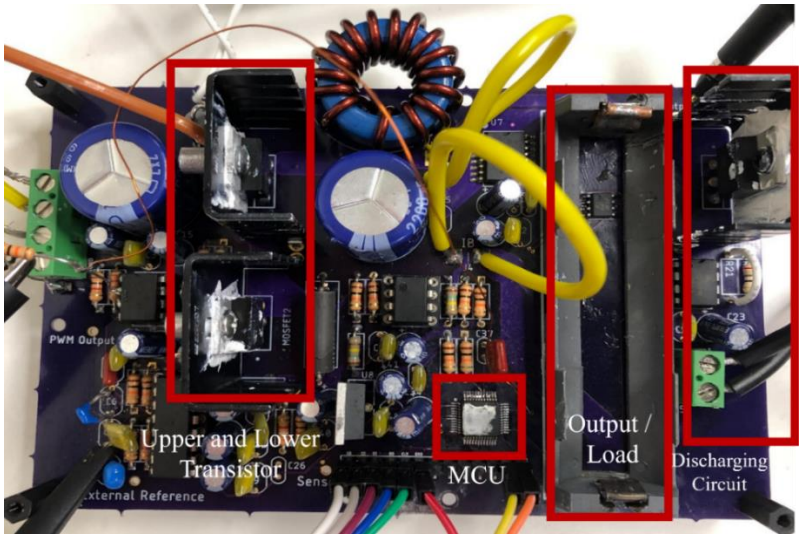

Figure 29: Assembled silicon based charging system

Several current measurement loops were included in the design. These enabled the inductor and output current to be measured.

With the charger assembled, temporary software was written to test the output range of the charging system. First, the current control was calibrated at constant output to ensure that the current requested by the microcontroller was properly output. Next, to ensure stability with an LIB as the load, a LIB was charged with constant current, this experimental set up is illustrated in Figure 30 and the results are shown in Figure 31.

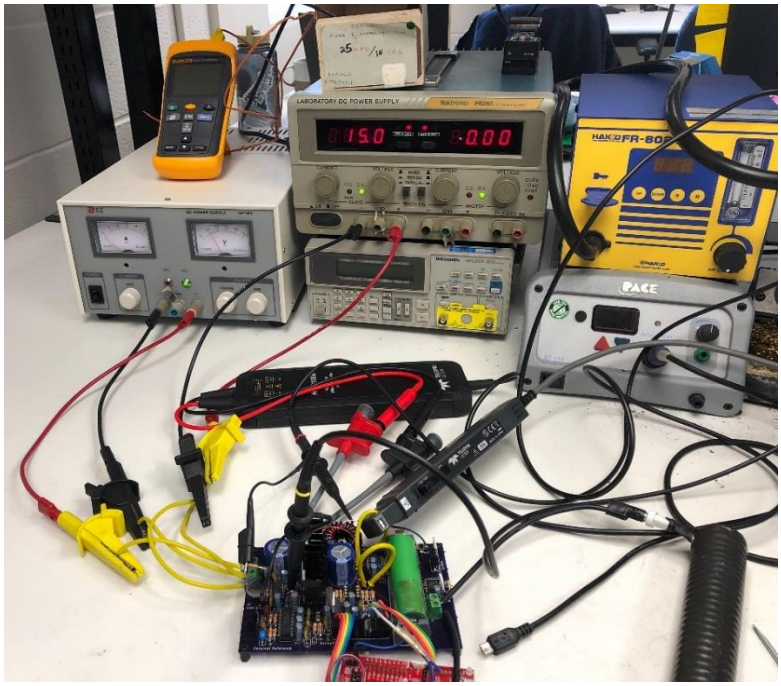

Figure 30: Confirmation of stability for GaN based charging system: constant current output and lithium ion battery as load

Figure 31: Oscilloscope screenshot illustrating from top to bottom: upper transistor gating signal, lower transistor gating signal, inductor current, output voltage for Silicon based charging system

Then, the charging algorithm was incorporated into the test software, but the output was selected to be a resistive load to mitigate any initial failures. Data were formatted, written to an SD card using the SPI interface, and finally imported into MATLAB for visualization. This output current is illustrated in Figure 32.

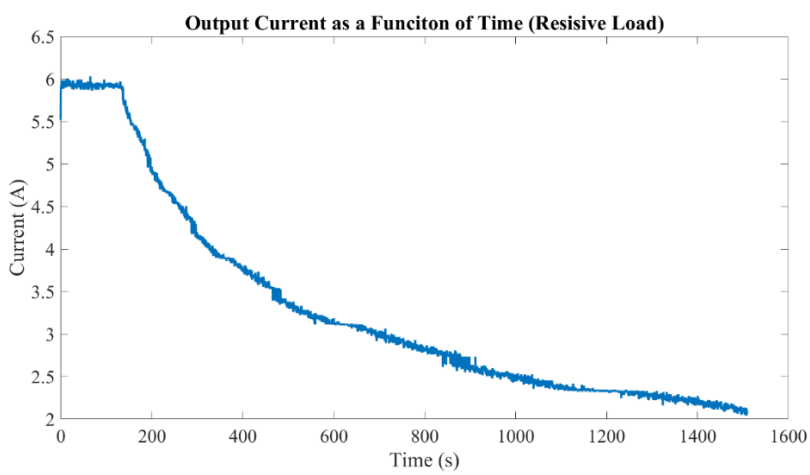

Figure 32: Silicon based charging system output current as a function of time for a resistive load

These data reveal several key facts. First, the charging system is working as intended; it can sense the output current, calculate representative SOC, and output a variable current via the given equation. Second, the charging time seen for this test is extremely similar to the one seen in the simulation of the small cell. Recall that this protocol will charge from 0% SOC to 80% SOC. The charging times are nearly identical, as illustrated in Figure 12, requiring around 1500 seconds. The accuracy of the charging is verified in the coming sections, but the current focus is on practical operation.

The stability of the charging system over several cycles was investigated. This system is responsible for both charging and discharging commercial LIBs and must be able to complete many consecutive cycles. Again, test software was constructed that allowed charges and discharges to take place. This test software was eventually incorporated into the software used to conduct experiments, but this was a simpler set of instructions and logging techniques. The load would was an LIB. First, the cell was discharged to 2.7 V; this voltage was set as the indication of 0% SOC. Once this voltage was reached, the cell was then charged to 80% SOC using the proposed charging algorithm. Recall, the method of SOC calculation chosen for this system is enhanced Coulomb counting. Here, Coulomb counting is used to calculate SOC from 0% to 80%, and the voltage of the cell is used to determine when the cell has reached 0% SOC. This process was repeated to create a test system that could autonomously cycle the commercial LIB. The charging current and the absolute value of the discharging current as illustrated in Figure 33.

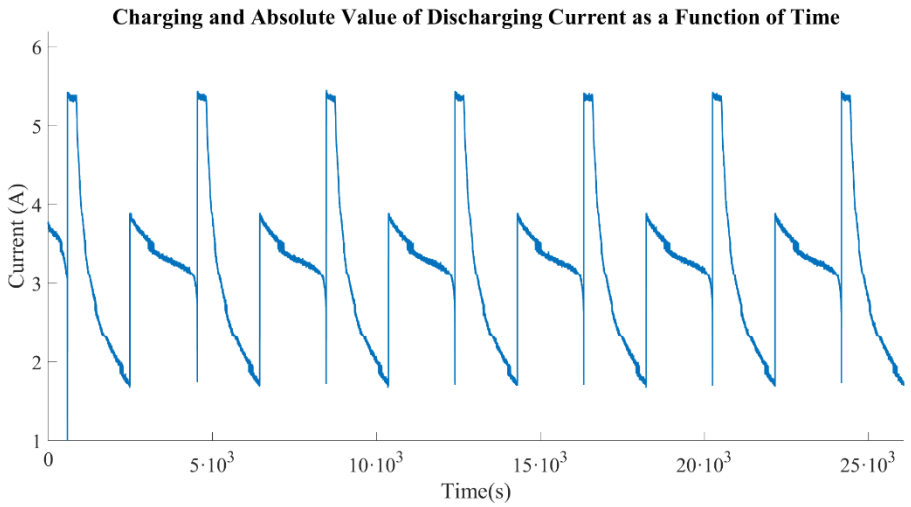

Figure 33: Charging and absolute value of discharging current as a function of time for silicon based charging system

This verified the charging systems ability to also act as a cycling system and a data logging system, having the ability to continuously charge and discharge the commercial LIBs while accurately logging the data.

With the capabilities of the system verified, the charging current was analyzed to ensure accuracy. This was done by logging the digital number calculated by the charging protocol and comparing to the output charging current. The reference current is set to zero during the discharging phase. The reference current, output current, and percent error are visualized in Figure 34. Note that several adjustments were made to the test software, so the constant current portion of the charging protocol is longer when compared to previous. This reflects the charging process more accurately, so slight deviations are seen from Figure 12.

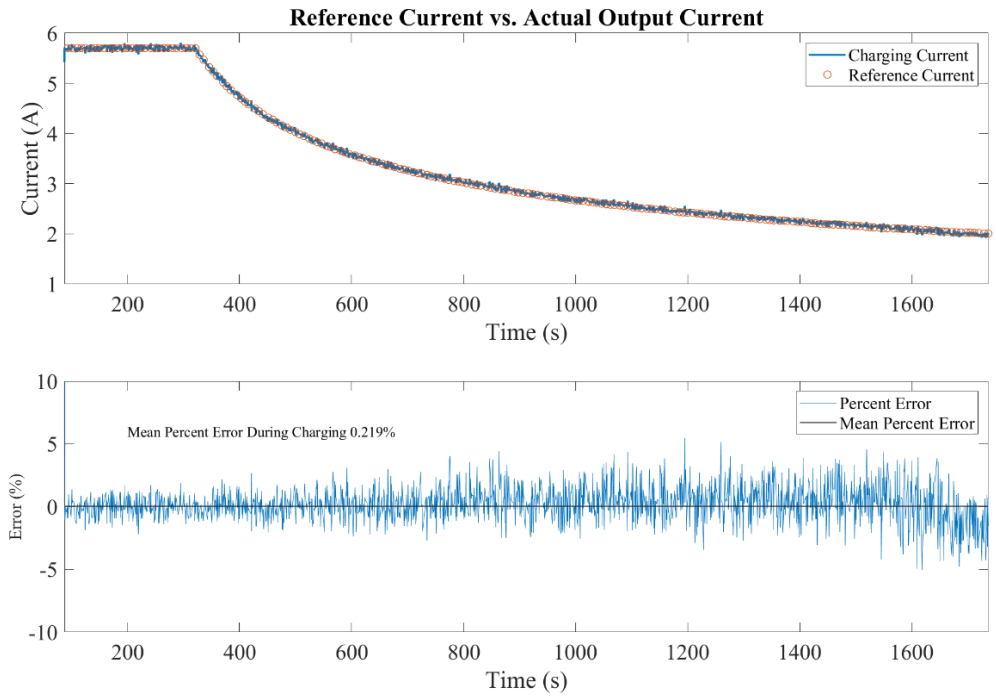

Figure 34: (top) Reference current compared to actual output current as a function of time and (bottom) percent error as a function of time for Silicon based charging system

The absolute maximum percent error seen is 5.49%, while the mean is 0.219%. The high maximum is indicative of noise in the system, but an impressive mean error illustrates that the system can accurately output the requested current. The current measurement also implicitly confirms the ability of the system to accurately measure discharging current. The charging time seen here is 28 minutes and 56 seconds; this is slightly longer than was seen in simulation. The difference in time has to do with non-idealities in the current sensing and logging.

The charging system can utilize the proposed charging protocol to generate a charging current, accurately output the calculated current, log the required data, and autonomously cycle a commercial LIB. This system is now able to begin long term cycling tests to evaluate the long term impacts of the proposed charging protocol.

While the long term cycling experiments were conducted with the previously described charging system, using the lessons learned, a new charging system was developed. The goal of developing a new charging system was to improve on the previous design in several ways. First, the switching frequency aim was increased to 1 MHz, with the goal of decreasing the inductor ripple current. This would allow the charging system to attain lower output current currents; therefore, allowing the system to charge to a higher SOC. Second, there was to be a focus on gallium nitride (GaN) technology. The GaN technology would be utilized in the transistors and provides several benefits over traditional silicon (Si) technology. Another aim for this improved charger was to create a more commercially applicable project meaning that more surface mount technology would be utilized as opposed to through hole devices. The design choices and outputs of this second charging system will now be examined. This new version was not used in LIB long temp LIB cycling experiments.

Realizing Power Electronics for Battery Charging: Gallium Nitride Based Version

GaN based transistors (GaN FET) offer several advantages over tradition Si based transistors (MOSFET). First, GaN FETs can be delivered in much smaller packages when compared to the traditional Si MOSFET while having comparable power ratings. The GaN FET chosen for the new charging system is the EPC2015C, offering a maximum drain-source voltage of 40 V and a maximum drain current of 53 A [47]. The Si MOSFET used in the first charging system, the IRFB7446PbF, features a maximum drain current of 120 A and maximum drain source voltage of 40 V [48]. The utilized Si MOSFET does have a greater power capacity than the GaN FET, but these are only individual products. Efficient Power Conversion (EPC) offers GaN FETs with up a maximum drain source voltage of 100 V and maximum drain current of 101

A in comparable packages sizes to the EPC2015C [49], rivaling the IRFB7446PbF. Regardless, in this application both the Si MOSFET and GaN FET exceed the required power requirements. In comparing the size of the IRFB7446PbF and the EPC2015C transistors, it is clear the advantages offered by the die GaN devices.

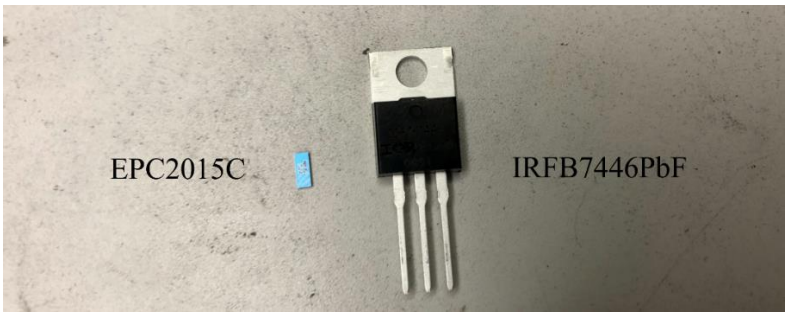

Figure 35: Size comparison of EPC2015C and IRFB7446PbF transistors

As GaN FETs can be offered in the illustrated die package, having similar power capacities to much larger Si MOSFETs, they have a key advantage. The EPC2015C also offers an on resistance of 4 mΩ [47] which comparable to the IRFB7446PbF which offers a typical on resistance of 2.6 mΩ [48]. When evaluated as a tool for efficient DC-DC conversion, GaN technology is also shown to outperform Si technology. For example, when evaluated as a transistor for a 48 V to 12 V, 120 W Buck converter operating at 1 MHz, GaN FETs were shown to have half the power loss of Si MOSFETs and an area-on resistance product of 4 times less [50].

In developing the new, GaN based charger, the same design process required for the Si based charger was followed. The output voltage and current remained the same, but the switching frequency was greatly increased. This motivated the reuse and replacement of certain ICs.

Table 6: Converter specifications for GaN charging system

Specification	Value
$I_{out,max}$	10 A
ΔI_L	20% of $I_{out,max}$
V_{in}	12 V
V_{out}	2.5 V – 4.2 V
f_s	1 MHz

The UC3823 PWM controller was used as this device offers a practical switching frequency of up to 1 MHz [40]. To determine this frequency, timing resistors and capacitors were used. As these values are imprecise, a switching frequency of 978 kHz was attained. As the limit of the UC3823 is being reached, thermal considerations will be made to enable the controller to operate at this frequency.

GaN FETs require a gating volage this is less than a typical Si MOSFET [47]–[49], so a new gate driving IC must be selected. The gate driver selected was the MAX8552ETB+ from Analog Devices Incorporated / Maxim Integrated. This device offers a switching frequency of up to 2 MHz, and a supply voltage of 5V which is recommended for the EPC2015C [47], [51]. It also enables a single input PWM signal to drive two output gating signals, which is required for the synchronous Buck converter [51].

To enable current sensing and closed loop control for average current mode control, a new current sense amplifier was also selected. The previously selected amplifier did not have a sufficiently fast slew rate for 1 MHz operation. The TLV3541IDR operational amplifier from Texas Instruments was selected. This amplifier offer a slew rate of 150 V/μs, a vast improvement

on the 19 V/μs offered by the TLC081IP [42], [52]. The differential gain and sensing resistor values remained the same.

The increase in frequency and increase in complexity did not affect the choice of microprocessor which remained the MSP403FR2355, but several considerations were made. With the increase in frequency, faster rise times were present in the system. This creates more noise, specifically on the reference line. Therefore, the MCU was given its own 3.3 V regulator and a decoupling capacitor was placed as close to the MCU as possible.

While the increase in frequency would have had no effect on the choice of the Hall effect sensor, as the measured value is the DC output current, global stock of the original choice was depleted. This required the choice of a new Hall effect sensor. The TMCS1108A2 from Texas Instruments was selected. This sensor offers a sensitivity of 100 mV/A and outputs an analog voltage proportional to the sensed current [53].

All other devices remained the same. To create a 5 V supply for the transistor gate driver, the LT1085CT-5#PBF-ND from Texas Instruments was used [54].

With all components selected, the new GaN charging system was constructed in the EagleCAD PCB design software. First, the new components were created; this included their symbols and footprints. Then, the schematic was created using the existing components. Finally, the footprints were laid out on a PCB and the required traces were routed. The finalized board is illustrated in Figure 36. Note there is an air-wire present near the bottom of the figure. This was an intentional choice in creating independent 3.3 V rails for the MCU and Hall effect sensor.

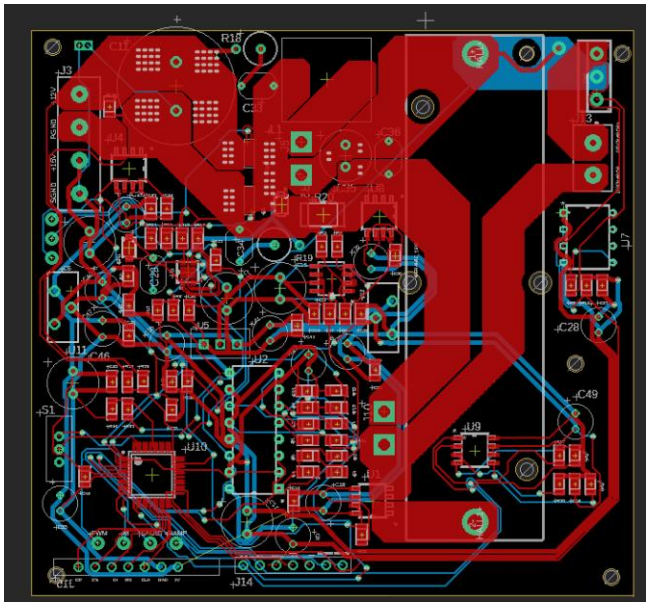

Figure 36: Finalized PCB layout in EagleCAD for GaN based charging system

The PCB was ordered from OSHPARK and the additional required parts were ordered from Digikey. Once the PCB and parts were received, the GaN charging system was assembled. The assembled system is illustrated in Figure 37.

Figure 37: Assembled GaN based charging system

Heat sinks were placed on the PWM controller to enable continual operation at 978 kHz. The heat sinks are clearly present in the bottom half of the previous figure.

Just as with the previous Si based charging system, the test software was used to confirm the operation of this charger. The same testing procedure was followed for the GaN based charging system. First, a resistive load was used to verify the proper operation of the power electronics. Then, a LIB was charged with a constant current. Figure 38 illustrates this test set up and Figure 39 resulting oscilloscope measurements.

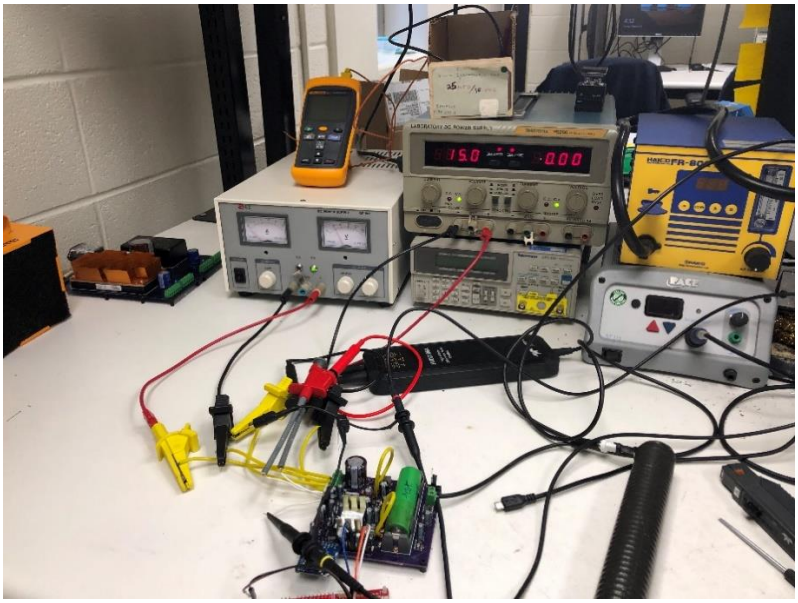

Figure 38: Confirmation of stability for GaN based charging system: constant current output and lithium ion battery as load

Figure 39: Oscilloscope screenshot illustrating from top to bottom: upper transistor gating signal, lower transistor gating signal, inductor current, output voltage for the GaN based charging system

Once the power electronics were verified, the charging and discharging process was tested. The accuracy of the charging current is illustrated in Figure 40.

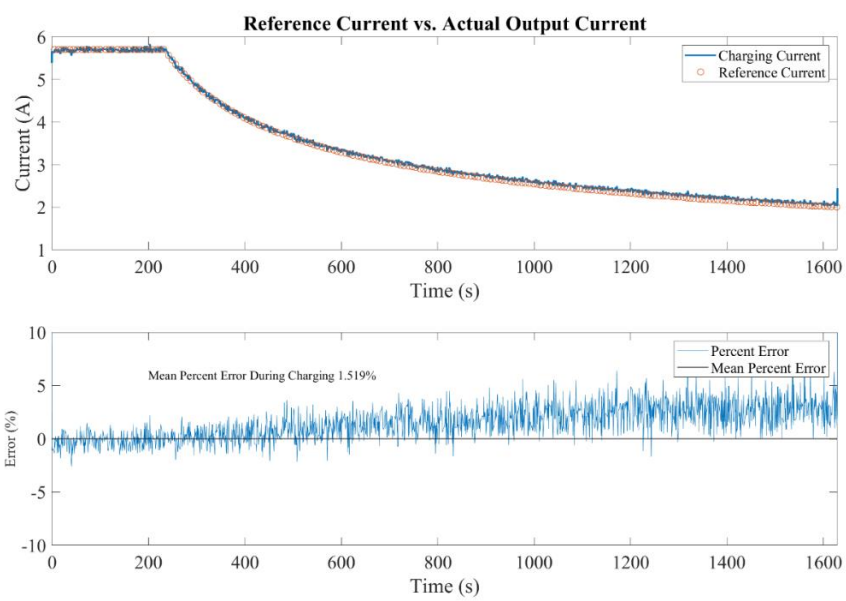

Figure 40: (top) Reference current compared to actual output current as a function of time and (bottom) percent error as a function of time for GaN based charging system

The mean percent error displayed by the GaN based charging system is greater than the Si based charger and it shows a greater percent error at lower output currents. The maximum absolute error is 7.93%. There are many probable sources for the error seen at lower output currents. First, at lower currents, the voltage sensed across the sensing resistor by the current sense amplifier is smaller; therefore, the signal to noise ratio is lower which enables the noise to have a greater impact on the system. A similar issue affects the reference voltage provided by the microcontroller and the analog signals being output to the MCU from the Hall effect sensors. As the reference becomes smaller in magnitude, it can be more easily affected by noise in the system.

While the Si charging system was used to conduct cycling experiments and the GaN based system was not, a comparison between the two can provide several insights into system design with more traditional technologies and emerging ones. The two boards will now be directly compared in terms of size, cost, and efficiency.

Comparison of Inductor Ripple Current and Efficiencies

The purpose of designing the GaN based charging system was to allow for a smaller output current. The smaller output current allows for the charging protocol to charge cells to higher SOCs before the inductor current becomes negative. Utilizing (14), the inductor ripple current is proportional to the switching frequency. Therefore, by increasing the frequency by ten times, from 100 kHz to 1 MHz, the inductor ripple current is expected to decrease by ten times.

First, the ripple current for the Si charging system will be inspected. To do so, the realistic values were measured from the charging system to reflect component values more accurately. The charging current was set to 3C and an approximate 1 Ω load was selected. The

output voltage, switching frequency, and input voltage were recorded. Using an inductance-capacitance-resistance (LCR) meter, the practical inductance of the inductor was measured. All these data were recorded in Table 7.

Table 7: Measured quantities for Silicon based charging system

Quantity to be Measured	Measured Value
Inductance	15.4 µH
Output Voltage	6.311 V
Switching Frequency	102.1 kHz
Input Voltage	12.04 V

Using the values required in Table 7 and slightly rearranging (14), the inductor ripple current can be calculated and then compared to the actual value. The actual inductor current, pictured with the output voltage, is illustrated below in Figure 41.

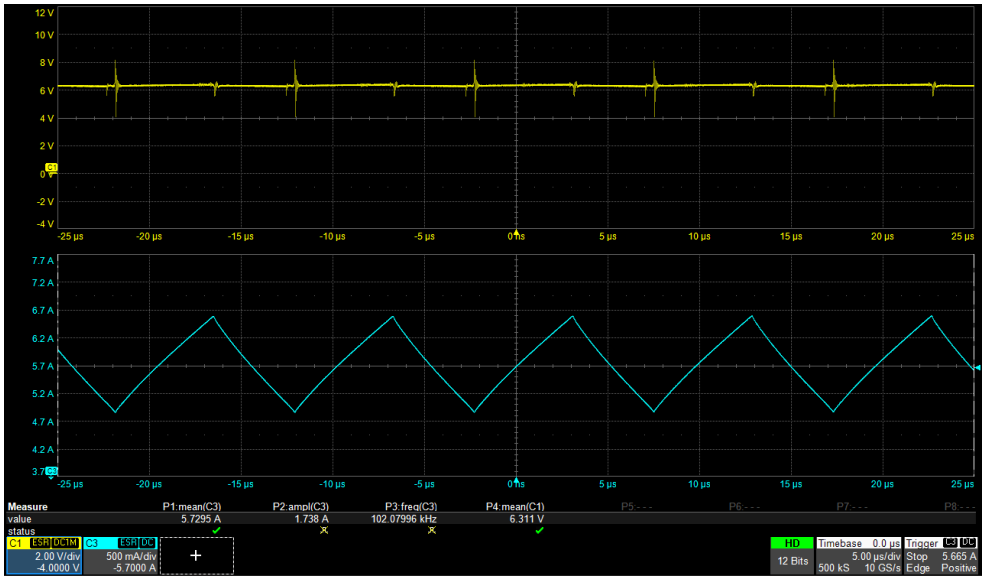

Figure 41: Oscilloscope screenshot illustrating from top to bottom: output voltage and inductor ripple current for the Silicon based charging system

Using (14) and the data in Table 7, the theoretical inductor current is found to be 1.90 A. The ripple current was measured to be 1.738 A. This results in a percent error of 8.53%. The error stems from assuming ideal circuit elements when forming (14). Realistic circuit elements will feature series resistances and other losses. This forces (14) to be an estimation rather than a precise prediction.

Similarly, the GaN based charging system was inspected. The same load and supply conditions were used. The resulting data was recorded in Table 8.

Table 8: Measured quantities for GaN based charging system

Quantity to be Measured	Measured Value
Inductance	14.0 μH
Output Voltage	6.297 V
Switching Frequency	978 kHz
Input Voltage	12.04 V

The expected inductor current was then calculated to be 218.6 mA. The measured inductor current ripple was found to 308 mA as illustrated in Figure 42. Note that the x and y-axes remained the same between Figure 41 and 42 to illustrate the difference in switching frequency and inductor current ripple.

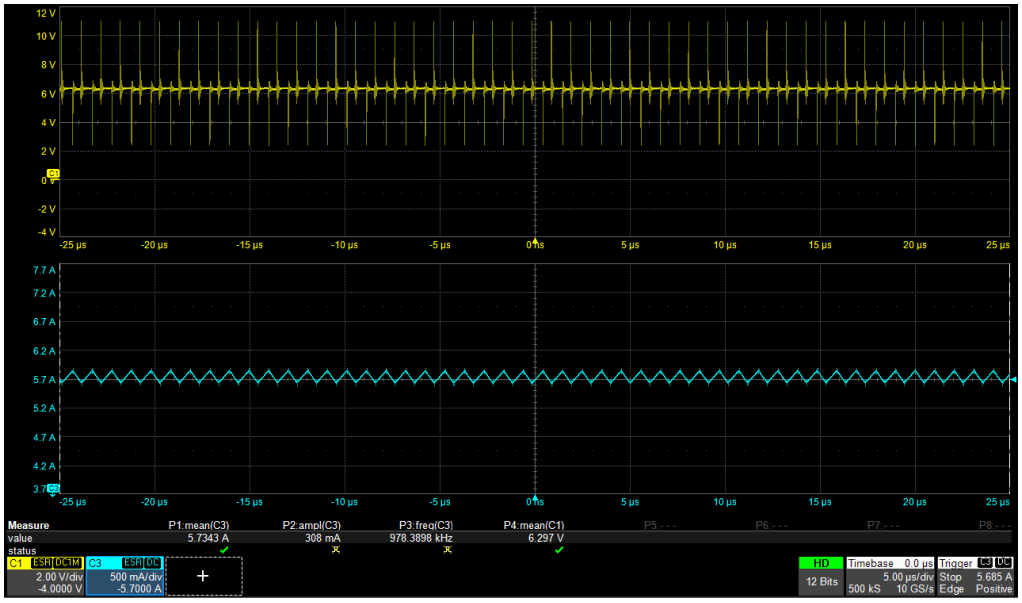

Figure 42: Oscilloscope screenshot illustrating from top to bottom: output voltage and inductor ripple current for the GaN based charging system

The percent error in the inductor ripple current was 40.9%. This higher error is due to the assumed ideal circuit elements which have an oversized effect on a much smaller ripple current.

To enable a future charging system to achieve charges requiring a higher SOC, the switching frequency was increased to lower the inductor current ripple. While a 9.57 times increase in frequency led to a 5.6 times decrease in inductor ripple current, the goal of lowering the inductor ripple current was achieved. The increase in frequency could allow for the charging system to output charging currents as low as 154 mA before the inductor current becomes negative.

Next, the power and energy efficiencies of the Si and GaN based systems were compared. The power efficiencies, for both charging systems, as a function of time are compared in Figure 43.

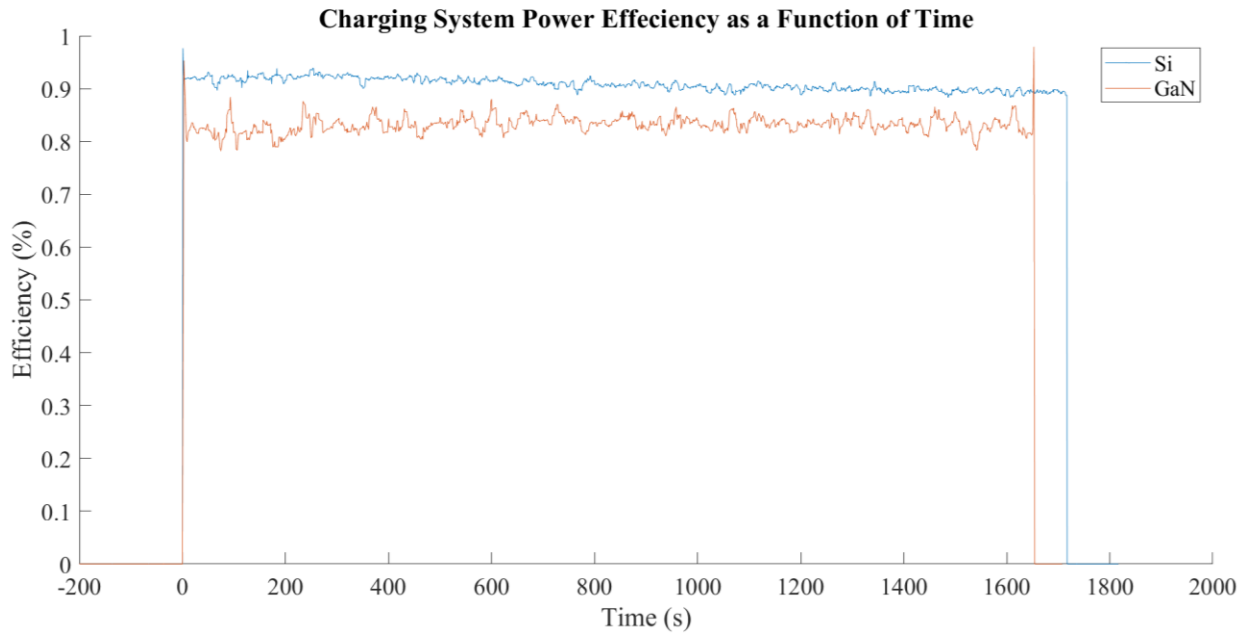

Figure 43: Comparison of charging system power efficiency as a function of time

Interestingly, efficiency does not have a strong dependence on the output power of the system. Note that the charging times are slightly different; this is seen constantly between cycles on the same charger as well and is due to sensing and noise error. The GaN system is not as efficient as the Si system due to higher switching loss resulting from the greater switching frequency. This is also reflected in the energy efficiency of the charging systems. The GaN system shows an energy efficiency of 83.1% during a fast charge, while the Si system shows an efficiency of 91.4%. This inefficiency is clear in a comparison of the temperature data recorded by the systems as the lost energy is converted to heat. The temperatures during the same charging illustrated in Figure 43 are shown in Figure 44.

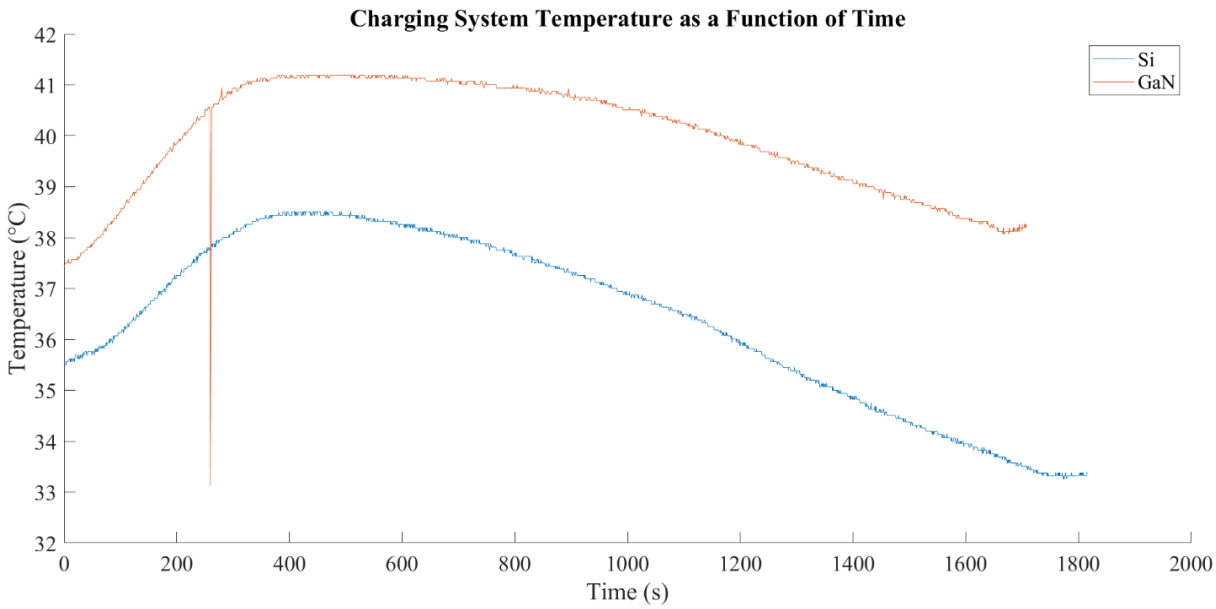

Figure 44: Comparison of charging system temperature as a function of times

Both charging systems illustrated a similar temperature rise and fall, but the GaN charging system will reach an upper temperature of nearly 42°C while the Si charging system will only reach 38.5°C.

To allow the charging system to attain lower output currents, the switching frequency was increased. This also resulted in several consequences. First, the higher frequency GaN based charging system was less efficient than the Si based charging system. The decrease in efficiency most likely stems from increasing switching losses at higher frequencies. Second, the inefficiency seen in the GaN based charging system led to higher temperatures during the charging process. While this increase in temperature was small, it will still affect the LIB health over many charges. The GaN based charging system offers an alternative to the Si based system. It can attain lower output currents at the cost of efficiency. The Si based charging system was used to conduct the following experiments.

DEVELOPMENT OF CUSTOM BATTERY CYCLING SOFTWARE

With the Si based charging hardware accuracy and stability verified, software to implement the required charging protocol was created. Implementing the charging protocol included the application of the derived charging equation, sensing the required system parameters, ensuring safety through the cycling process, and autonomously switching between charging and discharging states.

The digital and sensing system consists of the MSP430FR2355 microcontroller, the ACS717KMATR-10B-T Hall effect sensor, the LM92 temperature sensor, and the required programming inputs and test points. This system is illustrated in Figure 45.

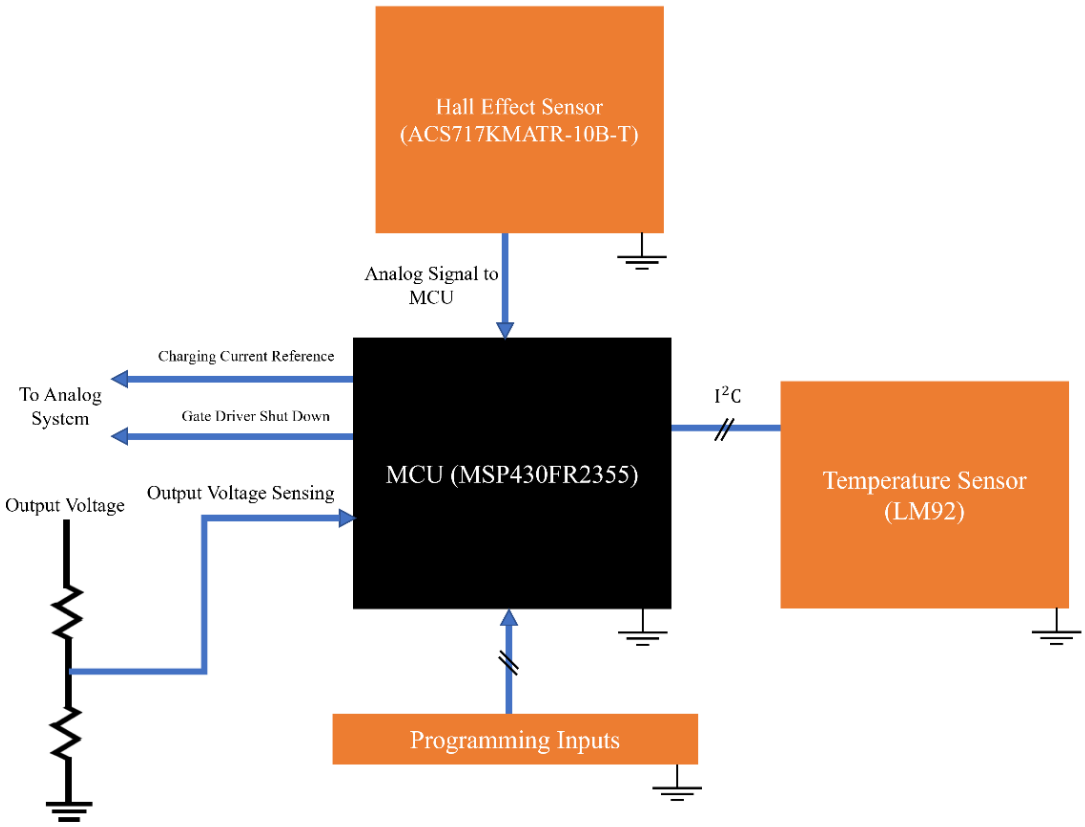

Figure 45: High level diagram of digital and sensing systems

The MCU utilized the inter-integrated circuit (I^2C) communication protocol to communicate with the temperature sensor, while using an ADC to read the information that was output by the Hall effect sensor. The MCU is programmed using Texas Instruments' Spy-Bi-Wire JTAG protocol.

The MCU is responsible for several control signals that interact with the analog circuitry in the charging system. Utilizing general purpose input/output (GPIO), it can shut down the gate driver responsible for driving the transistors. This ability is extremely useful during the discharge phase of the charging protocol. The MCU also uses an ADC to sense the output voltage via a resistor divider. To output the charging current reference to the PWM controller, a DAC is utilized. The DAC converts the given digital number to an output voltage proportional to the supply voltage provided to the MCU.

The general structure of the digital and sensing system has been described. Now, the software governing the MCU will be examined. This software will assist the system in meeting the goals as described in the introduction to this section.

Software Flowchart Discussion

The software used to conduct the cycling experiments is illustrated below in Figure 46.

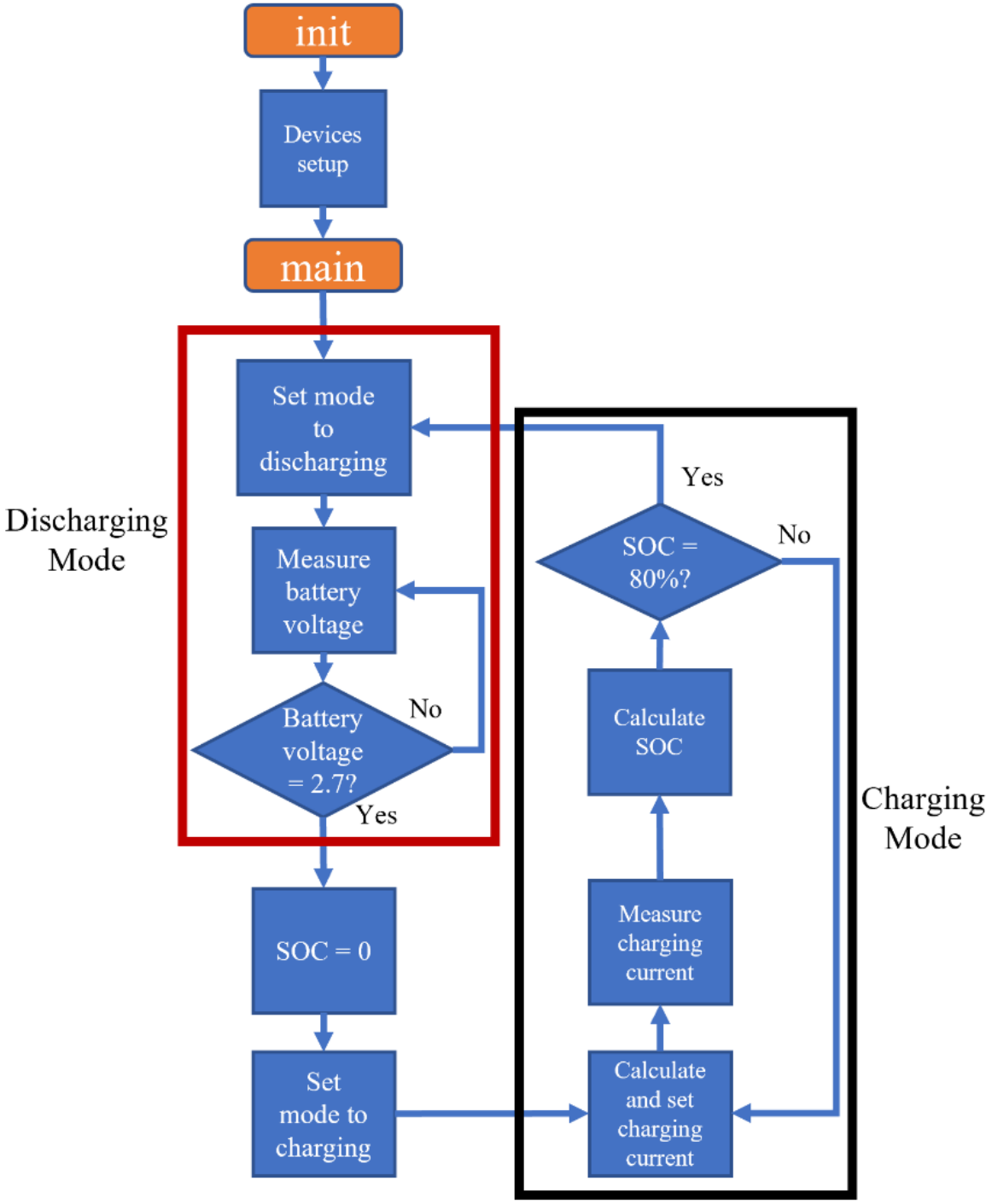

Figure 46: Charging system software flowchart

A high level description of this flowchart will now be presented; then the blocks within the flowchart will be examined in more detail. First, initialization takes place, meaning that proper power is provided, and the system reverts to a known state. Then, all sensing devices and on-chip modules are initialized to their start-up values. To ensure that the initial SOC of the battery under test is known, the system will discharge the cell to 2.7 V. Recall that this voltage has been chosen as the point that determines 0% SOC. Once this voltage is reached, the system begins the charging protocol. SOC is known, so the required charging current can be calculated. This current is then set by providing the reference to the PWM controller. The MCU will then sense the output current and, using on-chip timers, calculate the SOC added in that time frame. This process will then repeat until the MCU calculates that the cell has reached 80% SOC, at which point the cell will immediately begin discharging. There is no rest between the charging and discharging phases. The presented blocks will now be discussed in more detail.

Initialization

The initialization process handles the set up for all sensors and GPIO. First, the GPIO are configured; this allows them to later initialize the peripheral sensors. These involve the simple input and outputs used to send digital signals such as the GPIO used to shut down the transistor gate driver and enable the discharging circuit. Then, GPIO using their secondary and tertiary functions are initialized. There include I^2C data lines, ADCs, and DAC. Next, variables were set to initial values, and several on-chip modules were initialized. The on-chip modules used include a timer module and several interrupt modules to handle the required measurement devices.

Discharging Mode

After all initializations have taken place, the cell under test will be discharged to set a known SOC. Recall that the simple corrected Coulomb counting SOC determination method requires a known initial condition. During the discharge, several operations are continually running. The battery voltage is measured and used to determine the end of discharge point. The discharging current is being measured but during the discharging process there is no need to calculate SOC, as the 0% SOC indication is found from the battery voltage. Battery temperature is also measured and monitored. Monitoring the battery temperature is extremely important as if the battery begins to enter thermal runaway, the increase in temperature can be detected and the battery and the discharging circuit can be disabled. These data are stored and when the storage variable reaches the predetermined size, the data are logged onto an SD card and the storage variable is cleared. Once the cell under test reaches 2.7 V, the system will set the SOC to 0% and enter charging mode.

Charging Mode

In charging mode, the proposed charging protocol is implemented. Using the set SOC from the discharging process, the charging current is calculated. As this protocol requires that the initial charging current to be 3C, a soft start function allows the charging current to rise to maximum over 200 ms. The current through the cell is then measured and utilized to calculate the next SOC value. During this process, cell voltage and temperature are continually monitored to ensure safety in the process. Just as during the discharging process, the data are stored in a storage variable that is then written to the SD card when the predefined size is reached. The system will continually set the current reference using the proposed charging equation, measure

the output current, and calculate SOC until the SOC has reached 80%. At this point the software will reenter discharging mode and the process will repeat.

Confirmation of Cycling Software and Parallel Operation

After the cycling software had been fully developed and incrementally tested, a multi-cycle test was conducted to verify the proper operation of the charging system. To accompany the charging systems, a power supply PCB was created. This PCB housed two AC to DC converters; these converters were used separately for the signal and power voltage busses. It was desired to test several chargers at once, so this power supply PCB was created with the power capacity to supply six cycling systems. This system is illustrated below in Figure 47, with three cycling systems connected.

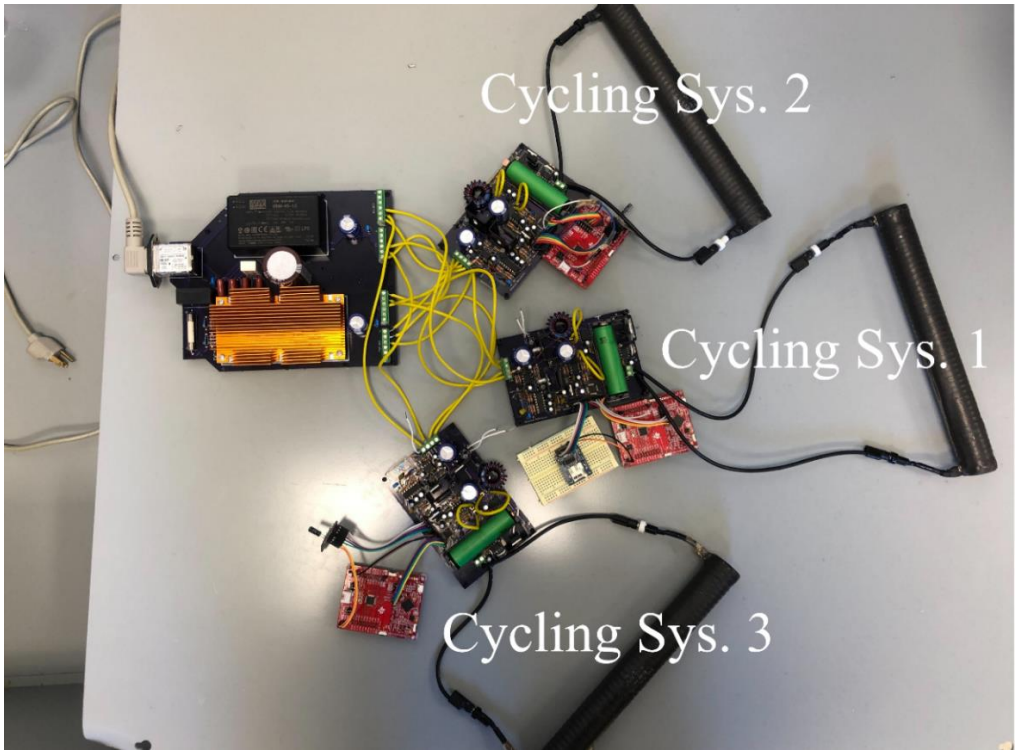

Figure 47: Multi-cycle multi-system software testing configuration

The power supply is illustrated on the left side of Figure 47 and is connected to each charging system. Each cycling system is accompanied by an MSP-EXP430FR2355, a development kit used to flash and provide debug information about the MSP430FR2355 MCU in charge of each system.

The charging systems were then tested in parallel as illustrated in Figure 47. They were tested continuously for 7 hours which constituted 6 complete cycles for each cell, with some variation in final SOC of each individual cell due to slightly differing initial SOCs. It was found that all cycling systems were functioning according to expectations, so the data produced by the charging systems was extremely similar. Battery current, voltage, and temperature as a function of time, taken from cycling system 2, is illustrated in Figure 48.

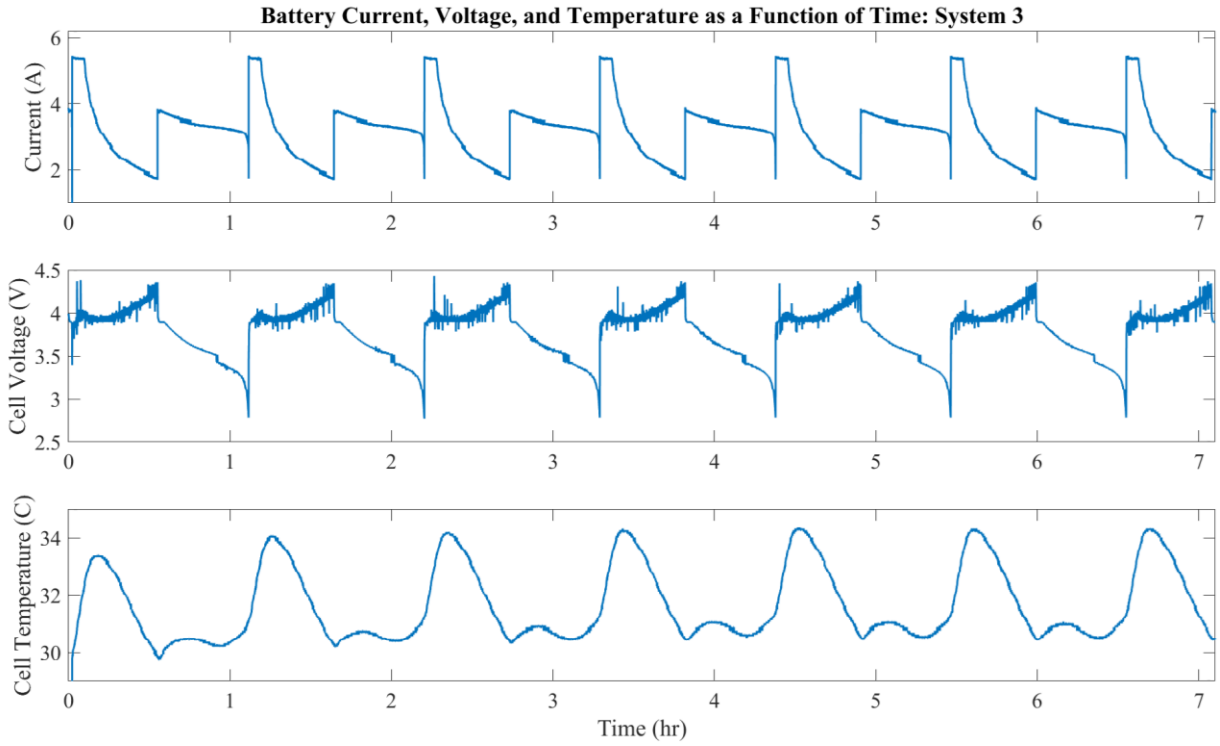

Figure 48: Battery current, voltage, and temperature as a function of time for system 2

The previous figure clearly illustrates that three charging systems can operate in parallel, properly implementing the proposed charging protocol, logging the required data, and remaining safe.

These data leads to two other interesting conclusions. First, the charging system reaches thermal equilibrium within two cycles. The temperatures seen during subsequent charges and discharges are almost identical, proving that the cycling system is thermally stable for the duration required by the cycling experiments. Second, the cell voltages seen during the charging portion of the cycle are nearly identical. This fact validates the repeatability of the SOC determination method as variation would be seen in the cycle to cycle cell voltage if a drift in SOC was present.

Experimental Setup: Long Term Cycling

With hardware and software created and confirmed for the charging system, long test cycling could begin. To determine the validity of the proposed charging protocol, commercial LIBs were cycled 350 times. The previously described software and hardware were configured in the arrangement illustrated in Figure 47. Fresh VTC4 cells were assigned to each cycling system. The multi-charging cycling system was placed inside of a large steel enclosure to contain any fires or unexpected failures during cycling and BC type extinguisher was kept near the enclosure. This enclosure included a removable lid as illustrated in Figure 49.

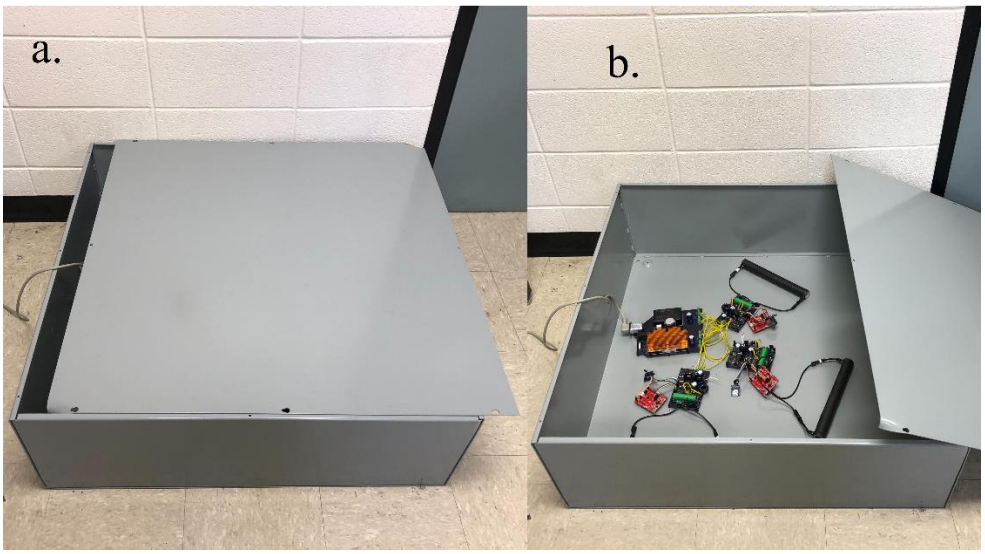

Figure 49: (a) Cycling environment with closed lid and (b) cycling environment with open lid

To mitigate safety concerns, the cycling systems were only operated with a researcher present in the laboratory. This means that cycling tests were started in the morning, allowed to run for the duration of business hours, and then shut down when the researcher left the lab for the day. This incremental cycling of the cells led to noticeable notches in the data and will be explained as data is presented.

To offer a comparison to the cell undergoing the fast charging protocol, another VTC4 from the same manufacturer was cycled for 350 cycles using the traditional 1C CC/CV charging method, this technique was able to attain 80% in about 50 minutes. This cycling test was performed using the LBT21084HC Arbin cycler.

ANALYSIS OF RESULTS

First, data pertaining to the fast charging system will be presented. This includes analysis of the charge and discharge capacity as a function of time, cell voltage sampled from every 50th cycle, temperatures achieved by the chargers during cycling and the average charging time. Next, the EIS measurements of the fast charged cell will be compared to that of the CC/CV charged cell. Finally, the fast charged and CC/CV charged cell will be destructively investigated and the graphite anodes will be inspected for signs of lithium plating.

During the process of the test, an error was encountered with charging system one. These errors stemmed from microprocessor and other digital IC failure. To mitigate this, the software governing system one was changed several time during the cycling process. Therefore, while the charging system was able to implement the charging protocol safely and accurately, the data received from system one will not be used in analysis.

Systems 2 and 3 were able to maintain operation through the cycling process and both presented similar outcomes in terms of charge and discharge capacity and maximum temperatures reached. Data from system 2 will be presented in analysis and data from system 3 will be included Appendix B.

Cycling Results

The charge and discharge capacities recorded from system 2 are illustrated below in Figure 50.

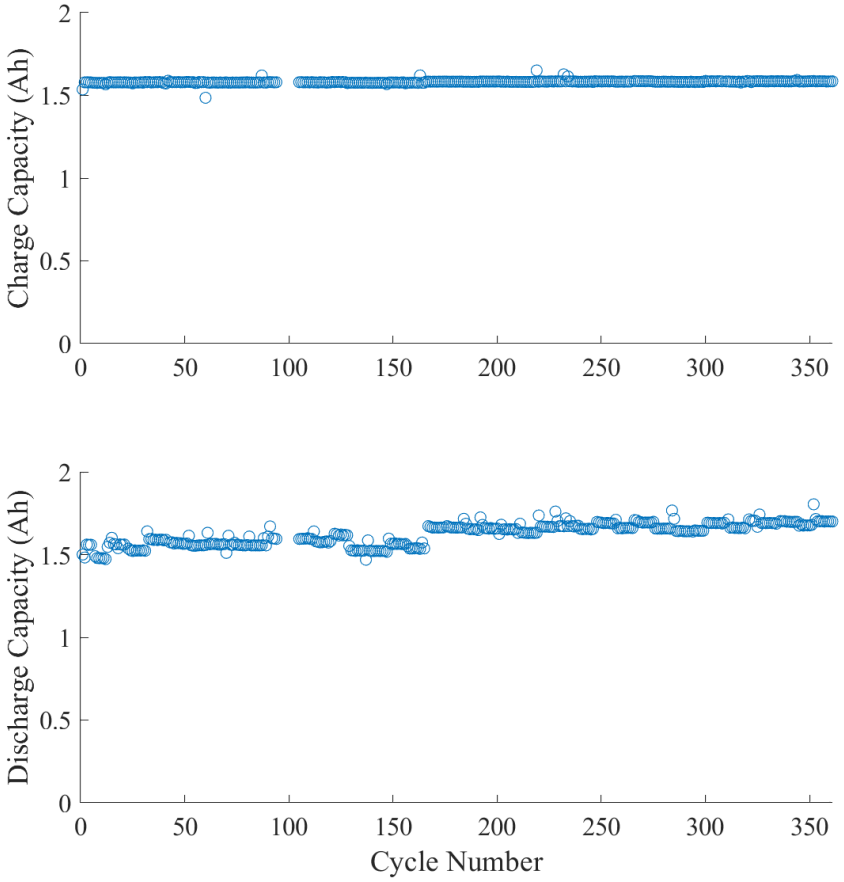

Figure 50: Charge and discharge capacity as a function of cycle number

From Figure 50, charge capacity remains very constant through the entirety of the cycling process. Recall, that the capacity of the VTC4 was determined to be 1.9 Ah; therefore, charging this cell to 80% SOC will result in a charge capacity of 1.52 Ah . This further confirms the repeatability and accuracy of the charging system in implementing the fast charging protocol. As stated previously, cycling tests were only conducted with a researcher present in the lab during

business hours. The stopping and restarting of the cycling process created the groupings evident in the discharge capacity. Notably, when the cell neared the 160 cycle mark, a jump in discharge capacity is noticed. The ratio of the charge capacity to the discharge capacity is called the Coulombic efficiency, and at this point the Coulombic efficiency becomes greater than 1. This means that the cell was discharging more capacity than was being input. As this is not possible, a system error occurred at this point as the discharge capacity jumps up by several milliamp hours and remains constant for the remained of the experiment. The cause of this error is believed to have originated in the MCU and the software. This jump in discharge capacity as well as the daily groups are illustrated by more closely investigating the previous figure.

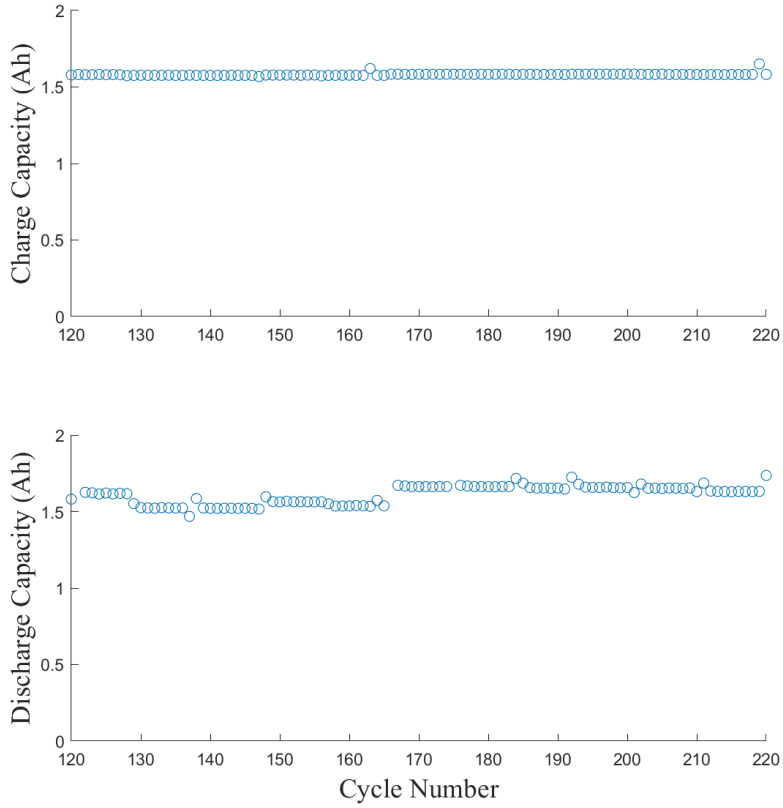

Figure 51: Charge and discharge capacity as a function of cycle number for cycles 120 to 220

These data illustrate that the fast charging protocol did not reduce the capacity in a noticeable way during this experiment.

Next, the cell voltage sampled from every 50th cycle will be inspected. The purpose of inspecting the cell voltage at different cycle numbers is to give insight into cell health. If the effective cell capacity becomes lower, due to damages by the charging protocol, this will be clear in a rising cell voltage at fixed points in the charging protocol. This cell voltage data is illustrated below in Figure 52.

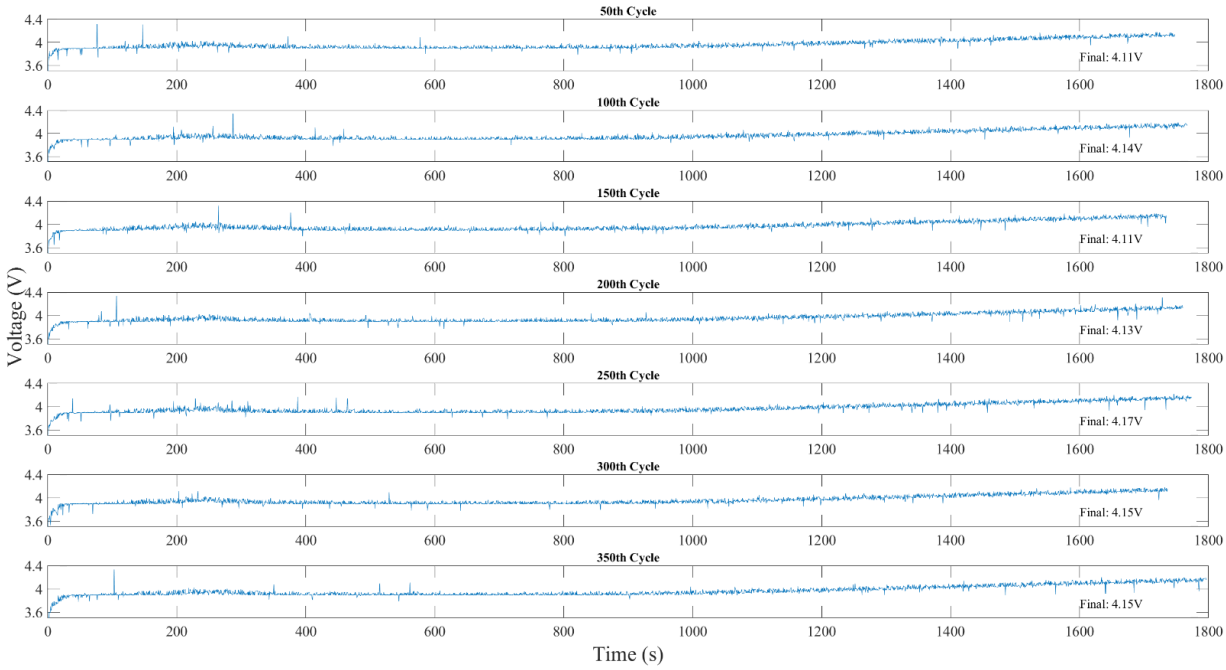

Figure 52: Voltage profiles as a function of time to reach 80 % SOC while charging the commercial LIB using the proposed fast charging protocol

Note that the proposed charging protocol is a function of SOC but evaluating the cell voltage as a function of time is still valid, as the charging protocol should be repeatable. The cell voltage is similar between all cycles illustrated in the previous figure but there is some variation in the

required charging time. This is due to the sampling error of the Hall effect sensor and the imperfections in the timing systems of the MCU. Also, there is no trend in the final voltage of the cell during the charging process. This signifies that there is no appreciable capacity decline suffered by the cell under test as an upward trend in cell voltage would be clear as the cycle number increased. It is not clear from the cell voltage data that the fast charging protocol has had a significant effect on cell health.

Next, the temperature data captured during charge and discharge will be inspected. While the temperature sensor physically touches the cell, the power losses of the charging power electronics also affect the temperature readings as they are physically close and mechanical connected. The average and max temperatures recorded during charge and discharge are compared to the ambient temperature in Figure 53.

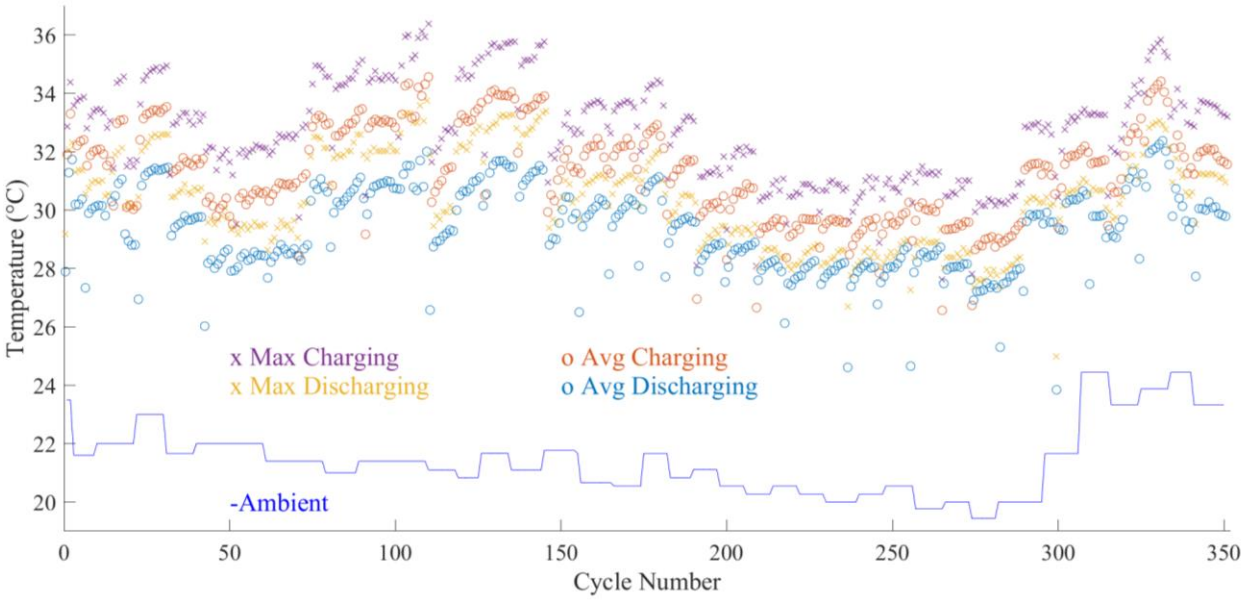

Figure 53: Variation in ambient and cell temperature while cycling the commercial 18650 LIB using the proposed fast charging protocol

Overlaying the ambient temperature illustrates the rise above ambient and helps explain the trends seen in the charging data. The average and maximums seen during the charging process, using the key present on the figure, are higher than those seen during discharge. This is because during the charging process there are high currents and losses in the operational power electronics contributing to the heat in the system. The rise above ambient is constant, with a maximum of approximately 14 °C, illustrating that the proposed charging protocol is not stressing the cell beyond its operating limits. The daily groupings are also seen in this data, with the system requiring several cycles to reach thermal equilibrium, as is clear in the average temperature during the charge and discharge.

Finally, the charging time can be inspected. The required charging time as function of cycle is illustrated in Figure 50.

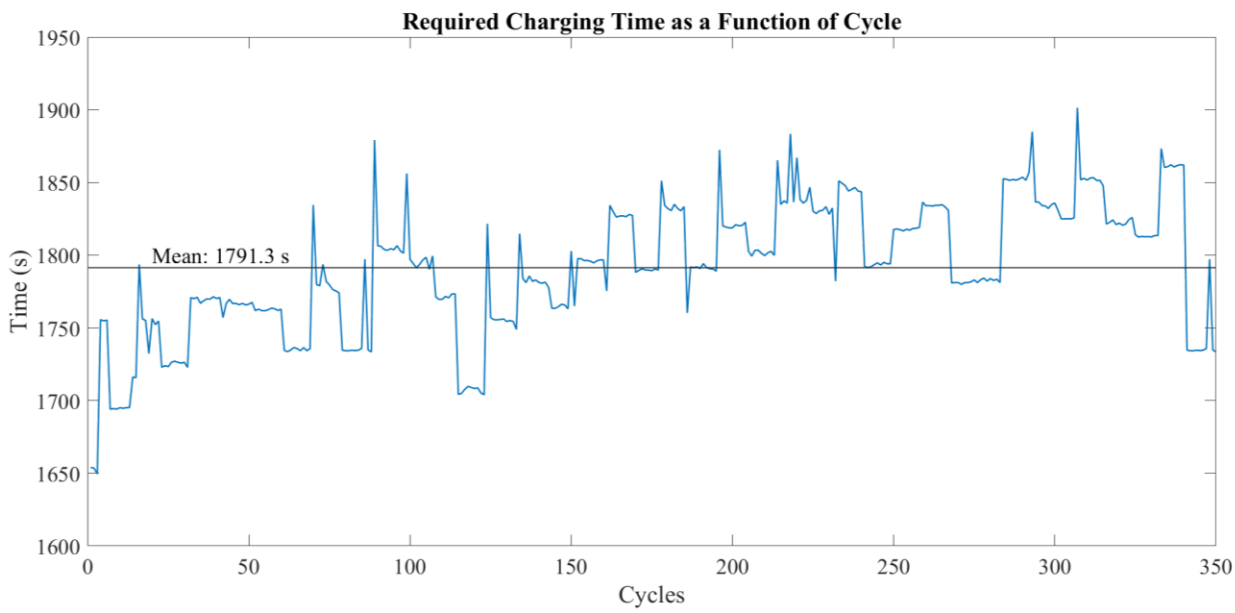

Figure 54: Required charging time as a function of cycle

The groups created by the daily cycling are evident in this figure. The variations in charging times illustrate that the charging protocol could be dependent on ambient temperature, rest time, and overall system error. The mean of all charging times was found to be 1793.1 seconds, or 29 minutes and 52 seconds. This shows improvement on the CC/CV charging protocol which requires 50 minutes to reach 80% SOC [3].

Inspecting the discharge capacity as a function of cycle number, the cell voltage during charge of every 50th cycle, maximum and average temperatures attained by the system during charge and discharge, and the required charging time it was found that the cell under test was not being stressed beyond its limits. These data confirm the proposed charging protocol as a safe and fast means of charging the VTC4 commercial LIB.

While the inspected data provide excellent insight to the health of the cell through the cycling experiment, there is no way to understand if appreciable lithium plating took place during the charging process. To evaluate the amount of lithium plating that took place during the cycling experiment, the cell was measured using EIS and destructively examined.

EIS and Destructive Examination Results

First, EIS experiments were conducting on the fast-charged cell, the 1C CC/CV charged cell, and a fresh VTC4 LIB. To allow for proper impedance comparisons, the tests were conducted at a cell voltage of 3.6 V [36]. The cells were also destructively examined by removing the graphite anode. The Nyquist plot of the spectra and unrolled anodes are illustrated in Figure 55. The impedance of each cell shows inductive behavior which can be attributed to the leads used to conduct the measurements. Within the medium to low frequency area a semi-circle is seen; this is related to the charge transfer process. Then a linear region, with respect to the Z`

axis, is observed; this is related to the solid state diffusion process [36]. The impedance spectra clearly show that the cycled cells have aged, as evident in their increase in resistance, but this aging is similar, signifying that the fast-charged cell is not being stressed beyond reasonable limits when compared to the CC/CV protocol [36].

Then, the cells were deconstructed inside of a glovebox to inspect the anode surface. As illustrated in the insert in Figure 55, photographs show no obvious signs of lithium plating on either the CC/CV charged or fast charged cell [36]. This indicates that the fast charging protocol can safely and quickly charge commercial LIBs without lithium plating on the graphite anode.

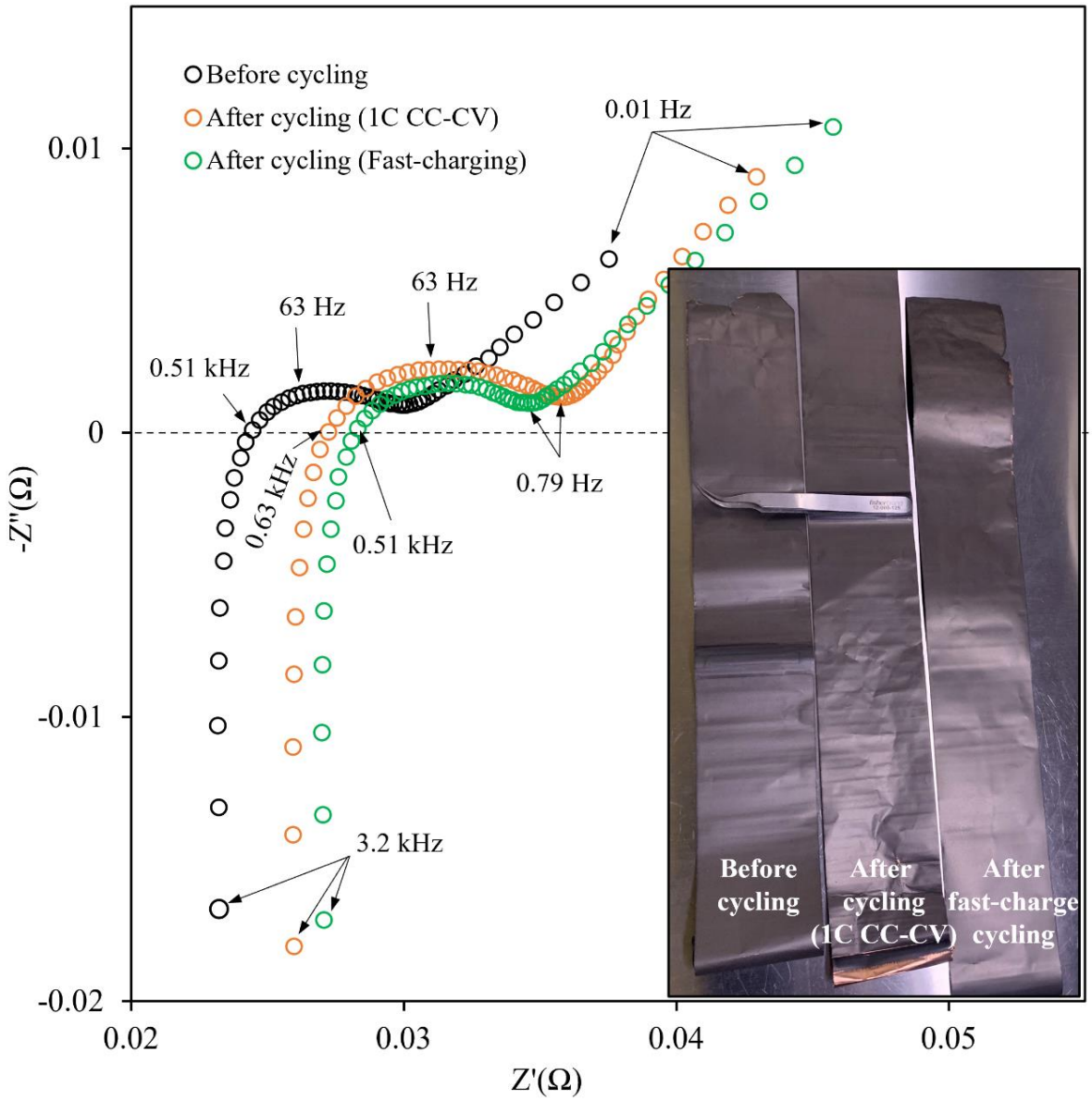

Figure 55: Electrochemical impedance spectra (EIS) of new and aged commercial LIBs. The insets show the optical photographs of the graphite anodes disassembled from the new and aged commercial LIBs [36]

With confirmation that the proposed fast charging protocol did not cause noticeable lithium plating over the course of 350 cycles, the validity of the circuit model and predicted fast charging current was proven.

FUTURE WORK AND CONCLUSION

The work conducted in this thesis was focused on a single LIB. The conclusions drawn from these results may generalize to multi-cell modules and multi-model packs but there are several unknown factor in increasing the scale in the fast charging system. First, in multi-cell packs, safety becomes a much larger issue. Cells are often confined close to one another, allowing for less heat dissipation. How the proposed fast charging protocol will perform charging cells in this configuration is unknown. Second, is the use of the equivalent circuit model in finding the model of a larger battery module or pack. Using basic circuit analysis rules, the equivalent circuit models can be placed in series and parallel, just as commercial cells are used to construct large battery packs, but it is unknown if this will properly model the pack.

Charging of lithium ion battery cells and packs is an extremely important focus for the future of electrical vehicles and personal electronics. Fast charging will eventually enable the recharging process required for electrical vehicles to rival those of traditional automobiles. But several considerations must be made in developing new fast charging methods. First, the charging process must balance the fast charging time with the degradation of the battery pack or cell and second the process must remain safe. In the research enabling this thesis, and work complete solely for this thesis, a proposed charging protocol was developed with the goal of eliminating lithium plating during fast charging, one of the main aging factors in LIBs. This charging protocol was first tested using small cells and then scaled for use with commercial LIBs. A custom battery cycling system was constructed, incorporating a synchronous Buck converter to be used as the charging circuit, and separate autonomous discharging circuit. Using the developed fast charging protocol and system, the VTC4 commercial LIB was cycled 350

times. The data generated during this experiment verified that the fast charging protocol was safe and faster than the traditional 1C CC/CV charge.

REFERENCES CITED

[1] J.-M. Tarascon and M. Armand, “Issues and challenges facing rechargeable lithium batteries,” 2001. [Online]. Available: www.nature.com

[2] V. Pop, H. J. Bergveld, J. H. G. Op het Veld, P. P. L. Regtien, D. Danilov, and P. H. L. Notten, “Modeling Battery Behavior for Accurate State-of-Charge Indication,” *J. Electrochem. Soc.*, vol. 153, no. 11, p. A2013, 2006, doi: 10.1149/1.2335951.

[3] “Sony US18650VTC4 Datasheet.” Jun. 29, 2012.

[4] J. B. Goodenough and K.-S. Park, “The Li-Ion Rechargeable Battery: A Perspective,” *J. Am. Chem. Soc.*, vol. 135, no. 4, pp. 1167–1176, Jan. 2013, doi: 10.1021/ja3091438.

[5] G. Zubi, R. Dufo-López, M. Carvalho, and G. Pasaoglu, “The lithium-ion battery: State of the art and future perspectives,” *Renew. Sustain. Energy Rev.*, vol. 89, pp. 292–308, Jun. 2018, doi: 10.1016/j.rser.2018.03.002.

[6] D. Deng, “Li-ion batteries: Basics, progress, and challenges,” *Energy Sci. Eng.*, vol. 3, no. 5, pp. 385–418, Sep. 2015, doi: 10.1002/ese3.95.

[7] M. Winter, J. O. Besenhard, M. E. Spahr, and P. Novák, “Insertion Electrode Materials for Rechargeable Lithium Batteries,” *Adv. Mater.*, vol. 10, no. 10, pp. 725–763, Jul. 1998, doi: 10.1002/(SICI)1521-4095(199807)10:10<725::AID-ADMA725>3.0.CO;2-Z.

[8] D. Lisbona and T. Snee, “A review of hazards associated with primary lithium and lithium-ion batteries,” *Process Saf. Environ. Prot.*, vol. 89, no. 6, pp. 434–442, Nov. 2011, doi: 10.1016/j.psep.2011.06.022.

[9] Z. Li, J. Huang, B. Yann Liaw, V. Metzler, and J. Zhang, “A review of lithium deposition in lithium-ion and lithium metal secondary batteries,” *J. Power Sources*, vol. 254, pp. 168–182, May 2014, doi: 10.1016/j.jpowsour.2013.12.099.

[10] B. K. Purushothaman and U. Landau, “Rapid Charging of Lithium-Ion Batteries Using Pulsed Currents,” *J. Electrochem. Soc.*, vol. 153, no. 3, p. A533, 2006, doi: 10.1149/1.2161580.

[11] S. S. Zhang, “The effect of the charging protocol on the cycle life of a Li-ion battery,” *J. Power Sources*, vol. 161, no. 2, pp. 1385–1391, Oct. 2006, doi: 10.1016/j.jpowsour.2006.06.040.

[12] Z. Guo, B. Y. Liaw, X. Qiu, L. Gao, and C. Zhang, “Optimal charging method for lithium ion batteries using a universal voltage protocol accommodating aging,” *J. Power Sources*, vol. 274, pp. 957–964, Jan. 2015, doi: 10.1016/j.jpowsour.2014.10.185.

[13] A. Manthiram, “A reflection on lithium-ion battery cathode chemistry,” *Nat. Commun.*, vol. 11, no. 1, Dec. 2020, doi: 10.1038/s41467-020-15355-0.

[14] “BU-205: Types of Lithium-ion,” *Battery University*. https://batteryuniversity.com/article/bu-205-types-of-lithium-ion (accessed Dec. 30, 2022).

[15] N. Nitta, F. Wu, J. T. Lee, and G. Yushin, “Li-ion battery materials: Present and future,” *Mater. Today*, vol. 18, no. 5, pp. 252–264, Jun. 2015, doi: 10.1016/j.mattod.2014.10.040.

[16] R. Analyst, D. Galves, and P. Nolan, “Electric Cars: Plugged In 2 A mega-theme gains momentum Rod Lache,” 2009. [Online]. Available: http://gm.db.com/IndependentResearch

[17] S. Y. Chung, J. T. Bloking, and Y. M. Chiang, “Electronically conductive phospho-olivines as lithium storage electrodes,” *Nat. Mater.*, vol. 1, no. 2, pp. 123–128, Oct. 2002, doi: 10.1038/nmat732.

[18] B. Lung-Hao Hu, F. Y. Wu, C. T. Lin, A. N. Khlobystov, and L. J. Li, “Graphene-modified LiFePO4 cathode for lithium ion battery beyond theoretical capacity,” *Nat. Commun.*, vol. 4, 2013, doi: 10.1038/ncomms2705.

[19] P. Mukherjee *et al.*, “Surface Structural and Chemical Evolution of Layered $LiNi_{0.8}Co_{0.15}Al_{0.05}O_2$ (NCA) under High Voltage and Elevated Temperature Conditions,” *Chem. Mater.*, vol. 30, no. 23, pp. 8431–8445, Dec. 2018, doi: 10.1021/acs.chemmater.7b05305.

[20] K. T. Lee, S. Jeong, and J. Cho, “Roles of Surface Chemistry on Safety and Electrochemistry in Lithium Ion Batteries,” *Acc. Chem. Res.*, vol. 46, no. 5, pp. 1161–1170, May 2013, doi: 10.1021/ar200224h.

[21] S. Heng *et al.*, “Controllable solid electrolyte interphase precursor for stabilizing natural graphite anode in lithium ion batteries,” *Carbon*, vol. 159, pp. 390–400, Apr. 2020, doi: 10.1016/j.carbon.2019.12.054.

[22] C. Li *et al.*, “An advance review of solid-state battery: Challenges, progress and prospects,” *Sustain. Mater. Technol.*, vol. 29, p. e00297, Sep. 2021, doi: 10.1016/j.susmat.2021.e00297.

[23] Y.-N. Yang, Y.-X. Li, Y.-Q. Li, and T. Zhang, “On-surface lithium donor reaction enables decarbonated lithium garnets and compatible interfaces within cathodes,” *Nat. Commun.*, vol. 11, no. 1, p. 5519, Nov. 2020, doi: 10.1038/s41467-020-19417-1.

[24] M. F. Lagadec, R. Zahn, and V. Wood, “Characterization and performance evaluation of lithium-ion battery separators,” *Nat. Energy*, vol. 4, no. 1, pp. 16–25, Dec. 2018, doi: 10.1038/s41560-018-0295-9.

[25] V. Chandran, C. K. Patil, A. Karthick, D. Ganeshaperumal, R. Rahim, and A. Ghosh, "State of charge estimation of lithium-ion battery for electric vehicles using machine learning algorithms," *World Electr. Veh. J.*, vol. 12, no. 1, 2021, doi: 10.3390/wevj12010038.

[26] Y. Tian, B. Xia, W. Sun, Z. Xu, and W. Zheng, "A modified model based state of charge estimation of power lithium-ion batteries using unscented Kalman filter," *J. Power Sources*, vol. 270, pp. 619–626, Dec. 2014, doi: 10.1016/j.jpowsour.2014.07.143.

[27] M. Murnane and A. Ghazel, "A Closer Look at State of Charge (SOC) and State of Health (SOH) Estimation Techniques for Batteries."

[28] W. Waag, C. Fleischer, and D. U. Sauer, "Critical review of the methods for monitoring of lithium-ion batteries in electric and hybrid vehicles," *J. Power Sources*, vol. 258, pp. 321–339, Jul. 2014, doi: 10.1016/j.jpowsour.2014.02.064.

[29] L. Lu, X. Han, J. Li, J. Hua, and M. Ouyang, "A review on the key issues for lithium-ion battery management in electric vehicles," *J. Power Sources*, vol. 226, pp. 272–288, Mar. 2013, doi: 10.1016/j.jpowsour.2012.10.060.

[30] T. Huria, G. Ludovici, and G. Lutzemberger, "State of charge estimation of high power lithium iron phosphate cells," *J. Power Sources*, vol. 249, pp. 92–102, 2014, doi: 10.1016/j.jpowsour.2013.10.079.

[31] M. Mastali, J. Vazquez-Arenas, R. Fraser, M. Fowler, S. Afshar, and M. Stevens, "Battery state of the charge estimation using Kalman filtering," *J. Power Sources*, vol. 239, pp. 294–307, 2013, doi: 10.1016/j.jpowsour.2013.03.131.

[32] D. Anseán, M. González, J. C. Viera, V. M. García, C. Blanco, and M. Valledor, "Fast charging technique for high power lithium iron phosphate batteries: A cycle life analysis," *J. Power Sources*, vol. 239, pp. 9–15, 2013, doi: 10.1016/j.jpowsour.2013.03.044.

[33] T. T. Vo, X. Chen, W. Shen, and A. Kapoor, "New charging strategy for lithium-ion batteries based on the integration of Taguchi method and state of charge estimation," *J. Power Sources*, vol. 273, pp. 413–422, Jan. 2015, doi: 10.1016/j.jpowsour.2014.09.108.

[34] P. Arora, R. E. White, and M. Doyle, "Capacity Fade Mechanisms and Side Reactions in Lithium-Ion Batteries," *J. Electrochem. Soc.*, vol. 145, no. 10, pp. 3647–3667, Oct. 1998, doi: 10.1149/1.1838857.

[35] J. Sieg *et al.*, "Fast charging of an electric vehicle lithium-ion battery at the limit of the lithium deposition process," *J. Power Sources*, vol. 427, pp. 260–270, Jul. 2019, doi: 10.1016/j.jpowsour.2019.04.047.

[36] A. Thapa, N. Hedding, and H. Gao, “Fast Charging of Commercial Lithium-ion Battery Without Lithium Plating.”

[37] A. Thapa and H. Gao, “Low-frequency Inductive Loop and Its Origin in the Impedance Spectrum of a Graphite Anode,” *J. Electrochem. Soc.*, vol. 169, no. 11, p. 110535, Nov. 2022, doi: 10.1149/1945-7111/aca364.

[38] B.-Y. Chang, “Conversion of a Constant Phase Element to an Equivalent Capacitor,” *J. Electrochem. Sci. Technol.*, vol. 11, no. 3, pp. 318–321, Aug. 2020, doi: 10.33961/jecst.2020.00815.

[39] L. Dixon, “Average Current Mode Control of Switching Power Supplies.” Unitrode, 1990.

[40] “High Speed PWM Controller - UC3823.” Unitrode, 1997.

[41] “IR2184(4)(S)-600 V, 1.8 A, half bridge gate driver with shutdown.” Infineon Technologies.

[42] “FAMILY OF WIDE-BANDWIDTH HIGH-OUTPUT-DRIVE SINGLE SUPPLY OPERATIONAL AMPLIFIERS.” Texas Instruments.

[43] “MSP430FR235x, MSP430FR215x Mixed-Signal Microcontrollers.” Texas Instruments, May 2018.

[44] “±0.33°C Accurate, 12-Bit + Sign Temperature Sensor and Thermal Window Comparator With Two-Wire Interface.” Texas Instruments, Mar. 2000.

[45] “TLV2217 Low-Dropout Fixed-Voltage Regulators.” Texas Instruments, Mar. 1992.

[46] “Low-Cost High- or Low-Side MOSFET Driver.” Microchip Technology, Jun. 2005.

[47] “EPC2015C – Enhancement Mode Power Transistor.” Efficient Power Conversion, 2021.

[48] “StrongIRFET™ IRFB7446PbF.” International Rectifier, Nov. 2014.

[49] “EPC2302 – Enhancement Mode Power Transistor.” Efficient Power Conversion, 2022.

[50] “eGaN® FET Advantages in 48 V – 12 V Power Conversion.” Efficient Power Conversion, 2018.

[51] “High-Speed, Wide-Input, Single Phase MOSFET Driver.” Maxim Incorperated, 2003.

[52] “TLV354x 200-MHz, Rail-to-Rail I/O, CMOS Operational Amplifiers for Cost-Sensitive Systems.” Texas Instruments, Oct. 2016.

[53] "TMCS1108 3% Functional Isolation Hall-Effect Current Sensor With ±100-V Working Voltage." Texas Instruments, 2021.

[54] "3A, 5A, 7.5A Low Dropout Positive Fixed Regulators." Linear Technology, Jun. 2015.

APPENDICES

APPENDIX A

CURRENT OF CAPACITIVE AND INDUCTIVE ELEMENTS IN EQUIVALENT MODEL

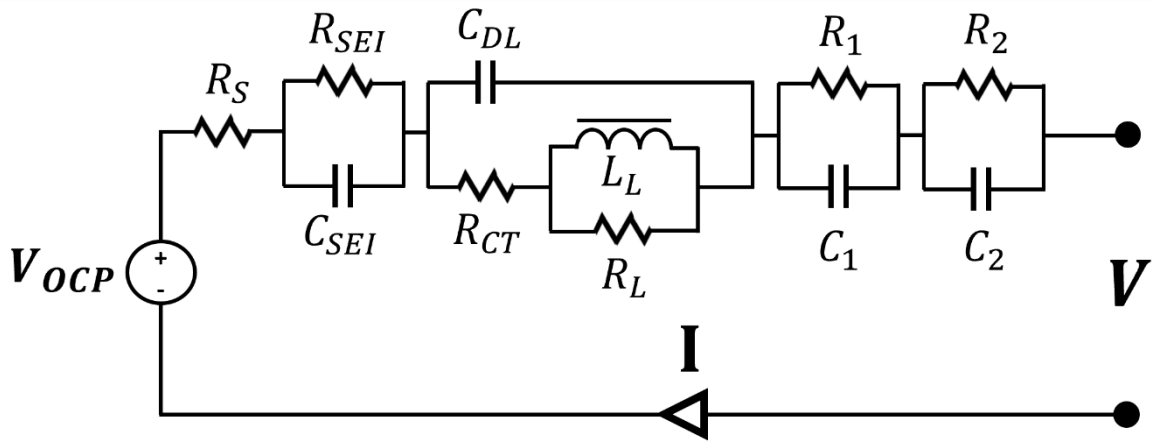

Figure A1: Electrical circuit model for predicting a fast-charging current for a LIB test cell

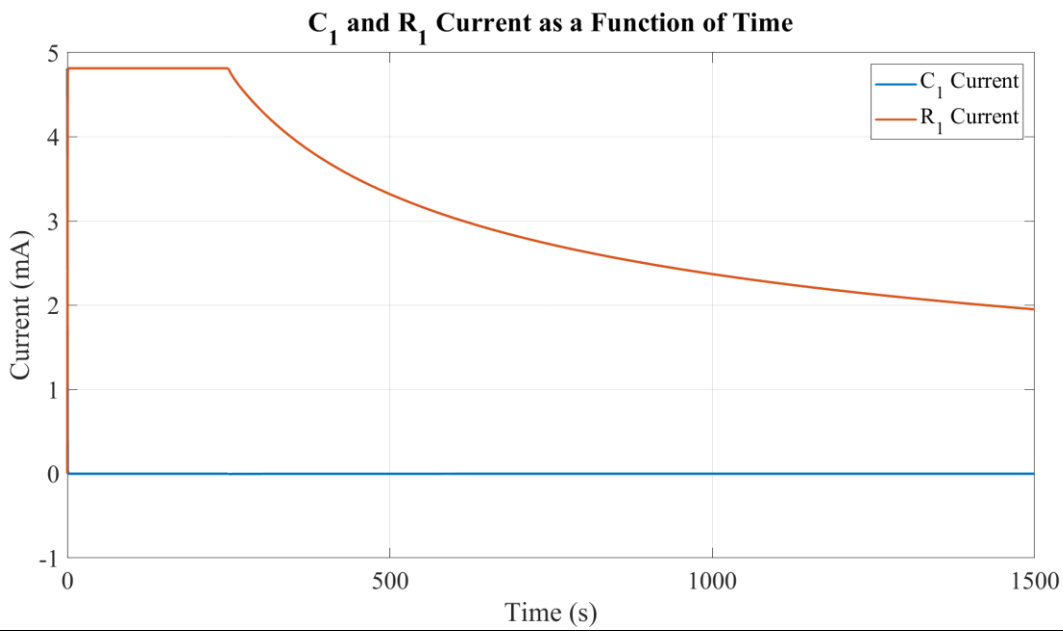

Figure A2: Comparison of C_1 and R_1 currents as a function of time during the charging process

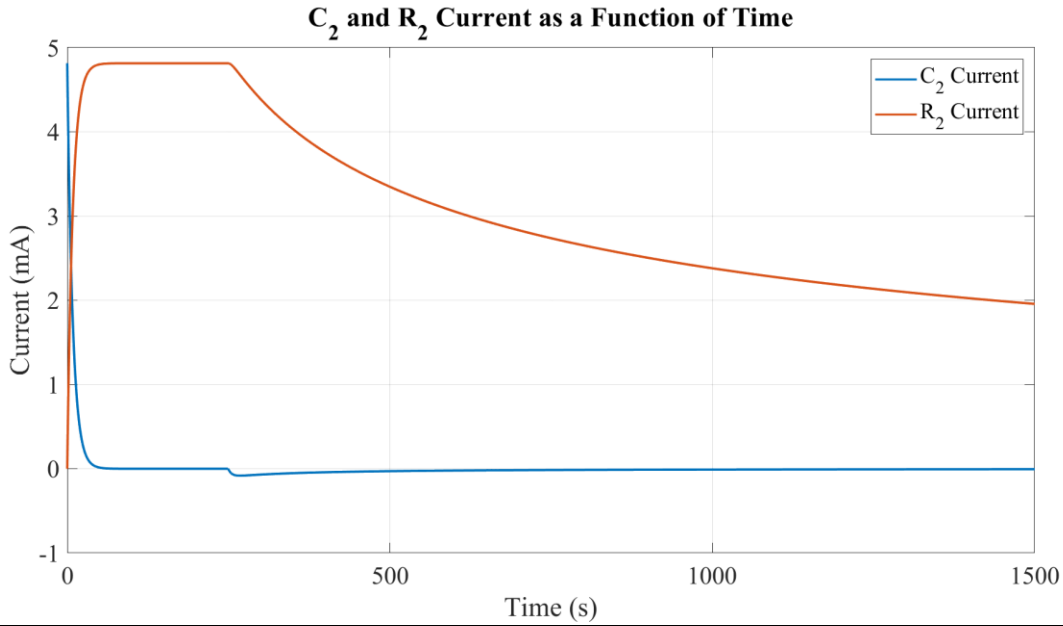

Figure A3: Comparison of C_2 and R_2 currents as a function of time during the charging process

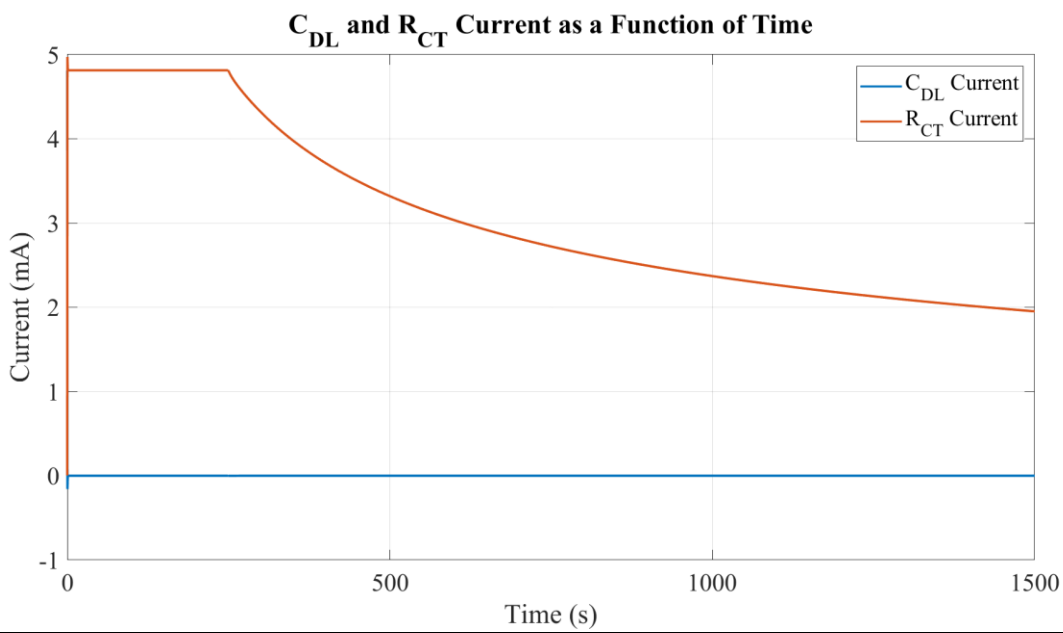

Figure A4: Comparison of C_{DL} and R_{CT} currents as a function of time during the charging process

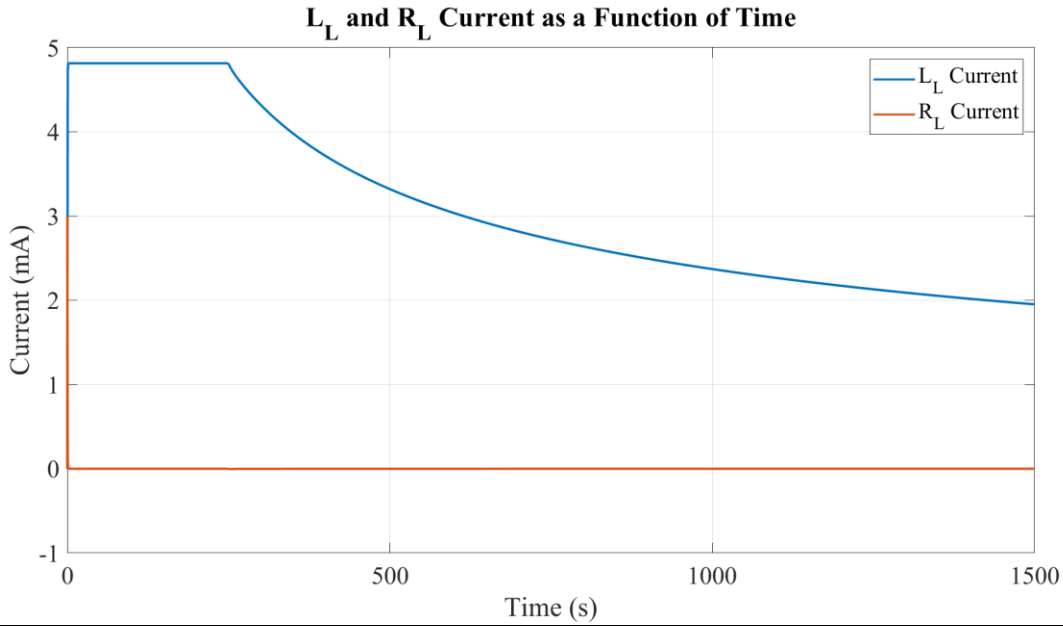

Figure A5: Comparison of L_L and R_L currents as a function of time during the charging process

APPENDIX B

CYCLING SYSTEM 3 DATA

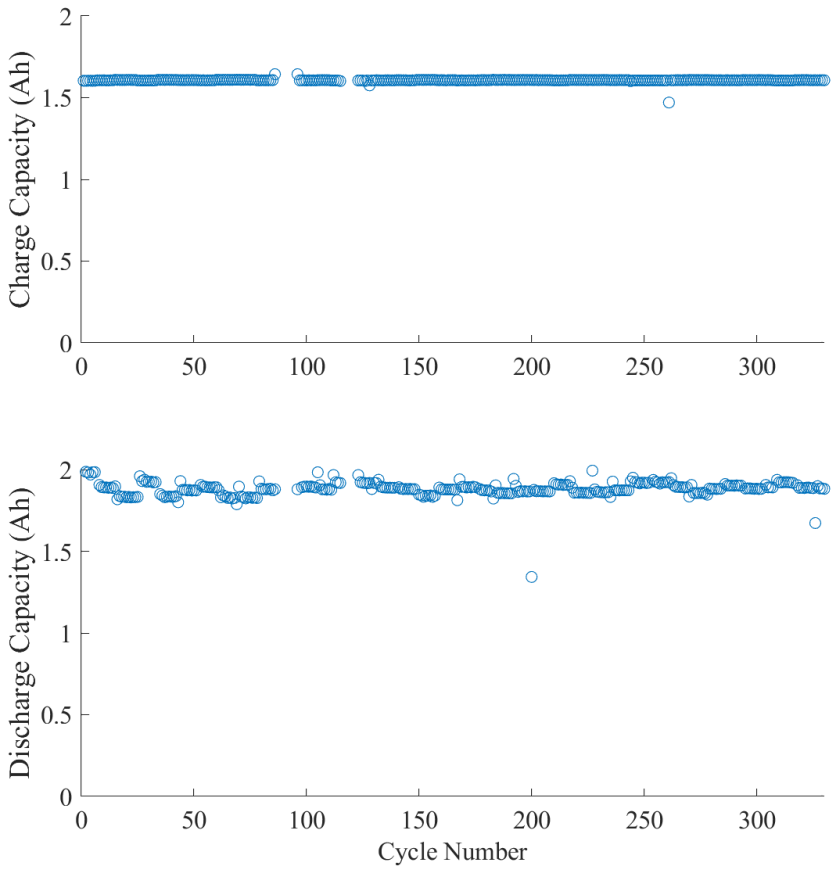

Figure B1: Charge and discharge capacity as a function of cycle number for system 3

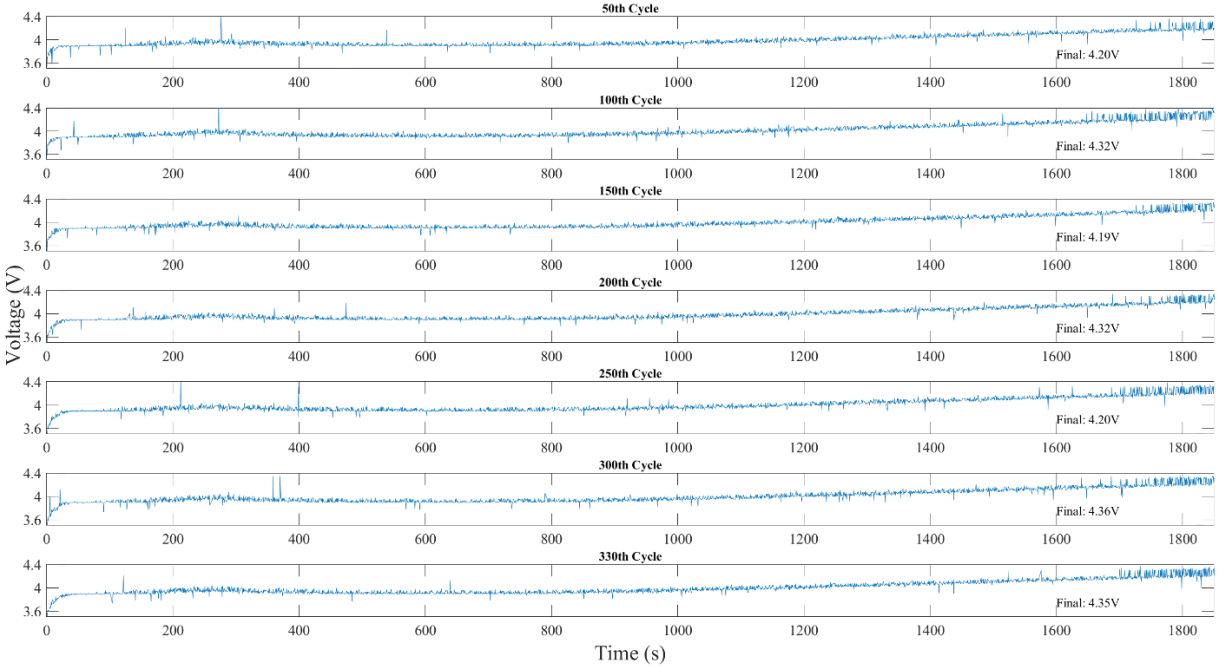

Figure B2: Voltage profiles as a function of time to reach 80 % SOC while charging the commercial LIB using the proposed fast charging protocol for system 3

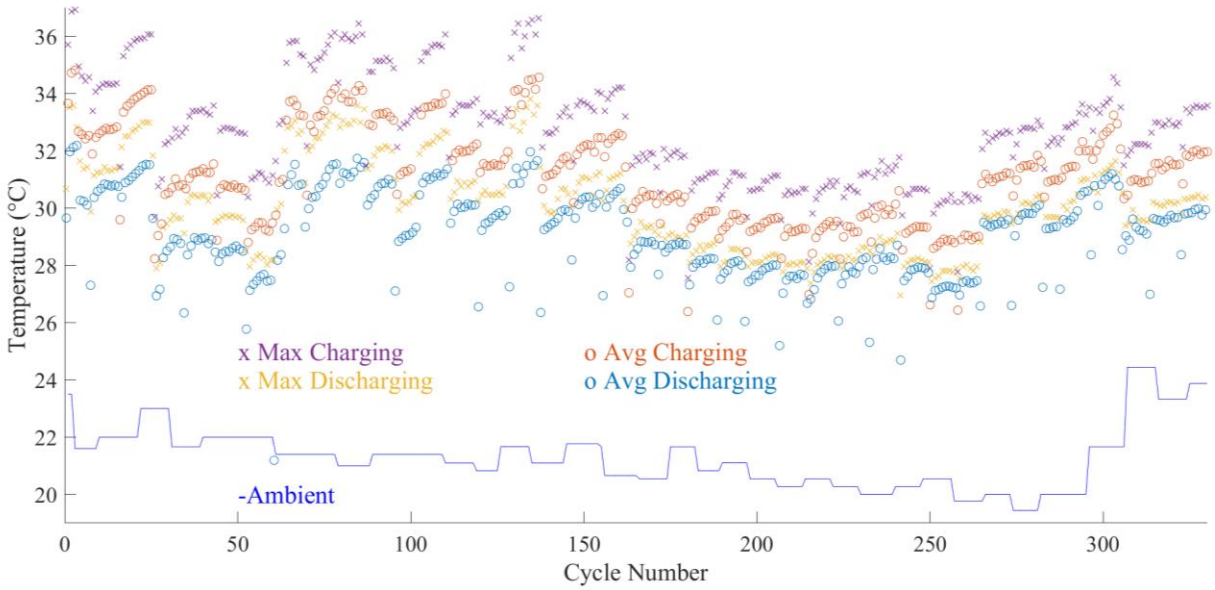

Figure B3: Variation in ambient and cell temperature while cycling the commercial 18650 LIB using the proposed fast charging protocol for system 3

APPENDIX C

SCHEMATICS AND BILL OF MATERIALS FOR SILICON MOSFET CYCYLING SYSTEM

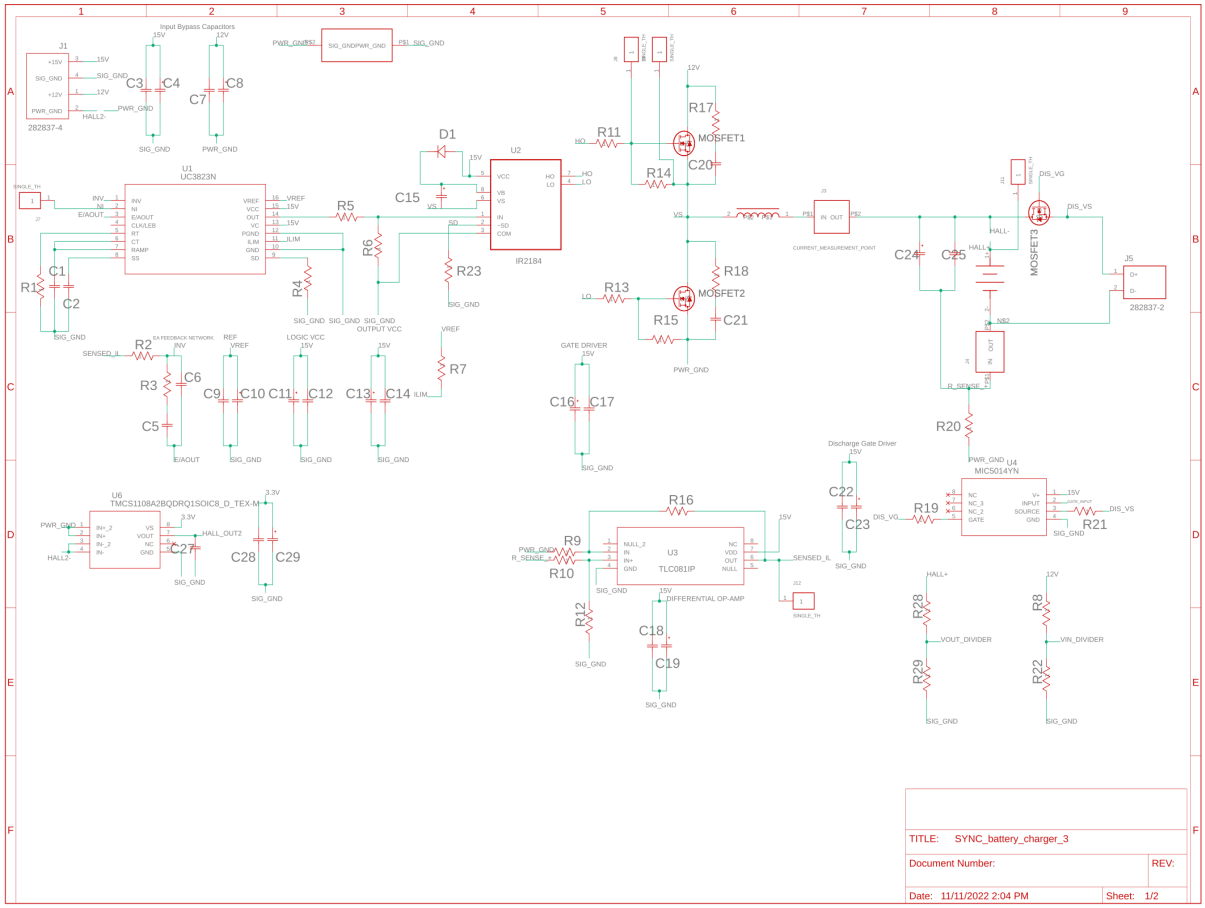

3/24/2023 11:39 AM C:\Users\nhedd\OneDrive\Documents\EAGLE\projects\SYNC_battery_charger\SYNC_battery_charger_3.sch (Sheet: 1/2)

Figure C1: Schematic page 1 for silicon based cycling system

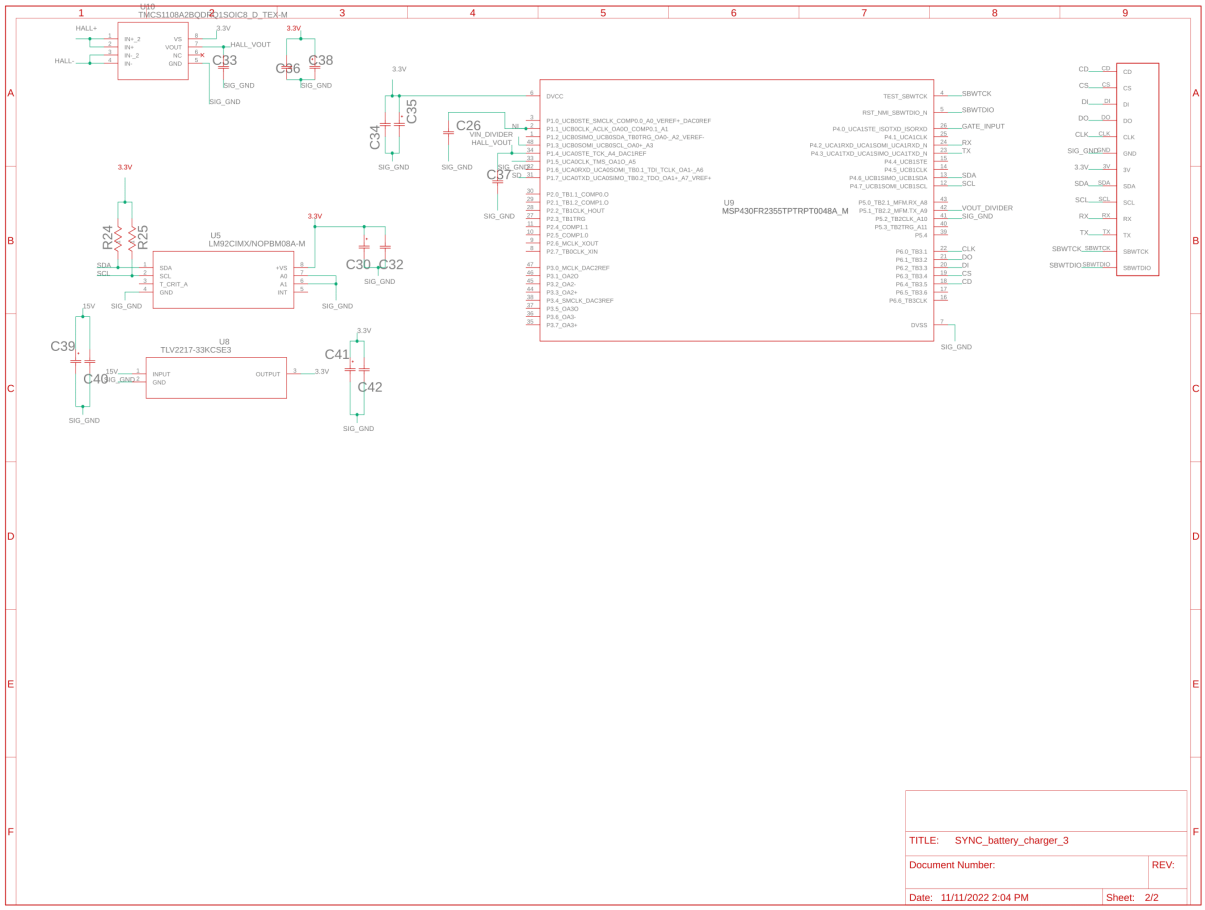

3/24/2023 11:40 AM C:\Users\nhedd\OneDrive\Documents\EAGLE\projects\SYNC_battery_charger\SYNC_battery_charger_3.sch (Sheet: 2/2)

Figure C2: Schematic page 2 for silicon based cycling system

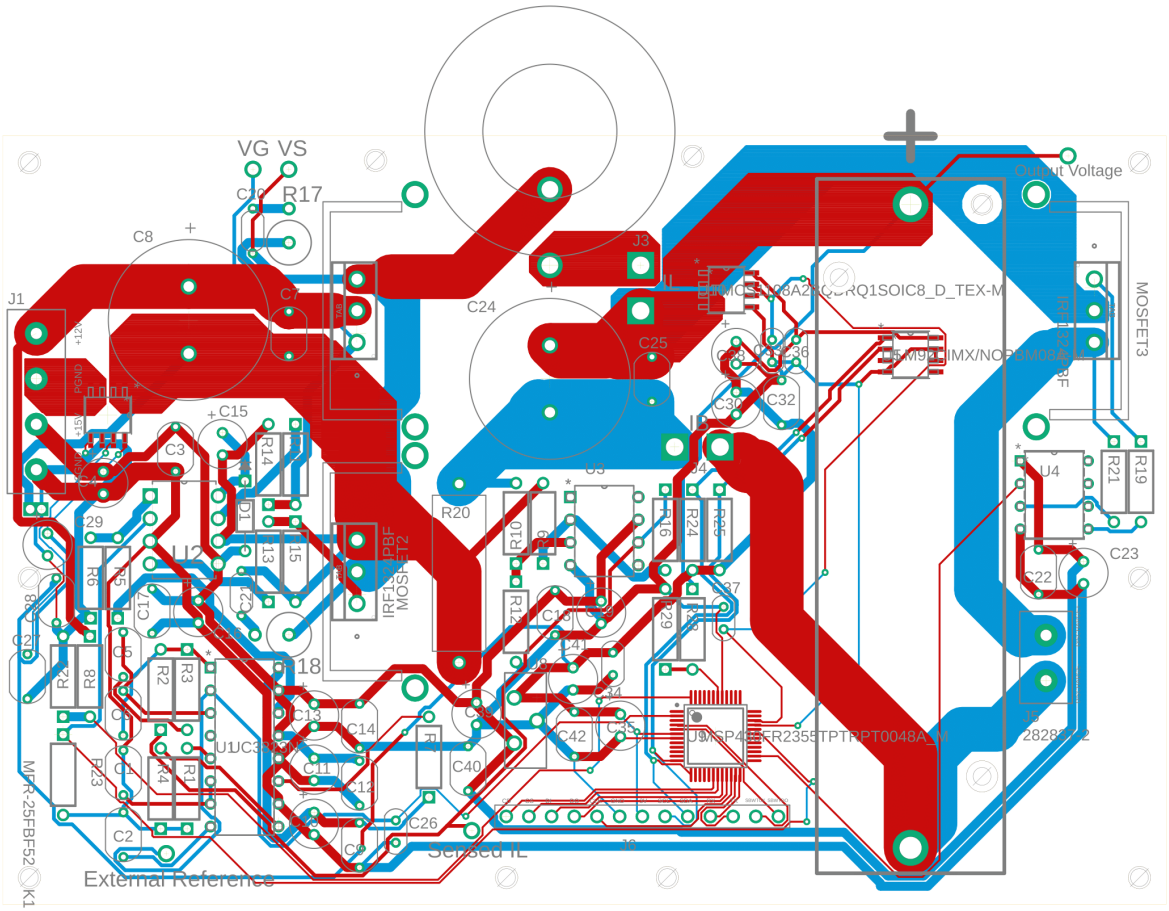

3/24/2023 11:41 AM C:\Users\nhedd\OneDrive\Documents\EAGLE\projects\SYNC_battery_charger\SYNC_battery_charger_3.brd

Figure C3: Board schematic for silicon based cycling system

Table C1: Bill of materials for silicon based cycling system

Designator	Value	Description
B1	3.6V, 2.5Ahr Lithium Ion Cell	battery to be charged
C1	4.7nF	CT capacitor, sets frequency of UC3823
C2	10uF	Softstart ceramic capacitor for UC3823
C3	100nF	filtering capacitor for 15V input
C4	2200uF	decoupling capacitor for 15V input
C5	1.8nF	pole capacitor for EA comp on UC3823
C6	180pF	zero capacitor for EA comp on UC3823
C7	100nf	filtering capacitor for 12V input
C8	2200uF	decoupling capacitor for 12V input
C9	100nF	filtering capacitor for reference voltage on UC3828
C10	10uF	decoupling capacitor for reference voltage on UC3823
C11	10uF	decoupling capacitor for logic input voltage on uc3823
C12	100nF	filtering capacitor for logic input voltage on UC3823
C13	10uF	decoupling capacitor for power input voltage on UC3823
C14	100nF	filtering capacitor for power input voltage on UC3823
C15	1uF	bootstrap capacitor for IR2184
C16	10uF	decoupling capacitor for IR2184
C17	100nF	filtering capacitor for IR2184
C18	100nF	filter capacitor for differential op-amp
C19	10uF	decoupling capacitor for IR2184
C20	22nF	snubber capacitor for upper MOSFET
C21	22nF	snubber capacitor for lower MOSFET
C22	100nF	filter capacitor for discharge gate driver
C23	10uF	decoupling capacitor for discharge gate driver
C24	2200uF	decoupling capacitor for output of buck converter
C25	100nF	filtering capacitor for output of buck converter
C26	1nF	output capacitor for reference from MCU
C30	10uF	decoupling capacitor for LM92
C32	100nF	filtering capacitor for LM92
C33	1nF	output capacitor for hall effect sensor
C34	100nF	filtering capacitor for MCU
C35	10uF	decoupling capacitor for MCU
C36	100nF	filtering capacitor for Hall effect sensor
C37	1nF	output capacitor for hall effect sensor
C38	10uF	decoupling capacitor for Hall effect sensor
C39	10uF	decoupling capacitor for input 15V to 3.3V regulator
C40	100nF	filtering capacitor for input 15V to 3.3V regulator
C41	10uF	decoupling capacitor for output 15V to 3.3V regulator

C42	100nF	filtering capacitor for output 15V to 3.3V regulator
D1	na	bootstrap diode for IR2184
J1	na	4 port input screw terminal for 15V and 12V
J2	na	connection point for signal and power ground
J3	na	inductor current measurement point
J4	na	battery current measurement point
J5	na	battery discharge point
J6	na	programming and info output pins for MCU
J7	na	manual reference for UC2338 point
J8	na	gate measurement point for upper MOSFET
J9	na	source measurement point for upper MOSFET
J10	na	output PWM measurement point from UC3823
J11	na	output voltage measurement point
J12	na	output current sense op-amp measurement point
L1	15uH	inductor for buck converter
MOSFET1	na	upper MOSFET
MOSFET2	na	lower MOSFET
MOSFET3	na	discharge MOSFET
R1	3.3kOhm	RT resistor for UC3823 for setting PWM frequency
R2	1kOhm	input resistor for UC3823 EA comp
R3	1kOhm	feedback resistor for UC3823 EA comp
R4	1kOhm	UC3823 SD pull down resistor
R5	2kOhm	upper leg of PWM output resistor divider
R6	1kOhm	lower leg of PWM output resistor divider
R7	1kOhm	upper leg of ILIM resistor divider
R9	10kOhm	input resistor for differential opamp minus
R10	10kOhm	input resistor for differential opamp plus
R11	20Ohm	input gating resistor for upper MOSFET
R12	150kOhm	plus to ground resistor for differential opamp amp
R13	20Ohm	gating resistor for lower MOSFET
R14	1kOhm	gate-source resistor for upper MOSET
R15	1kOhm	gate-source resistor for lower MOSFET
R16	150kOhm	feedback resistor for differential op-amp
R17	20Ohm	snubber resistor for upper MOSFET
R18	20Ohm	snubber resistor for lower MOSFET
R19	20Ohm	gating resistor for discharging MOSFET
R20	20mOhm	sensing resistor
R21	0ohm	incorrectly placed resistor, should be shorted
R24	10kohm	SDA pull up resistor
R25	10kOhm	SCL pull up resistor

R28	1kOhm	output voltage measurement upper resistor for resistor divider
R29	1kOhm	output voltage measurement lower resistor for resistor divider
U1	na	UC3823N: PWM Controller
U2	na	IR2184: Hi-Lo gate driver
U3	na	TLC081IP: differential op amp
U4	na	MIC5014YN: discharge gate driver
U5	na	LM92CIMX/NOPB: temperature sensor
U7	na	ACS717MATR: hall effect sensor
U8	na	TLV2217-33KCSE3: 15V to 3.3V Regulator
U9	na	MSP430FR2355TPTR: MCU

APPENDIX D

SCHEMATICS AND BILL OF MATERIALS FOR GALLIUM NITRIDE TRANSISTOR CYCYLING SYSTEM

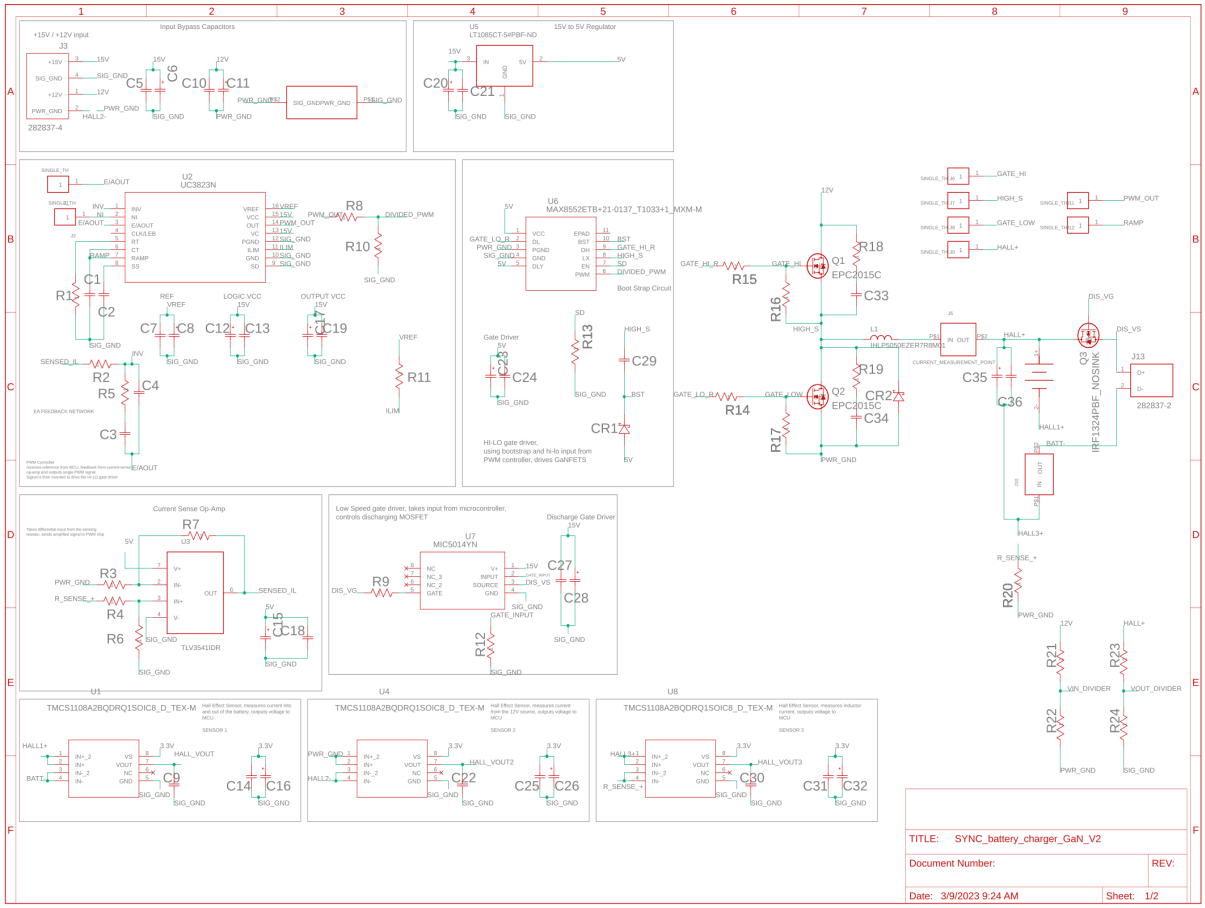

3/24/2023 12:28 PM C:\Users\nhedd\OneDrive\Documents\EAGLE\projects\GaN_Sync_Charger\SYNC_battery_charger_GaN_V2.sch (Sheet: 1/2)

Figure D1: Schematic page 1 for GaN based cycling system

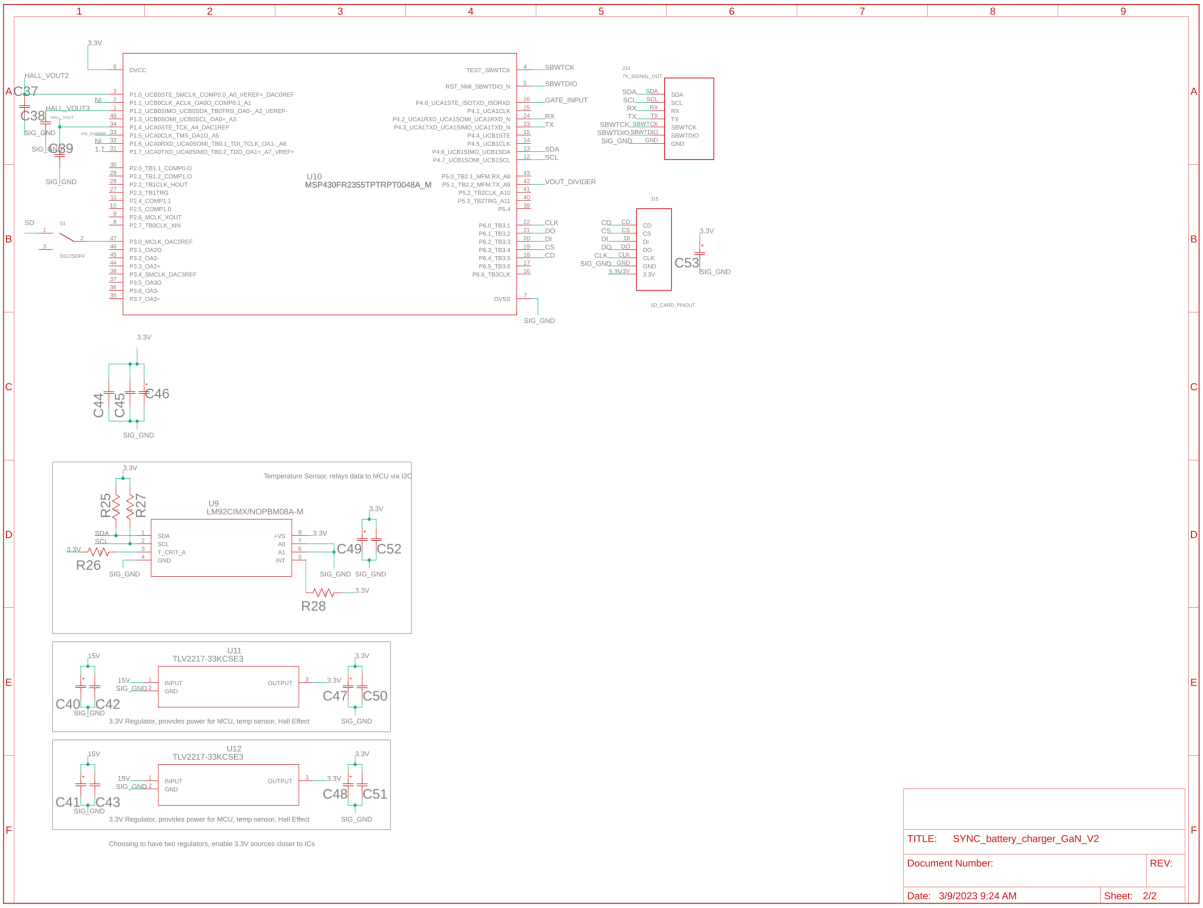

3/24/2023 12:29 PM C:\Users\nhedd\OneDrive\Documents\EAGLE\projects\GaN_Sync_Charger\SYNC_battery_charger_GaN_V2.sch (Sheet: 2/2)

Figure D2: Schematic page 2 for GaN based cycling system

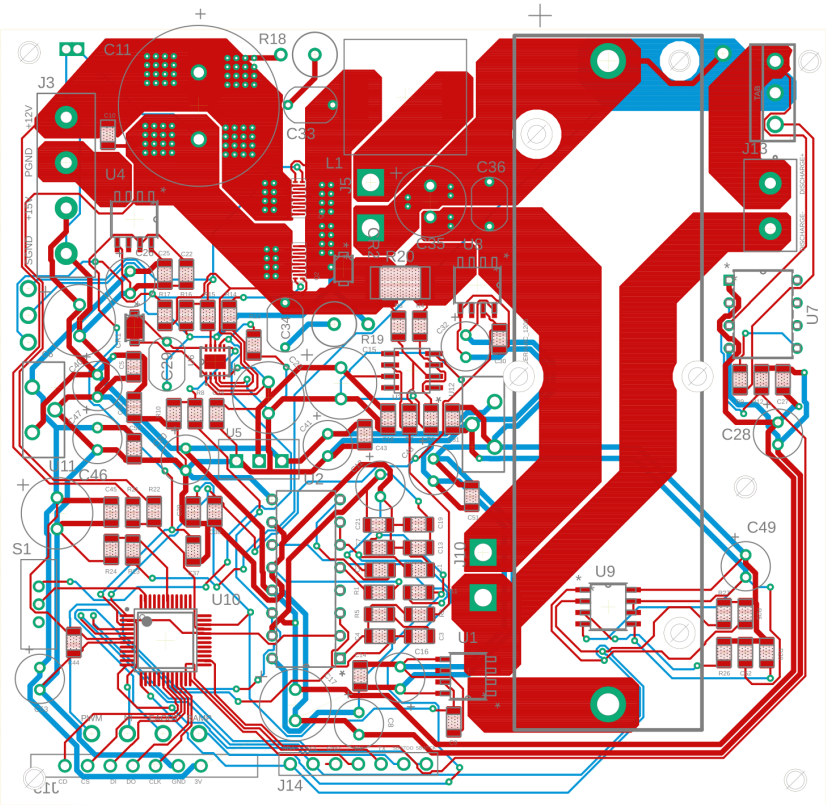

3/24/2023 12:29 PM C:\Users\nhedd\OneDrive\Documents\EAGLE\projects\GaN_Sync_Charger\SYNC_battery_charger_GaN_V2.brd

Figure D3: Board schematic for silicon based cycling system

Table D1: Bill of materials for silicon based cycling system

Designator	Value	Description
B1	18650_BATTERY	Battery to be charged
C1	See description	CT Capacitor, along with RT sets the PWM Frequency for UC3823 100kHz: 4.7nF 500kHz: 1nF 750kHz: 470pF 1MHz: 470pF
C2	10uF	Softstart capacitor for UC3823
C3	See description	CFz capacitor: 100kHz: 1.6nF 500kHz: 318pF 750kHz: 424pF 1MHz: 318pF
C4	See description	CFp capacitor: 100kHz: 160pF 500kHz: 31.8pF 750kHz: 42.4pF 1MHz: 31.8pF
C5	100nF	ceramic bypass capacitor for 15V input
C6	220uF	bullk decoupling capacitor for 15V input
C7	100nF	ceramic bypass capacitor for reference on UC3823
C8	10uF	bulk decoupling capacitor for reference on UC3823
C9	500pF	hall output capacitor on hall sensor 1
C10	100nF	ceramic bypass capacitor for 12V input
C11	2200uF	bulk decoupling capacitor for 12V input
C12	10uF	bulk decoupling capacitor for logic VCC on UC3823
C13	100nF	ceramic capacitor for logic VCC on UC3823
C14	100nF	ceramic capacitor for hall sensor 1
C15	220uF	decoupling capacitor for current sense op-amp
C16	10uF	decoupling capacitor for hall sensor 1
C17	220uF	decoupling capacitor for output VCC on UC3823
C18	100nF	bypass capacitor for current sense op-amp
C19	100nF	ceramic capacitor for output VCC on UC3823
C20	10uF	input decoupling capacitor for 15V to 5V
C21	100nF	input bypass capacitor for 15V to 5V
C22	500pF	output capacitor for hall sensor 2
C23	220uF	decoupling capacitor for gate driver
C24	100nF	bypass capacitir for gate driver
C25	100nF	bypass capacitor for hall effect sensor 2

C26	10uF	decoupling capacitor for hall sensor 2
C27	100nF	bypass capacitor for dicharging gate driver
C28	10uF	decoupling capacitor for discharging gate driver
C29	1uF	bootstrap capacitor for gate driver
C30	500pF	output capacitor for hall sensor 3
C31	100nF	bypass capacitor for hall sensor 3
C32	10uF	decoupling capacitor for hall sensor 3
C33	1nF	snubber capacitor for upper swtich
C34	1nF	snubber capacitor for lower swtich
C35	220uF	decoupling buck output capacitor
C36	100nF	bypass buck output capacitor
C37	500pF	output ceramic capacitor for hall 2
C38	500pF	output ceramic capacitor for hall 3
C39	500pF	output ceramic capacitor for hall 1
C40	10uF	decoupling capacitor for 15V to 3.3V input 1
C41	10uF	decoupling capacitor for 15V to 3.3V input 2
C42	100nF	bypass capacitor for 15V to 3.3V input 1
C43	100nF	bypass capacitor for 15V to 3.3V input 2
C44	100nF	bypass capacitor for MCU
C45	100nF	bypass capacitor for MCU
C46	220uF	decoupling capacitor for MCU
C47	10uF	output decoupling capacitor for 15V to 3.3V 1
C48	10uF	output decopuling capacitor for 15V to 3.3V 2
C49	10uF	decoupling capacitor for temp sensor
C50	100nF	bypass capacitor for output of 15V to 3.3V 1
C51	100nF	bypass capacitof for output of 15V to 3.3V 2
C52	100nF	bypass capacitor for temp sensor
C53	10uF	decoupling capacitor for SD card
CR1	100V, 2A	bootstrap diode
CR2	100V, 2A	lower switch diode
J1	NA	EA measurement
J2	NA	NI measurement
J3	NA	15V and 12V input
J4	NA	gnd connection point
J5	NA	inductor current measurement
J6	NA	high switch gate measurement
J7	NA	high side measurement
J8	NA	low switch gate measurement
J9	NA	output voltage measurement
J10	NA	battery current measurement
J11	NA	pwm output measurement

J12	NA	ramp measurement
J13	NA	discharge resistor output
J14	NA	programming pins
J15	NA	SD Card pin out
L1	15uH	buck inductor
Q1	40V, 53A	upper GaN switch
Q2	40V, 53A	lower GaN switch
Q3	NA	dicharge MOSFET
R1	See description	RT capacitor for setting PWM frequency 100kHz: 3.3kOhm 500kHz: 5kOhm 750kHz: 5kOhm 1MHz: 3kOhm
R2	10kOhm	input EA resistor for UC3823
R3	10kOhm	in- resistor for current sensing op-amp
R4	10kOhm	in+ resistor for current sensing op-amp
R5	See description	10kOhm for 100kHz and 250kHz 5kOhm for 750kHz and 1MHz
R6	150kOhm	in+ to gnd resistor for current sensing op-amp
R7	150kOhm	feedback resistor for current sensing op-amp
R8	2kOhm	upper pwm output resistor divider
R9	10Ohm	gate resistor for discharging mosfet
R10	1kOhm	lower pwm output resistor divider
R11	1kOhm	Ilim pull up
R12	1kOhm	pull down resistor for input of discharging gate driver
R13	1kOhm	pull down resistor for SD on gate driver
R14	10Ohm	low switch input resistor
R15	10Ohm	high switch input resistor
R16	1kOhm	upper gs resistor
R17	1kOhm	lower gs resistor
R18	5Ohm	upper swtich snubber
R19	5Ohm	lower switch snubber
R20	20mOhm	current sense resistor
R21	4kOhm	upper leg of input resistor divider
R22	1kOhm	lower leg of input resistor divider
R23	1kOhm	upper leg of output resistor divider
R24	1kOhm	lower leg of output resistor divider
R25	10kOhm	SDA pull up resistor
R26	10kOhm	T_CRIT pull up
R27	10kOhm	SCL pull up resistor

R28	10kOhm	INT pull up
S1	NA	switch for SD on gate driver
U1	NA	TMCS1107A3BQDR: hall sensor 1
U2	NA	UC3823N: PWM controller
U3	NA	TLV3541IDR: Current sense op-amp
U4	NA	TMCS1108A4BQDR: hall sensor 2
U5	NA	LT1085CT-5#PBF-ND: 15V to 5V regulator
U6	NA	MAX8552ETB+: Gate Driver
U7	NA	MIC5014YN: Discharge Gate Driver
U8	NA	TMCS1107A3BQDR: Hall Sensor 3
U9	NA	LM92CIMX/NOPBM08A-M: temperature sensor
U10	NA	MSP430FR2355TPTR: MCU
U11	NA	TLV2217-33KCSE3: 15V to 3.3V regulator 1

APPENDIX E

PROOF OF SUBMISSION TO JOURNAL OF ENERGY STORAGE FOR REFERENCE 37

Journal of Energy Storage

Fast Charging of Commercial Lithium-ion Battery Without Lithium Plating

--Manuscript Draft--

Manuscript Number:	EST-D-23-01343
Article Type:	Research Paper
Keywords:	Lithium-ion battery (LIB); electrochemical impedance spectroscopy (EIS); Fast Charging; Lithium Plating; Three-electrode lithium-ion cell
Corresponding Author:	Hongwei Gao Bozeman, Montana UNITED STATES
First Author:	Arun Thapa
Order of Authors:	Arun Thapa
	Noah Hedding
	Hongwei Gao
Abstract:	Rapid charging of lithium-ion batteries (LIBs) enables the devices or systems powered by the batteries to provide services at faster rates or higher frequencies. However, fast charging of LIBs can cause lithium plating, resulting in rapid capacity degradation and even thermal runaway or fire in the batteries. Fast charging and lithium plating in a LIB are anode-centric events. Therefore, an anode-centric electrochemical model is critical for deriving a fast charging protocol for LIBs. In this work, we developed an electric circuit model for the negative electrode using tests conducted on laboratory three-electrode lithium-ion cells, used the model to estimate the fast charging current, and compared the fast charging current derived using the model to the fast charging current obtained from measurement. The fast charging current obtained using the model agrees well with the measured fast charging current. Furthermore, we implemented this fast charging protocol on commercial 18650 LIBs for 350 cycles using custom-built charging hardware and software and achieved an 80% state of charge in 29 minutes with acceptable temperature rise. The cell aging analysis revealed no significant capacity degradation nor lithium plating on the anode surface, as the protocol explicitly imposes control to protect the battery from lithium plating.
Suggested Reviewers:	Johannes Sieg johannes.sieg@daimler.com
	David Anseán anseandavid@uniovi.es